Monte Carlo study of Schwinger model at finite temperature and theta

Hiroki Ohata

Yukawa Institute for Theoretical Physics, Kyoto University

February 5, 2024

Abstract

The θ term, the redundant term in gauge theories, has been attracting a large amount of interest due to its intriguing features. The effects of the θ term are purely quantum since the term does not affect the classical equation of motion. Additionally, the θ term explicitly breaks the CP symmetry except for the special case $\theta = \pi$, where the CP symmetry is not explicitly broken due to the topological nature of the term. Despite the theoretical interest, investigating the effects of the θ term by the Monte Carlo method is known to be very challenging due to the sign problem.

The purpose of this thesis is to investigate the interplay between the quantum effects of the θ term and thermal effects through the first-principle Monte Carlo study of quantum electrodynamics in $1 + 1$ dimensions, known as the Schwinger model. The Schwinger model describes confinement, the chiral anomaly, and the nontrivial topological θ vacuum, similar to quantum chromodynamics in $3 + 1$ dimensions. After reviewing the lattice formulations of the Schwinger model, we point out that the sign problem at finite θ can be circumvented by using the bosonization technique, in which the Dirac fermion is transformed into boson, effectively evading the fermion doubling problem and preserving the chiral anomaly intact simultaneously. We explicitly confirm its validity and effectiveness through detailed comparisons with analytical and previous numerical results.

Using the proposed method, we perform a precise calculation of the string tension and quantitatively reveal the confining properties in the Schwinger model at finite temperature and θ. We find that the string tension is strongly affected by the θ term and can become negative for noninteger probe charges near $\theta = \pi$ at low temperatures. Furthermore, we observe that the string tension becomes less dependent as temperature increases, indicating the thermal suppression of the quantum effects of the θ term.

We also explore the phase structure of the Schwinger model at $\theta = \pi$ in the temperature and fermion mass plane focusing on the CP-breaking quantum critical point (QCP) at zero temperature, which belongs to the Ising universality class. Specifically, we perform a detailed investigation of the correlation function of the electric field near the QCP and find that it shares the same asymptotic form as the quantum Ising chain. This finding indicates the existence of three regions near the QCP, each characterized by a specific asymptotic form of the correlation length, and demonstrates that the long-range order at zero temperature is broken by infinitesimally small thermal effects.

Citations to published works

A part of Chapter 2 and Chapters 3, 4 are based on a paper by the author [1]:

- H. Ohata,
  "Monte Carlo study of Schwinger model without the sign problem,"
  Journal of High Energy Physics, 12 (2023) 007,
  arXiv:2303.05481 [hep-lat].

Chapter 5 is based on a paper by the author [2]:

- H. Ohata,
  "Phase diagram near the quantum critical point in Schwinger model at $\theta = \pi$:
  analogy with quantum Ising chain,"
  Progress of Theoretical and Experimental Physics, 013B02 (2023),
  arXiv:2311.04738 [hep-lat].

Contents

Chapter 1

Introduction

1.1 Background and purpose

Gauge theories form the basis of our understanding of subatomic physics. All fundamental interactions except gravity, the strong, weak, and electromagnetic interactions, are described by gauge theories. Historically, the gauge principle has played a crucial role in the development of fundamental theories, imposing significant constraints on the form of the Lagrangian.

The strong interaction is described by quantum chromodynamics (QCD), whose gauge group is SU(3). Under the guiding principle of SU(3) gauge symmetry and renormalizability, the QCD action is *almost uniquely* determined to take the simple form of

$$S_{\text{QCD}} = \int d^4x \, \frac{1}{2} \text{tr}(G_{\mu\nu} G_{\mu\nu}) + \sum_f \bar{q}_f (\gamma_\mu D_\mu + m_f) q_f, \tag{1.1}$$

where q_f represents quark of mass m_f, $G_{\mu\nu}$ is the field strength of gluon A_μ, and the interaction among them is encoded in the covariant derivative $D_\mu = \partial_\mu + ig A_\mu$.

The gauge symmetry has a significant impact on the properties of the theory. In QCD, due to the non-Abelian nature of SU(3) gauge group, which appears characteristically in the field strength

$$G_{\mu\nu} := \frac{1}{ig} [D_\mu, D_\nu] = \partial_\mu A_\nu - \partial_\nu A_\mu + ig[A_\mu, A_\nu], \tag{1.2}$$

gluon has self-interactions. This feature, which is absent in Abelian gauge theories, leads to the remarkable energy scale Q dependence of the renormalized gauge coupling [3, 4]

$$\alpha_s(Q) := \frac{g^2}{4\pi} \simeq \frac{12\pi}{33 - 2N_f} \frac{1}{\ln\left(Q^2/\Lambda_{\text{QCD}}^2\right)}, \tag{1.3}$$

where $\Lambda_{\text{QCD}} \simeq 200\,\text{MeV}$ is the empirically determined scale parameter, and N_f is the number of massless quark flavors. In our real world, there exist two light flavors, called up and down quarks. Therefore, the gauge coupling of QCD becomes small as the energy scale increases, allowing for the perturbative analysis. This property is called asymptotic freedom. In contrast to asymptotic freedom, the QCD gauge coupling becomes large as the energy scale

decreases. This property makes the analytical investigation of low-energy QCD extremely difficult. Nevertheless, it also gives rise to important nonperturbative phenomena, such as confinement of quark and spontaneous breaking of the chiral symmetry. Figure 1.1 shows a summary of measurements of $\alpha_s(Q)$ at various energy scales, compared to the theoretical curve incorporating the higher-order loop effects [5]. We find that the theoretical curve
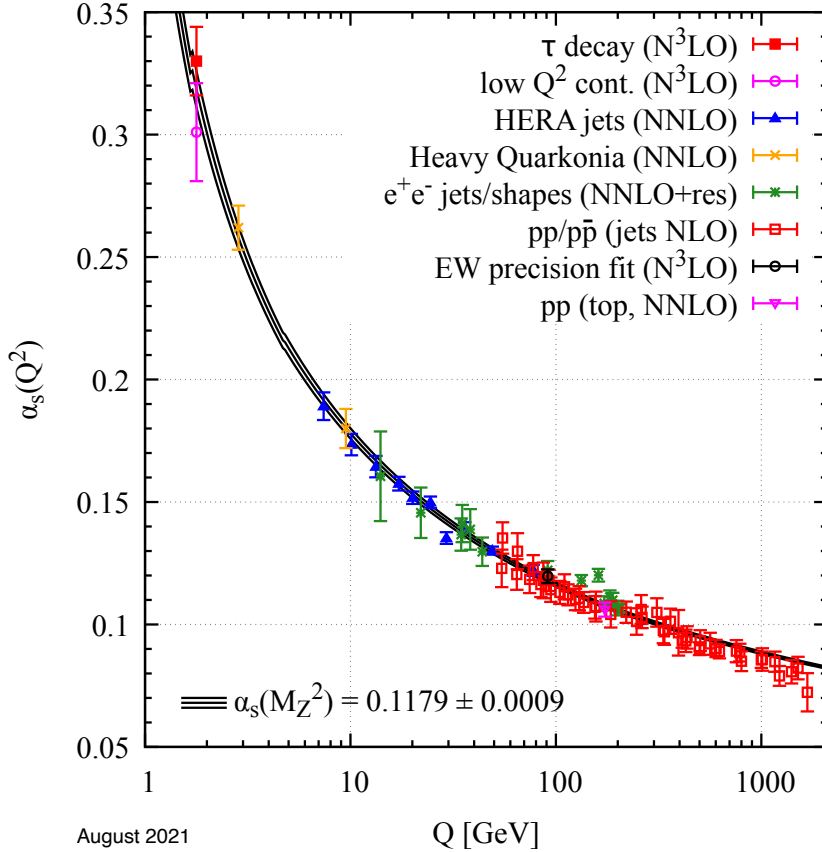
Figure 1.1: Summary of measurements of $\alpha_s(Q)$ at various energy scales Q. This figure is taken from Review of Particle Physics, 2022 [5].

successfully explains diverse experimental results over a wide range of energy scales. This provides strong evidence that QCD is the fundamental theory of the strong interaction.

Behind the success of QCD, there remains one theoretical open problem related to the formulation of QCD, the strong CP problem. In fact, the gauge principle and renormalizability *do not* uniquely determine the QCD Lagrangian. It is possible to add the so-called θ term into the action

$$i\theta Q, \quad Q = \int d^4x \, \frac{g^2}{32\pi^2} \epsilon_{\mu\nu\rho\sigma} \operatorname{tr}(G_{\mu\nu}G_{\rho\sigma}), \tag{1.4}$$

where $\epsilon_{\mu\nu\rho\sigma}$ is the antisymmetric tensor. Unlike the action of QCD (1.1), the θ term is antisymmetric under the CP transformation. Therefore, the real parameter θ determines the

degree of the explicit CP symmetry breaking in the strong interaction. In our real world, the most recent measurement on the neutron electric dipole moment yields [6]

$$d_n = (0.0 \pm 1.1_{\text{stat}} \pm 0.2_{\text{sys}}) \times 10^{-26} \, e.\text{cm}, \tag{1.5}$$

indicating that the absolute value of θ must be extremely small

$$|\theta| \lesssim 3 \times 10^{-12}. \tag{1.6}$$

While the most popular solution to the strong CP problem is the Peccei–Quinn mechanism, which predicts a new particle called axion, the existence of axion is not experimentally confirmed at present (see, e.g., Ref. [7] for a review).

Aside from the strong CP problem, the θ term has intriguing features due to its topological nature. It is known that the topological charge Q (1.4) takes an integer for any gluonic configuration that gives a finite contribution to the Euclidean path-integral. Therefore, θ has 2π periodicity, and the most distinct point from our vacuum is $\theta = \pi$. Interestingly, the most distinct point $\theta = \pi$ is, in a sense, similar to our vacuum $\theta = 0$ as the CP symmetry is not explicitly broken despite the presence of the θ term, as evident from the equivalence between $\theta = \pi$ and $\theta = -\pi$. Additionally, the effects of the θ term are purely quantum since the term is a total derivative term and does not affect the classical equation of motion. Hence, by examining the quantum effects of the θ term, we can gain insights into the quantum nature of the system and also deepen the understanding of our vacuum $\theta = 0$.

Despite the theoretical interest, investigating the quantum effects of the θ term is difficult. While the Monte Carlo simulation is currently the only first-principle method to investigate the low-energy properties of QCD, the conventional Monte Carlo method can not be applied as the θ term appears purely imaginary in the Euclidean path-integral. This problem is called the sign problem. Despite the proposal and testing of various approaches to overcome the sign problem, the simulation of QCD in $3+1$ dimensions is not yet satisfactory, in particular, near $\theta = \pi$.

In this thesis, we investigate the quantum effects of the θ term not in QCD but in quantum electrodynamics in $1+1$ dimensions, commonly referred to as the Schwinger model [8]. The Schwinger model describes the nontrivial topological θ vacuum, the chiral anomaly, and confinement, similar to QCD. Therefore, the Schwinger model can be regarded as a toy model of QCD. Due to the low dimensionality, the Schwinger model can be investigated to some extent analytically using the bosonization technique [9, 10, 11, 12, 13, 14, 15, 16, 17, 18] and is even exactly solvable when the fermion is massless [8, 14, 15, 16, 19]. Recently, many approaches have been applied to the Schwinger model, including the tensor network method [20, 21, 22, 23, 24, 25, 26, 27, 28, 29, 30, 31, 32, 33], the quantum computing [34, 35, 36, 37, 38, 39, 40, 41, 42, 43], the dual formulation [44, 45], and the Lefschetz thimble method [46, 47].

We particularly focus on the interplay between the quantum effects of the θ term and thermal effects. In general, quantum effects are more pronounced in low-dimensional systems. On the other hand, thermal effects tend to spoil the quantum nature of the system. Therefore, investigating how the quantum effects of the θ term are disputed by thermal effects is an

interesting research topic. For this purpose, we propose a novel method to simulate the Schwinger model at finite temperature and θ without suffering the sign problem, the Monte Carlo study of the lattice bosonized Schwinger model. After explicitly confirming the validity and effectiveness of the proposed method, we apply the method to the study of the confining properties of the Schwinger model at finite temperature and θ [1] and also the phase structure of the model at $\theta = \pi$ in the temperature and fermion mass plane [2].

1.2 Schwinger model and the θ term

In this section, we review the basic properties of the Schwinger model and the θ term in the Euclidean space-time.

1.2.1 Schwinger model

The Schwinger model is quantum electrodynamics in $1 + 1$ dimensions [8]. The Euclidean action of the Schwinger model is given by

$$S_E = \int d^2x \, \frac{1}{4} F_{\mu\nu} F_{\mu\nu} + \overline{\psi}(\gamma_\mu D_\mu + m)\psi, \tag{1.7}$$

where A_μ is the U(1) gauge field, ψ the Dirac fermion, m the fermion mass, and $g > 0$ the dimensionful gauge coupling. The covariant derivative and the field strength are defined as

$$D_\mu = \partial_\mu + igA_\mu, \tag{1.8}$$

$$F_{\mu\nu} = \frac{1}{ig}[D_\mu, D_\nu] = \partial_\mu A_\nu - \partial_\nu A_\mu, \tag{1.9}$$

respectively. $\gamma_\mu, \mu = 0, 1$ are the gamma matrices, which satisfy the anticommutation relation

$$\{\gamma_\mu, \gamma_\nu\} = 2\delta_{\mu\nu}, \tag{1.10}$$

where $\delta_{\mu\nu}$ in Kronecker's delta, and $\overline{\psi} = \psi^\dagger \gamma_0$ is the Dirac conjugate.

1.2.2 Symmetry in the Schwinger model

The Euclidean action (1.7) is symmetric under the U(1) gauge transformation $e^{i\alpha(x)} \in$ U(1),

$$A_\mu(x) \rightarrow A_\mu(x) - \frac{1}{g}\partial_\mu \alpha(x), \tag{1.11}$$

$$\psi(x) \rightarrow e^{i\alpha(x)}\psi(x), \tag{1.12}$$

$$\overline{\psi}(x) \rightarrow \overline{\psi}(x)e^{-i\alpha(x)}. \tag{1.13}$$

Indeed, under the U(1) gauge transformation, the covariant derivative and the field strength transform as

$$D_\mu \rightarrow e^{i\alpha(x)} D_\mu e^{-i\alpha(x)}, \tag{1.14}$$

$$F_{\mu\nu} \rightarrow F_{\mu\nu}, \tag{1.15}$$

respectively. Therefore, the Euclidean action (1.7) is symmetric under the U(1) gauge transformation.

We next introduce the vector and chiral symmetries. The vector transformation is defined by

$$\psi \to e^{i\alpha}\psi, \tag{1.16}$$

$$\overline{\psi} \to \overline{\psi}e^{-i\alpha}, \tag{1.17}$$

where α is a constant real number in the Euclidean space-time. Similarly, the chiral transformation is defined by

$$\psi \to e^{i\alpha\gamma_5}\psi, \tag{1.18}$$

$$\overline{\psi} \to \overline{\psi}e^{i\alpha\gamma_5}, \tag{1.19}$$

where γ_5 is defined as

$$\gamma_5 = \gamma_0\gamma_1. \tag{1.20}$$

The Euclidean action (1.7) is invariant under the vector transformation. In contrast, the Euclidean action (1.7) is invariant under the chiral transformation only at $m = 0$. Interestingly, the chiral symmetry is explicitly broken even at $m = 0$ due to the chiral anomaly [48, 49, 50]. The conservation law of the chiral current

$$j_\mu^5 = \overline{\psi}\gamma_5\gamma_\mu\psi \tag{1.21}$$

is known to be violated as

$$\partial_\mu j_\mu^5 = \frac{g}{\pi}E, \tag{1.22}$$

where E is the electric field. The relation (1.22) can be derived from the diagrammatic analysis or the chiral transformation properties of the path-integral measure [51, 52]. The existence of the chiral anomaly is closely related to the fermion doubling problem, a significant obstacle in formulating the fermion field on a lattice.

Let us discuss the effect of the chiral anomaly on the vacuum expectation value of the chiral condensate $\overline{\psi}\psi$. Because the chiral condensate is not invariant under the chiral transformation, and spontaneous breaking of continuous symmetry is prohibited in $(1 + 1)$-dimensional relativistic quantum field theories [53], the vacuum expectation value of the chiral condensate must be zero if not for the chiral anomaly. In fact, the chiral condensate has a nonzero expectation value of [8]

$$\langle\overline{\psi}\psi\rangle = -\frac{e^\gamma}{2\pi^{3/2}}g, \tag{1.23}$$

where $\gamma = 0.57721...$ is Euler's constant. Thus, the breaking of the chiral symmetry in the Schwinger model is driven by the chiral anomaly.

In addition to the continuous local and global symmetries, the Euclidean action of the Schwinger model (1.7) also has discrete global symmetries, such as charge conjugation (C), parity (P), and time reversal (T) symmetries. Unlike continuous symmetries, spontaneous symmetry breaking of such symmetry is not prohibited. We discuss the spontaneous breaking of the CP symmetry in Chapter 5.

1.2.3 θ term

While the gauge principle imposes significant constraints on the Lagrangian, it is possible to introduce the θ term in $(1+1)$-dimensional U(1) gauge theory

$$i\theta Q, \quad Q = \int d^2 x \, \frac{g}{4\pi} \epsilon_{\mu\nu} F_{\mu\nu}, \tag{1.24}$$

where $\epsilon_{\mu\nu}$ is the antisymmetric tensor. The θ term is antisymmetric under the CP transformation, unlike the Euclidean action of the Schwinger model (1.7). Thus, introducing the θ term into the action typically results in the explicit breaking of the CP symmetry.

Intriguing features of the θ term arise from the fact that the topological charge Q takes an integer for any gauge configuration that is finite in $\mathbb{R}^2$. By converting the volume integral to a circular integral of radius R, which is sent to infinity, using Gauss's divergence theorem, the topological charge Q is expressed as

$$Q = \frac{g}{2\pi} \int_{\mathbb{R}^2} d^2 x \, \partial_0 A_1 + \partial_1(-A_0) \tag{1.25a}$$

$$= \lim_{R \to \infty} \frac{g}{2\pi} R^2 \int_0^{2\pi} d\varphi \, (A_1 \cos\varphi - A_0 \sin\varphi). \tag{1.25b}$$

Because only gauge configurations that are finite in $\mathbb{R}^2$

$$\int d^2 x \, \frac{1}{4} F_{\mu\nu} F_{\mu\nu} = \int d^2 x \, \frac{1}{2} E^2 < \infty \tag{1.26}$$

contribute to the Euclidean path-integral, the electric field E must approach zero in the infinite radius limit $R \to \infty$. Equivalently, the gauge field must take the pure gauge form

$$A_\mu = -\frac{1}{g} \partial_\mu \alpha(\varphi). \tag{1.27}$$

By substituting the form into Eq. (1.25b), we find

$$Q = -\frac{1}{2\pi} \int_0^{2\pi} d\varphi \, \partial_\varphi \alpha(\varphi). \tag{1.28}$$

Because of the 2π periodicity of the gauge function $\alpha(\varphi)$, we can conclude that Q takes an integer. The following intriguing properties are now easily understood:

- The effects of the θ term are purely quantum since the term does not affect the classical equation of motion.

- The θ angle has 2π periodicity.

- The θ term explicitly breaks the CP symmetry except for the special case $\theta = \pi$, where the CP symmetry is not explicitly broken.

In the Euclidean formulation, the expectation value of an observable can be decomposed as

$$\langle O \rangle = \int D\overline{\psi} D\psi DA\, O \exp(-S_E - i\theta Q) \Big/ Z \tag{1.29a}$$

$$= \sum_{Q=0,\pm1,\pm2,\dots} \exp(-i\theta Q) \int D\overline{\psi} D\psi DA^{(Q)}\, O \exp(-S_E) \Big/ Z, \tag{1.29b}$$

where $DA^{(Q)}$ denotes the path-integral over all gauge configurations of topological charge Q, and Z is the partition function. Thus, the θ angle governs the relative weight between different topological charge vacua.

1.3 Hamiltonian formalism

In this section, we discuss the Hamiltonian formalism of the Schwinger model to gain a different perspective from the Euclidean formulation. We start with the Minkowski action of the Schwinger model with the θ term

$$S_M = \int d^2x\, \mathcal{L}, \tag{1.30}$$

$$\mathcal{L} = -\frac{1}{4} F_{\mu\nu} F^{\mu\nu} + \theta \frac{g}{4\pi} \epsilon_{\mu\nu} F^{\mu\nu} + \overline{\psi}(i\gamma^\mu D_\mu - m)\psi, \tag{1.31}$$

where $\gamma^\mu, \mu = 0, 1$ are the gamma matrices in the Minkowski space-time, which satisfy the anticommutation relation

$$\{\gamma^\mu, \gamma^\nu\} = 2g^{\mu\nu}, \tag{1.32}$$

and the Dirac conjugate is defined by $\overline{\psi} = \psi^\dagger \gamma^0$. We use the following notation in the Minkowski space-time throughout this thesis:

$$x^0 = t, \quad x^1 = x, \quad g^{\mu\nu} = \mathrm{diag}(1, -1), \quad \epsilon^{01} = 1. \tag{1.33}$$

The conjugate momenta are defined as

$$\pi_\psi := \partial\mathcal{L}/\partial\dot{\psi} = i\psi^\dagger, \tag{1.34}$$

$$\pi_{\psi^\dagger} := \left(\partial/\partial\dot{\psi}^\dagger\right)\mathcal{L} = 0, \tag{1.35}$$

$$\pi_0 := \frac{\partial\mathcal{L}}{\partial\dot{A}^0} = 0, \tag{1.36}$$

$$E := \frac{\partial\mathcal{L}}{\partial\dot{A}^1} = \dot{A}^1 + \partial_x A^0 - \frac{\theta g}{2\pi}, \tag{1.37}$$

respectively. While $\pi_{\psi^\dagger}$ and π_0 do not appear in the Hamiltonian since they are equal to zeros, equations (1.35, 1.36) form constraints on the physical Hilbert space. From the nonzero parts

of the conjugate momenta, the Hamiltonian is obtained as

$$H = \int dx\, E\dot{A}^1 + \pi_\psi \dot{\psi} - \mathcal{L} \tag{1.38}$$

$$= \int dx\, \frac{1}{2}\left(E + \frac{g\theta}{2\pi}\right)^2 - E\partial_x A^0 + \pi_\psi\left(igA^0 - \gamma^5\partial_x + igA^1\gamma^5 - im\gamma^0\right)\psi. \tag{1.39}$$

Under the Hamiltonian (1.39), the time evolution of $\pi_{\psi^\dagger}, A^0, \pi_0$ are calculated as

$$\dot{\pi}_{\psi^\dagger} = -\left(\delta/\delta\psi^\dagger\right)H = 0, \tag{1.40}$$

$$\dot{A}^0 = \frac{\delta H}{\delta\pi_0} = 0, \tag{1.41}$$

$$\dot{\pi}_0 = -\frac{\delta H}{\delta A^0} = -\partial_x E + g\psi^\dagger\psi. \tag{1.42}$$

By taking the temporal gauge $A^0 = 0$ at the initial state, A^0 remains zero at any time, allowing us to simplify the Hamiltonian. For the constraint (1.36) to be satisfied, the Gauss law

$$\partial_x E - g\psi^\dagger\psi = 0 \tag{1.43}$$

must be imposed. Combining these together, we arrive at the simplified Hamiltonian

$$H = \int dx\, \frac{1}{2}\left(E + \frac{g\theta}{2\pi}\right)^2 - \pi_\psi\left(\partial_x - igA^1\right)\gamma^5\psi - im\pi_\psi\gamma^0\psi \tag{1.44a}$$

$$= \int dx\, \frac{1}{2}\left(E + \frac{g\theta}{2\pi}\right)^2 - \overline{\psi}\left(i\partial_x + gA^1\right)\gamma^1\psi + m\overline{\psi}\psi, \tag{1.44b}$$

where the electric field and the fermion density are constrained by the Gauss law (1.43).

The quantization is performed by imposing the equal-time (anti)commutation relations

$$\left\{\psi_\alpha(x,t), \psi_\beta^\dagger(y,t)\right\} = \delta_{\alpha\beta}\delta(x-y), \tag{1.45}$$

$$\{\psi_\alpha(x,t), \psi_\beta(y,t)\} = \left\{\psi_\alpha^\dagger(x,t), \psi_\beta^\dagger(y,t)\right\} = 0, \tag{1.46}$$

$$\left[A^1(x,t), E(y,t)\right] = i\delta(x-y), \tag{1.47}$$

where α, β denote the spinor indices.

1.3.1 Bosonized Hamiltonian

The physics of the Schwinger model becomes much more transparent using the bosonization technique, in which the Dirac field ψ is transformed into the scalar field ϕ and its conjugate momenta π. The concept of bosonization of the Dirac fermion first appeared in Coleman's proof of the equivalence between the Thirring model and the sine-Gordon model [9]. Coleman's proof was based on the explicit confirmation of equivalence in the coefficients of

16

perturbation expansion at any order, and its generalization to other models, such as the Schwinger model, was not clear. Subsequently, Mandelstam explicitly constructed the Dirac fermion from the bosonic fields, establishing that bosonization is a universal concept in $1 + 1$ dimensions [10] (see Appendix A). The bosonized form of the Schwinger model first appeared in Ref. [11]. In this subsection, we use the chiral representation of the gamma matrices

$$\gamma^0 = \sigma^1, \quad \gamma^1 = i\sigma^2, \quad \gamma^5 = \gamma^0\gamma^1 = -\sigma^3. \tag{1.48}$$

For bosonization of the Hamiltonian of the Schwinger model (1.44b), the following bosonization formulae are necessary:

$$j^\mu = \overline{\psi}\gamma^\mu\psi = \begin{cases} \frac{1}{\sqrt{\pi}}\partial_x\phi, & \mu = 0, \\ -\frac{1}{\sqrt{\pi}}\pi, & \mu = 1, \end{cases} \tag{1.49}$$

$$-\overline{\psi}i\partial_x\gamma^1\psi = \frac{1}{2}\pi^2 + \frac{1}{2}(\partial_x\phi)^2, \tag{1.50}$$

$$\overline{\psi}\psi = -\frac{e^\gamma}{2\pi}\mu\mathcal{N}_\mu\cos(2\sqrt{\pi}\phi). \tag{1.51}$$

Here, the symbol $\mathcal{N}_\mu$ denotes the normal ordering with respect to the bosonic creation and annihilation operators defined as

$$\phi(x) =: \int \frac{dk}{2\pi}\left(\frac{1}{2\omega(k,\mu)}\right)^{1/2}\left[a(k,\mu)e^{-ikx} + a^\dagger(k,\mu)e^{ikx}\right], \tag{1.52}$$

$$\pi(x) =: -i\int \frac{dk}{2\pi}\left(\frac{\omega(k,\mu)}{2}\right)^{1/2}\left[a(k,\mu)e^{-ikx} - a^\dagger(k,\mu)e^{ikx}\right], \tag{1.53}$$

where $\omega(k,\mu) = \sqrt{k^2 + \mu^2}$ and μ being the energy scale to define the normal ordering. The derivation of these bosonization formulae requires somewhat complicated manipulations and the detail can be found in Appendix A.

We note that the chiral condensate does not depend on the energy scale μ. This can be seen by removing the normal ordering using Wick's theorem. Coleman showed that the normal ordering can be removed as [9]

$$\mathcal{N}_\mu\exp(i2\sqrt{\pi}\phi) = \exp\{2\pi\Delta(x = 0; \mu)\}\exp(i2\sqrt{\pi}\phi), \tag{1.54}$$

where $\Delta(x;\mu)$ is the Feynman propagator for the scalar field of mass μ. The Feynman propagator is divergent at the origin in the continuum. This divergence can be regularized with an ultraviolet (UV) cutoff Λ by subtracting the divergent part as

$$\Delta(x;\mu;\Lambda) := \Delta(x;\mu) - \Delta(x;\Lambda) = \frac{1}{2\pi}\ln\frac{\Lambda}{\mu} + \mathcal{O}(x^2), \tag{1.55}$$

leading to the formula [9]

$$\mathcal{N}_\mu\exp(i2\sqrt{\pi}\phi) = \frac{\Lambda}{\mu}\exp(i2\sqrt{\pi}\phi). \tag{1.56}$$

The re-normal ordering formula [9], which states the connection between the normal orderings using different energy scales,

$$\mu \mathcal{N}_\mu \exp\big(i2\sqrt{\pi}\phi\big) = \mu' \mathcal{N}_{\mu'} \exp\big(i2\sqrt{\pi}\phi\big) \tag{1.57}$$

is derived from Eq. (1.56). The re-normal ordering formula ensures the independence of the energy scale μ in the bosonized form of the chiral condensate (1.51).

Using the bosonized form of the fermion density (1.49), the Gauss law (1.43) is

$$\partial_x \left(E - \frac{g}{\sqrt{\pi}}\phi \right) = 0, \tag{1.58}$$

and solved as

$$E = \frac{g}{\sqrt{\pi}}\phi. \tag{1.59}$$

The constant of integration is interpreted as the external electric field and absorbed into θ. Conversely, the θ angle is physically interpreted as the external electric field

$$E_{\text{ex}} = \frac{g\theta}{2\pi} \tag{1.60}$$

in the Schwinger model [12]. This perspective is useful for the description of the pair of static probe charges and the semiclassical picture of confinement in Chapter 4. The total electric field is given by

$$E_{\text{tot}} = E + E_{\text{ex}} = \frac{g}{\sqrt{\pi}} \left(\phi + \frac{\theta}{2\sqrt{\pi}} \right). \tag{1.61}$$

Henceforth, we refer to E_{tot} as the electric field and write E_{tot} as E.

Using the bosonization formulae (1.49, 1.50, 1.51), and setting the energy scale to $\mu = g/\sqrt{\pi}$, we arrive at the Hamiltonian of the bosonized Schwinger model [11]

$$H = \int dx \, \frac{1}{2}\pi^2 + \frac{1}{2}(\partial_x\phi)^2 + \frac{g^2}{2\pi} \left(\phi + \frac{\theta}{2\sqrt{\pi}} \right)^2 - \frac{e^\gamma}{2\pi^{3/2}} mg \mathcal{N}_{g/\sqrt{\pi}} \cos\big(2\sqrt{\pi}\phi\big). \tag{1.62}$$

Note that the term proportional to A^1 is expressed as

$$-\overline{\psi} g A^1 \gamma^1 \psi = \frac{g A^1}{\sqrt{\pi}} \pi \tag{1.63}$$

and eliminated by a redefinition of the conjugate momentum π. It is now evident that the Schwinger model is equivalent to the free boson theory of mass $g/\sqrt{\pi}$ at $m = 0$. Therefore, the massless Schwinger model is exactly solvable. At $m \neq 0$, the Hamiltonian includes both the bosonic mass term and the cosine term, making an analytically exact treatment extremely difficult. For small fermion mass, the perturbation in terms of the fermion mass m/g can be used and discussed in Refs. [54, 55, 56]. For large fermion mass, ordinary perturbation in terms of the gauge coupling g/m is possible.

18

1.3.2 Chiral anomaly

Let us finally discuss the chiral anomaly in the bosonized Hamiltonian (1.62). From the bosonized form of the vector current (1.49), the chiral current turns out to be

$$j_5^\mu = \overline{\psi}\gamma^5\gamma^\mu\psi = \begin{cases} \frac{1}{\sqrt{\pi}}\pi, & \mu = 0, \\ -\frac{1}{\sqrt{\pi}}\partial_x\phi, & \mu = 1. \end{cases} \tag{1.64}$$

The chiral charge is given by

$$Q_5 = \int dx\, j_5^0 = \frac{1}{\sqrt{\pi}}\int dx\, \pi, \tag{1.65}$$

and satisfies the commutation relations

$$[\phi(x), Q_5] = \frac{i}{\sqrt{\pi}}, \tag{1.66}$$

$$[\pi(x), Q_5] = 0. \tag{1.67}$$

The chiral transformation acts on the scalar field and its conjugate momenta as [57]

$$\phi \to e^{-i\alpha Q_5}\phi e^{i\alpha Q_5} = \phi - \frac{\alpha}{\sqrt{\pi}}, \tag{1.68}$$

$$\pi \to e^{-i\alpha Q_5}\pi e^{i\alpha Q_5} = \pi, \tag{1.69}$$

respectively. Therefore, the bosonized Hamiltonian is not invariant under the chiral transformation even at $m = 0$, as expected from the chiral anomaly. More specifically, at $m = 0, \theta = 0$, because the time evolution of the scalar field and its conjugate momentum are given by

$$\dot{\phi} = \frac{\delta H}{\delta \pi} = \pi, \tag{1.70}$$

$$\dot{\pi} = -\frac{\delta H}{\delta \phi} = \partial_x^2\phi - \frac{g^2}{\pi}\phi, \tag{1.71}$$

the conservation law of the chiral current is violated

$$\partial_\mu j_5^\mu = \frac{1}{\sqrt{\pi}}\left(\dot{\pi} - \partial_x^2\phi\right) = \frac{g}{\pi}E. \tag{1.72}$$

In contrast, the conservation law of the vector current is preserved

$$\partial_\mu j^\mu = \frac{1}{\sqrt{\pi}}\partial_x\left(\dot{\phi} - \pi\right) = 0. \tag{1.73}$$

19

1.4 Outline of this thesis

In this chapter, we first presented the theoretical background and purpose of this thesis. We next reviewed the basic properties of the Schwinger and the θ term in both the Lagrangian and Hamiltonian formalism, including the bosonized Schwinger model in the Hamiltonian formalism.

The remaining part of this thesis is organized as follows. In Chapter 2, we introduce three different lattice formulations of the Schwinger model. We compare their respective advantages and disadvantages and conclude that the lattice formulation of the bosonized Schwinger model is the most preferable formulation from both theoretical and practical numerical sides for our purpose. In Chapter 3, we perform an explicit verification of the lattice bosonized Schwinger model from analytical and numerical analyses. In Chapter 4, we investigate the confining properties in the Schwinger model at finite temperature and θ. In Chapter 5, we study the phase structure of the Schwinger model at $\theta = \pi$ in the temperature and fermion mass plane. Chapter 6 is devoted to summary and outlook.

Chapter 2

Lattice formulation of the Schwinger model

As seen in the previous chapter, the massive Schwinger model is far from being exactly solvable. First-principle numerical simulations are desired for a quantitative and conclusive understanding of the model. For numerical simulations, it is necessary to formulate the model on a lattice. In this chapter, we introduce three different lattice formulations of the Schwinger model and compare their respective advantages and disadvantages. We stress that the lattice formulation itself is important as a mathematically rigorous formulation of the model. Special attention is given to the manifestation of the chiral anomaly on a lattice.

2.1   Lattice gauge theory

We first review the lattice discretization of the Euclidean action of the Schwinger model (1.7) using lattice gauge theory of Wilson [58]. The most significant feature of lattice gauge theory is that the gauge symmetry is manifestly preserved on a lattice. While the concept of lattice gauge theory was first invented to discuss confinement of quark in QCD [58], the formulation can also be readily applied to the Schwinger model, whose gauge group is U(1).

In lattice gauge theory, the fermion field is defined on a site, and the gauge field is defined on a link, as shown in Fig. 2.1. To preserve the gauge symmetry on a lattice, Wilson proposed to express the gauge field in terms of the link variable [58]

$$U_{\mu,x} \leftrightarrow e^{iagA_\mu(x)}, \tag{2.1}$$

where a is the lattice spacing. Under the U(1) gauge transformation $e^{i\alpha_x} \in \mathrm{U}(1)$, the link variable and the fermion field are transformed as

$$U_{\mu,x} \to e^{i\alpha_x} U_{\mu,x} e^{-i\alpha_{x+\hat{\mu}}}, \tag{2.2}$$

$$\psi_x \to e^{i\alpha_x} \psi_x, \tag{2.3}$$

$$\overline{\psi}_x \to \overline{\psi}_x e^{-i\alpha_x}, \tag{2.4}$$
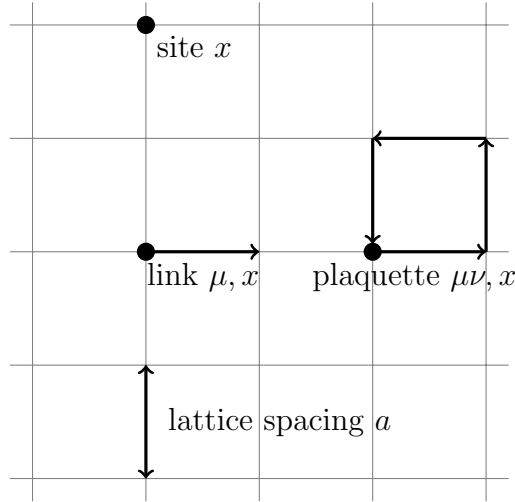
respectively.

Figure 2.1: Terminology of lattice gauge theory.

2.1.1 Plaquette gauge action

From the gauge transformation property of the link variable (2.2), it is clear that loop objects are gauge invariant. The simplest one is the so-called plaquette variable (see Fig. 2.1) defined as

$$\Box_{\mu\nu,x} := U_{\mu,x} U_{\nu,x+\hat{\mu}} U_{\mu,x+\hat{\nu}}^{\dagger} U_{\nu,x}^{\dagger} \tag{2.5a}$$

$$= \exp\left(ia^2 g F_{\mu\nu,x}\right), \tag{2.5b}$$

where

$$aF_{\mu\nu,x} = (A_{\nu,x+\hat{\mu}} - A_{\nu,x}) - (A_{\mu,x+\hat{\nu}} - A_{\mu,x}) \tag{2.6}$$

is the field strength on a lattice. In the continuum limit $ag \to 0$, we can easily confirm that the plaquette gauge action

$$S_g = \frac{1}{(ag)^2} \sum_x \sum_{\mu>\nu} \mathrm{Re}(1 - \Box_{\mu\nu,x}) \tag{2.7}$$

converges to the gauge action in the continuum

$$\int d^2x \, \frac{1}{4} F_{\mu\nu} F_{\mu\nu}. \tag{2.8}$$

2.1.2 θ term on a lattice

Using the principle value of the field strength on a lattice

$$a^2 g F_{01} =: a^2 g G_{01} + 2\pi n_{01}, \quad a^2 g G_{01} \in [-\pi, \pi), \quad n_{01} \in \mathbb{Z}, \tag{2.9}$$

22

a lattice discretization of the θ term can be obtained as [24]

$$Q = \int d^2x \, \frac{g}{2\pi} F_{01} \to \sum_x a^2 \frac{g}{2\pi} G_{01,x} = \frac{1}{2\pi} \sum_x a^2 g G_{01,x}. \tag{2.10}$$

With periodic boundary conditions in both spatial and imaginary time directions, Q is guaranteed to be an integer, as the summation of the field strength at all sites vanishes

$$\sum_x a^2 g F_{01,x} = 0. \tag{2.11}$$

2.1.3 Fermion doubling problem

We next consider the lattice discretization of the fermion action

$$\int d^2x \, \overline{\psi}(\gamma_\mu D_\mu + m)\psi. \tag{2.12}$$

We readily find that the naive lattice fermion action

$$a \sum_x \left[\frac{1}{2} \left(\overline{\psi}_x \gamma_\mu U_{x,\mu} \psi_{x+\hat{\mu}} \psi_{x+\hat{\mu}} - \overline{\psi}_x \gamma_\mu U^{\dagger}_{\mu,x-\hat{\mu}} \psi_{x-\hat{\mu}} \right) + m a \overline{\psi}_x \psi_x \right] \tag{2.13}$$

converges to the continuum action and is gauge invariant. However, it is well known that the naive lattice action (2.13) describes four-flavor fermions of mass m. This can be seen from the Feynman propagator for the fermion field of mass m on a lattice:

$$\Delta\left(x; m; \frac{1}{a}\right) := \left\langle (\psi_x)_\alpha \left(\overline{\psi}_0\right)_\beta \right\rangle_{U=1} \tag{2.14a}$$

$$= \frac{1}{a} \int_{-\pi}^{\pi} \frac{d^2k}{(2\pi)^2} e^{ikx} \frac{[-i\gamma_\mu \sin(k_\mu) + ma]_{\alpha\beta}}{\sum_\mu \sin^2(k_\mu) + (ma)^2}, \tag{2.14b}$$

where α, β denote the spinor indices. Thus, in the lattice discretization, the momentum in each direction is transformed from $\hat{k}_\mu = k_\mu$ to $\hat{k}_\mu = \sin(k_\mu)$. Figure 2.2 shows the behavior of the momentum in the continuum and on a lattice. We find that the lattice momentum has two zero points at $k_\mu = 0, \pi$ for each direction. Therefore, the naive lattice action describes a one-flavor fermion and three doublers. This problem is known as the fermion doubling problem.

The appearance of the three doublers is related to the absence of the chiral anomaly in the naive lattice formulation of the Dirac fermion. The Nielsen–Ninomiya theorem [59, 60] states that if a lattice fermion satisfies the following conditions:

- chiral symmetry,

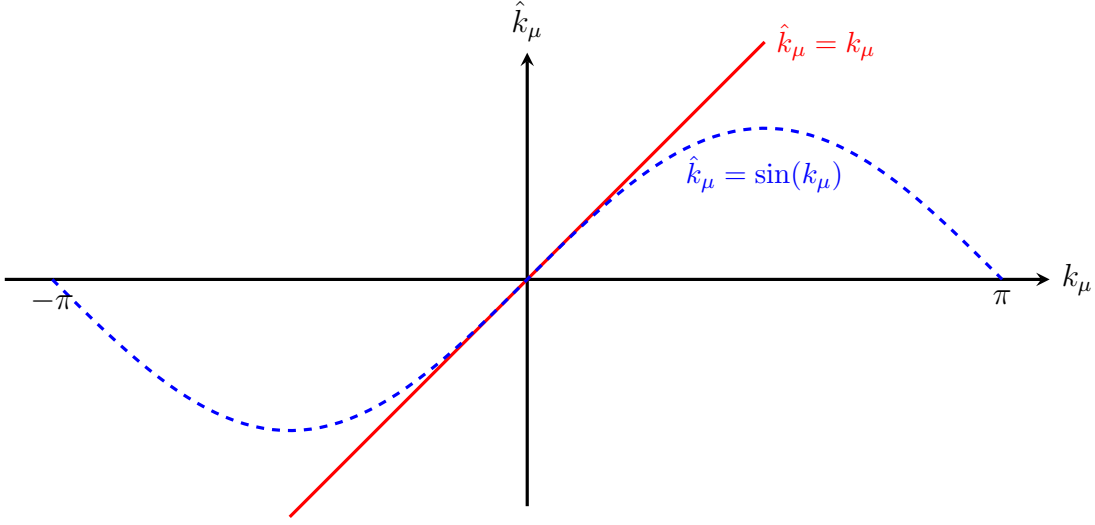- translational invariance,

- hermiticity,

Figure 2.2: Behavior of the momentum $\hat{k}_\mu$ in the continuum (solid curve) and on a lattice (dashed curve) in $k_\mu \in [-\pi, \pi]$

- bilinear form of the fermion field,

- locality,

the doublers emerge so as to cancel out the chiral anomaly. Hence, it is difficult to formulate a chiral fermion on a lattice while preserving the chiral anomaly intact.

2.1.4 Wilson fermion

To achieve a one-flavor fermion in $1+1$ dimensions, the Wilson fermion is the simplest lattice discretization. The Wilson fermion is defined by adding the Wilson term

$$-a \int d^2x \, \overline{\psi} D_\mu D_\mu \psi \to -a \sum_x \left[\frac{1}{2} \left(\overline{\psi}_x U_{x,\mu} \psi_{x+\hat{\mu}} + \overline{\psi}_x U^\dagger_{\mu,x-\hat{\mu}} \psi_{x-\hat{\mu}} \right) - 2\overline{\psi}_x \psi_x \right], \qquad (2.15)$$

which vanishes in the continuum limit, to the naive lattice fermion action (2.13). The Wilson fermion formulation of the action is given by

$$S_f = a \sum_{x,y} \overline{\psi}_x D_{x,y}(m) \psi_y, \qquad (2.16)$$

$$D_{x,y}(m) = \frac{1}{2} \left\{ (\gamma_\mu - 1) U_{\mu,x} \delta_{y,x+\hat{\mu}} - (\gamma_\mu + 1) U^\dagger_{\mu,x-\hat{\mu}} \delta_{y,x-\hat{\mu}} \right\} + (ma + 2)\delta_{y,x}. \qquad (2.17)$$

The Feynman propagator is modified as

$$\Delta\left(x; m; \frac{1}{a} \right) := \left\langle (\psi_x)_\alpha (\overline{\psi}_0)_\beta \right\rangle_{U=1} \qquad (2.18a)$$

$$= \frac{1}{a} \int_{-\pi}^{\pi} \frac{d^2k}{(2\pi)^2} e^{ikx} \frac{[-i\gamma_\mu \sin(k_\mu) + \tilde{m}a]_{\alpha\beta}}{\sum_\mu \sin^2(k_\mu) + (\tilde{m}a)^2}, \qquad (2.18b)$$

24

where $\tilde{m}$ is the modified mass, which depends on the momentum as

$$\tilde{m}(k) = m + \frac{1}{a} \sum_\mu (1 - \cos k_\mu) \tag{2.19a}$$

$$= \begin{cases} m, & k_0 \to 0 \quad \text{and} \quad k_1 \to 0, \\ m + \mathcal{O}(1/a), & k_0 \to \pi \quad \text{or} \quad k_1 \to \pi. \end{cases} \tag{2.19b}$$

Thus, the Wilson term works to make the mass of the three doublers infinitely large in the continuum limit.

In the Wilson fermion, the Nielsen–Ninomiya theorem is evaded by explicitly breaking the chiral symmetry. Consequently, the chiral anomaly is tainted by the finite lattice spacing effect. Although the recovery of the chiral anomaly is naively anticipated in the continuum limit, it remains theoretically unclear whether this expectation is realized. Additionally, since our numerical data from computer simulations are restricted to finite lattice spacings, nontrivial contamination could lead to incorrect conclusions about the continuum model.

Other than the Wilson fermion, various lattice fermions, such as the Kogut–Susskind fermion and the overlap fermion, have been proposed for a better lattice formulation of QCD [61]. In particular, the Kogut–Susskind fermion has been widely used in practical numerical simulations due to its low numerical cost. However, at least naively, the Kogut–Susskind fermion can not describe a one-flavor fermion in $1+1$ dimensional Euclidean space-time, as explained in subsection 2.2.1.

2.1.5 Numerical method

We here discuss the numerical method to simulate the Schwinger model using lattice gauge theory in Euclidean space-time. The expectation value of an observable $O(U)$ is written as

$$\langle O(U) \rangle = \frac{\int DU D\overline{\psi} D\psi \, O(U) \exp(-S_g - S_f - i\theta Q)}{\int DU D\overline{\psi} D\psi \, \exp(-S_g - S_f - i\theta Q)}, \tag{2.20}$$

where the lattice actions are given in Eqs (2.7, 2.10, 2.16). Since the Grassmann number can not be treated on a computer in the Monte Carlo method, the integration over the fermion field must be performed in advance as

$$\langle O(U) \rangle = \frac{\int DU \, \det(D(m)) O(U) \exp(-S_g - i\theta Q)}{\int DU \, \det(D(m)) \exp(-S_g - i\theta Q)}, \tag{2.21}$$

where $D(m)$ is the kernel of the Wilson fermion (2.17).

There are two difficulties in simulating the Schwinger model by the Monte Carlo method using the present lattice formulation. One difficulty comes from the fermionic determinant $\det(D(m))$, which breaks the locality of the action. Although the generation of the Monte Carlo configurations is commonly performed using the hybrid Monte Carlo method [62, 61] in this case, the large-scale linear equation for the Wilson kernel must be solved repeatedly.

As the fermion mass decreases, the diagonal components of the Wilson kernel become small, leading to a significant increase in the numerical cost of solving the linear equation.

Another difficulty is, of course, the sign problem. Although various approaches to overcome the sign problem within the Euclidean formulation, such as the reweighting method, the Lefschetz thimble method, and the complex Langevin method, have been proposed, simulating the Schwinger model at large θ is still very challenging. At present, the most successful approach would be the Grassmann tensor renormalization group [63], in which the Grassmann number can be directly treated [23, 24].

2.2 Spin Hamiltonian formulation

After explaining lattice gauge theory in Euclidean space-time, we next apply it to the lattice discretization of the Hamiltonian (1.44b). Since only spatial direction is discretized in the Hamiltonian formalism, the naive lattice fermion describes two-flavor fermions. We here employ the Kogut–Susskind fermion [64], also known as the staggered fermion, to formulate a one-flavor fermion and derive the spin Hamiltonian formulation of the Schwinger model by applying the Jordan–Wigner transformation [65].

2.2.1 Kogut–Susskind fermion

The basic idea of the Kogut–Susskind fermion is to construct the fermion field, which is two-component in the Schwinger model, from 2^d-flavor one-component fermion field, where d is the number of lattice discretized directions. Thus, in the lattice Euclidean formulation ($d = 2$), we can construct two-flavor fermions. On the other hand, in the Hamiltonian formulation, the Kogut-Susskind formulation allows us to construct a one-flavor fermion since only the spatial direction is discretized ($d = 1$).

Let the number of the spatial lattice sites L_x be even. The Dirac fermion is constructed by the one-component fermion field, the staggered field, at even and odd adjacent sites as

$$\psi_x \leftrightarrow \frac{1}{\sqrt{2a}} \begin{pmatrix} \chi_{2[x/2]} \\ \chi_{2[x/2]+1} \end{pmatrix}, \quad x = 0, \ldots, L_x/2 - 1, \tag{2.22}$$

where $[r]$ denotes the largest integer that is even or smaller than a real number r. We introduce the link variable corresponding to the gauge field A^1 as

$$U_x \leftrightarrow e^{-iagA^1(x)}. \tag{2.23}$$

It is important to notice that the effective lattice spacing between the adjacent Dirac field is now $2a$. Hence, the doubling problem is avoided because the integration interval in momentum space is now $k \in [-\pi/2, \pi/2]$.

The (anti)commutation relations in the continuum (1.45, 1.46, 1.47) are now expressed

as

$$\{\chi_x, \chi_y^\dagger\} = \delta_{xy}, \tag{2.24}$$

$$\{\chi_x, \chi_y\} = \{\chi_x^\dagger, \chi_y^\dagger\} = 0, \tag{2.25}$$

$$[U_x, -E_y] = g\delta_{xy}U_x, \tag{2.26}$$

respectively. Using the Dirac representation of the gamma matrices

$$\gamma^0 = \sigma^3, \quad \gamma^1 = i\sigma^2, \quad \gamma^5 = \gamma^0\gamma^1 = \sigma^1, \tag{2.27}$$

the Hamiltonian (1.39) is expressed in terms of the staggered field as

$$aH = \frac{(ag)^2}{2}\sum_{x=0}^{L_x-2}\left(\frac{E}{g} - \frac{\theta}{2\pi}\right)^2 - \frac{i}{2}\sum_{x=0}^{L_x-2}\left(\chi_x^\dagger U_x \chi_{x+1} - \chi_{x+1}^\dagger U_x^\dagger \chi_x\right) + ma\sum_{x=0}^{L_x-1}(-1)^x\chi_x^\dagger\chi_x, \tag{2.28}$$

where the open boundary condition is imposed for later convenience.

2.2.2 Elimination of the gauge field

The Gauss law (1.43) is now written as

$$E_x - E_{x-1} + g\left(\chi_x^\dagger\chi_x - \frac{1-(-1)^x}{2}\right) = 0. \tag{2.29}$$

In the open boundary condition, the Gauss law is solved as

$$E_x = -g\sum_{y=0}^x\left(\chi_y^\dagger\chi_y - \frac{1-(-1)^y}{2}\right), \tag{2.30}$$

where the boundary term is neglected as it can be absorbed into θ. The gauge field A^1 is also eliminated by the following redefinition of the staggered field:

$$\chi_x =: \left(\prod_{y=0}^{x-1} U_y^\dagger\right)\chi_x', \tag{2.31}$$

$$\chi_x^\dagger =: (\chi_x^\dagger)'\left(\prod_{y=0}^{x-1} U_y\right), \tag{2.32}$$

as

$$\chi_x^\dagger U_x \chi_{x+1} = \left(\chi_x^\dagger\right)'\chi_{x+1}', \tag{2.33}$$

$$\chi_{x+1}^\dagger U_x^\dagger \chi_x = \left(\chi_{x+1}^\dagger\right)'\chi_x'. \tag{2.34}$$

It is important to note that the set of the transformations (2.31, 2.32) is not a gauge transformation since no transformation has been performed on the link variable. However, if we

focus only on the staggered field, it is a gauge transformation. Therefore, when considering gauge invariant quantities composed of the staggered field, we need not distinguish between χ and χ'. Henceforth, we write χ' as χ. The lattice Hamiltonian can now be expressed solely in terms of the staggered field as

$$
aH = \frac{(ag)^2}{2} \sum_{x=0}^{L_x-2} \left\{ \sum_{y=0}^{x} \left(\chi_y^\dagger \chi_y - \frac{1-(-1)^y}{2} \right) + \frac{\theta}{2\pi} \right\}^2
$$
$$
- \frac{i}{2} \sum_{x=0}^{L_x-2} \left(\chi_x^\dagger \chi_{x+1} - \chi_{x+1}^\dagger \chi_x \right) + ma \sum_{x=0}^{L_x-1} (-1)^x \chi_x^\dagger \chi_x. \tag{2.35}
$$

2.2.3 Map to a spin system

The lattice Hamiltonian (2.35) can be transformed into a spin system by using the Jordan–Wigner transformation [65]

$$
\chi_x = \frac{X_x - iY_x}{2} \prod_{y=0}^{x-1} (-iZ_y), \tag{2.36}
$$

$$
\chi_x^\dagger = \frac{X_x + iY_x}{2} \prod_{y=0}^{x-1} (iZ_y), \tag{2.37}
$$

where X_x, Y_x, Z_x denote the Pauli matrices $\sigma^1, \sigma^2, \sigma^3$ that reside on a spatial site x, respectively. The resulting spin Hamiltonian formulation of the Schwinger model reads

$$
aH = \frac{(ag)^2}{2} \sum_{x}^{L_x-2} \left(\sum_{y=0}^{x} \frac{Z_y + (-1)^y}{2} + \frac{\theta}{2\pi} \right)^2
$$
$$
+ \frac{1}{4} \sum_{y=0}^{L_x-2} (X_x X_{x+1} + Y_x Y_{x+1}) + \frac{ma}{2} \sum_{x=0}^{L_x-1} (-1)^x Z_x. \tag{2.38}
$$

In Ref. [66], the lattice spacing dependence of the vacuum expectation value of the chiral condensate at $m = 0$ was investigated using the spin Hamiltonian (2.38). It was found that the analytically exact chiral condensate (1.23) is reproduced only after taking the continuum limit. This contradicts the fact that the chiral anomaly is independent of the ultraviolet regulator of the model. Hence, we can deduce that the chiral anomaly is tainted by the finite lattice spacing effects in the Kogut–Susskind fermion formulation, similar to the Wilson fermion formulation.

2.2.4 Numerical method

The most significant feature of the spin Hamiltonian formulation (2.38) is that the Hamiltonian is expressed in terms of the Pauli matrices, and the dimension of the Hamiltonian is

finite, albeit exponentially large 2^{L_x}. Therefore, the spin Hamiltonian is an ideal formulation for the tensor network method [20, 21, 22, 23, 24, 25, 26, 27, 28, 29, 30, 31, 32, 33] and quantum computing [34, 35, 36, 37, 38, 39, 40, 41, 42, 43].

In contrast to the Monte Carlo method, evaluation of the thermal expectation value is generally more difficult than the vacuum expectation value in the Hamiltonian formalism. In Refs. [26, 28, 29], the Schwinger model at finite temperature was investigated using the matrix product operators. It was found that the precision of the numerical results becomes worse as the temperature increases.

2.3   Lattice bosonized Schwinger model

We finally introduce the lattice formulation of the bosonized Hamiltonian (1.62). The lattice discretization of the free bosonic part is straightforward: define the scalar field and its conjugate momenta on a site and replace the derivative with the forward derivative

$$\partial_x \phi(x) \to \frac{1}{a} \partial_x \phi_x := \frac{\phi_{x+1} - \phi_x}{a}. \tag{2.39}$$

The lattice discretization of the chiral condensate

$$\overline{\psi}\psi = -\frac{e^{\gamma}}{2\pi^{3/2}} g \mathcal{N}_{g/\sqrt{\pi}} \cos\left(2\sqrt{\pi}\phi\right) \tag{2.40}$$

can be done by replacing the Feynman propagator, which appears in removing the normal ordering as explained in subsection 1.3.1, with that on a lattice [67]

$$\Delta\left(x; \mu; \frac{1}{a}\right) = \int_{-\pi}^{\pi} \frac{d^2 k}{(2\pi)^2} e^{ikx} \Delta(k, a\mu), \tag{2.41}$$

$$\Delta(k, a\mu) = \left(4 \sum_{\mu} \sin^2\left(\frac{k_{\mu}}{2}\right) + (a\mu)^2\right)^{-1} \tag{2.42}$$

as

$$\mathcal{N}_{g/\sqrt{\pi}} \exp\left(i2\sqrt{\pi}\phi_x\right) = \mathcal{O}(1/ag) \exp\left(i2\sqrt{\pi}\phi_x\right), \tag{2.43}$$

$$\mathcal{O}(1/ag) := \exp\left\{2\pi\Delta\left(0; \frac{g}{\sqrt{\pi}}; \frac{1}{a}\right)\right\}. \tag{2.44}$$

The factor $\mathcal{O}(1/ag)$ defined here appears frequently throughout this thesis, and we call it the ultraviolet (UV) divergent factor since it is divergent in the continuum limit $ag \to 0$. Figure 2.3 shows the lattice spacing dependence of the UV divergent factor (2.44). We find that the UV divergent factor behaves as $\mathcal{O}(1/ag) \simeq 10/ag$ at $ag \ll 1$.
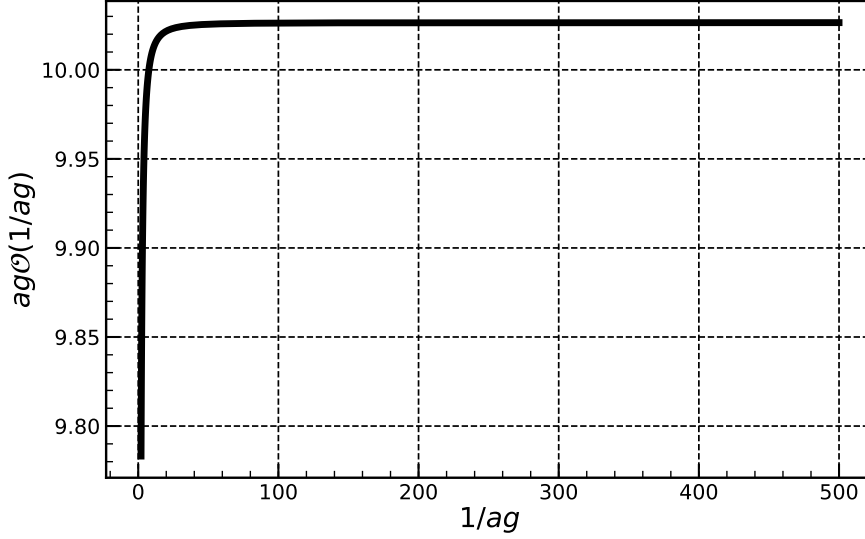
Figure 2.3: Lattice spacing dependence of the UV divergent factor (2.44).

The lattice counterpart of the bosonized Hamiltonian (1.62) can now be expressed without using the normal ordering

$$aH = \sum_{x=0}^{L_x-1} \frac{1}{2}(a\pi_x)^2 + \frac{1}{2}(\partial_x\phi_x)^2 + \frac{(ag)^2}{2\pi}\left(\phi_x + \frac{\theta}{2\sqrt{\pi}}\right)^2$$
$$- \frac{e^\gamma}{2\pi^{3/2}} \frac{m}{g}(ag)^2 \mathcal{O}(1/ag)\cos(2\sqrt{\pi}\phi_x). \tag{2.45}$$

Since bosonization is performed on an infinite line (1.62), the spatial length $L_x ag$ should be infinitely large in principle. However, in practical numerical simulations, L_x must be finite and some boundary condition must be specified. Throughout this thesis, we impose the periodic boundary condition to preserve the translational symmetry and expect that the boundary condition becomes irrelevant in the large spatial length limit $L_x ag \to \infty$.

The thermal expectation value of an observable $O(\phi)$ at temperature $T/g = (L_\tau ag)^{-1}$ can be expressed using the path-integral

$$\langle O(\phi) \rangle = \operatorname{tr} O(\phi)e^{-H/T}/\operatorname{tr} e^{-H/T} \tag{2.46a}$$

$$= \int D\phi\, O(\phi)e^{-S_E} \bigg/ \int D\phi\, e^{-S_E}, \tag{2.46b}$$

where S_E is the lattice Euclidean action of the bosonized Schwinger model

$$S_E = \sum_{\tau=0}^{L_\tau-1}\sum_{x=0}^{L_x-1} \frac{1}{2}(\partial_\tau\phi_{x,\tau})^2 + \frac{1}{2}(\partial_x\phi_{x,\tau})^2 + \frac{(ag)^2}{2\pi}\left(\phi_{x,\tau} + \frac{\theta}{2\sqrt{\pi}}\right)^2$$
$$- \frac{e^\gamma}{2\pi^{3/2}}\frac{m}{g}(ag)^2\mathcal{O}(1/ag)\cos(2\sqrt{\pi}\phi_{x,\tau}). \tag{2.47}$$

30

The periodic boundary condition must be imposed for the imaginary time direction since the scalar field is bosonic. We stress that the analytic continuation is not used from Eq. (2.46a) to Eq. (2.46b); we just need the completeness relations and the canonical commutation relations among the bosonic operators.

The CP symmetry in the Euclidean action becomes more transparent by shifting the scalar field $\phi + \frac{\theta}{2\sqrt{\pi}} \to \phi$. After the shift, the Euclidean action (2.47) becomes

$$
\begin{aligned}
S_E = \sum_{\tau=0}^{L_\tau-1} \sum_{x=0}^{L_x-1} & \frac{1}{2}(\partial_\tau \phi_{x,\tau})^2 + \frac{1}{2}(\partial_x \phi_{x,\tau})^2 + \frac{(ag)^2}{2\pi}(\phi_{x,\tau})^2 \\
& - \frac{e^\gamma}{2\pi^{3/2}} \frac{m}{g}(ag)^2 \mathcal{O}(1/ag) \cos\big(2\sqrt{\pi}\phi_{x,\tau} - \theta\big),
\end{aligned} \tag{2.48}
$$

and the electric field (1.61) is expressed as

$$
E = \frac{g}{\sqrt{\pi}}\phi, \tag{2.49}
$$

respectively. We find that the Euclidean action (2.48) is indeed symmetric at $\theta = 0, \pi$ under the CP transformation $\phi \to -\phi$. The 2π periodicity of the θ angle is also apparent now.

In the present lattice discretization, the fermion doubling problem does not emerge from the beginning as the fermion is transformed into boson in the continuum. Thus, bosonization provides a novel lattice fermion formulation, which is independent of the specific choice of the lattice fermions.

One of the other advantages of the lattice bosonized Schwinger model is that the chiral anomaly remains intact. This is obvious from the chiral transformation property in the bosonized Hamiltonian, as described in subsection 1.3.1. Indeed, in Chapter 3, we find that the analytically exact chiral condensate (1.23), which arises from the chiral anomaly, is completely reproduced at any lattice spacing, as long as the system size $L_x ag$ is sent to infinity.

We note that the method of addressing the normal ordering on a lattice was initially proposed by Bender, Rothe, and Rothe in 1985 [67] to numerically obtain the static potential at $\theta = 0$ by evaluating its ground state energy in the presence of static probe charges. In their paper, the cosine term in the bosonized Hamiltonian was introduced symbolically as

$$
\frac{M^2}{4\pi}\cos\big(2\sqrt{\pi}\phi\big) \tag{2.50}
$$

without explicitly specifying the scale of the normal ordering or the relation between M and the fermion mass m. Probably because of the absence of the explicit prefactor in terms of the fermion mass m, their paper has not received much attention to date despite its significance. Their method was recently rediscovered, and the correct prefactor of the cosine term was explicitly described by the author in Ref. [1].

2.3.1 Numerical method

The thermal expectation value (2.46b) can be evaluated by the Monte Carlo method. The Monte Carlo configurations can be easily generated by combined use of the heat-bath algorithm and the rejection sampling, just like the case of SU(2) Yang–Mills theory [68]. This allows for low-cost Monte Carlo simulations. In the heat-bath algorithm, each update of the Monte Carlo configuration $\{\phi_{x,\tau}\}$ consists of updating the scalar field $\phi_{x,\tau}$ at each site with the probability density $P(\phi_{x,\tau}) \propto \exp(-S_E^{x,\tau})$, where $S_E^{x,\tau}$ is the part of the lattice Euclidean action (2.48) dependent on $\phi_{x,\tau}$:

$$S_E^{x,\tau} = 2\big(\phi_{x,\tau} - \overline{\phi}_{x,\tau}\big)^2 + \frac{(ag)^2}{2\pi}\phi_{x,\tau}^2 - C(ag)\cos\big(2\sqrt{\pi}\phi_{x,\tau} - \theta\big), \tag{2.51}$$

$$\overline{\phi}_{x,\tau} := \frac{\phi_{x+1,\tau} + \phi_{x-1,\tau} + \phi_{x,\tau+1} + \phi_{x,\tau-1}}{4}, \tag{2.52}$$

$$C(ag) := \frac{e^{\gamma}}{2\pi^{3/2}}\frac{m}{g}(ag)^2\mathcal{O}(1/ag). \tag{2.53}$$

To update the scalar field $\phi_{x,\tau}$ with the probability density $P(\phi_{x,\tau}) \propto \exp(-S_E^{x,\tau})$, the rejection sampling can be used in the following steps:

1. Generate a Gaussian random number g with the probability density $P(g) \propto \exp(-2g^2)$.

2. Set the trial scalar field $\phi_{x,\tau}^{\text{trial}} = \overline{\phi}_{x,\tau} + g$.

3. Generate a uniform random number $r \in [0, 1]$.

4. If $r \exp\{C(ag)\} < \exp\Big\{C(ag)\cos\big(2\sqrt{\pi}\phi_{x,\tau}^{\text{trial}} - \theta\big) - \frac{(ag)^2}{2\pi}\big(\phi_{x,\tau}^{\text{trial}}\big)^2\Big\}$, accept the trial scalar field $\phi_{x,\tau}^{\text{new}} = \phi_{x,\tau}^{\text{trial}}$; otherwise, reject the trial scalar field.

For an efficient rejection sampling, a high acceptance rate at the fourth step is crucial. In practical simulations near the continuum limit $ag \ll 1$, the small values of the prefactors $C(ag), (ag)^2/2\pi$ lead to high acceptance rates. For example, the acceptance rate is approximately 93% in the equilibrium at $ag = 0.1, m/g = 0.5, \theta = 0$.

The sign problem is circumvented since lattice Euclidean action (2.47) is real and bounded below even at $\theta \neq 0$. The absence of the sign problem is related to excluding the gauge degrees of freedom and obtaining the Euclidean action (2.47) without the need for the analytic continuation. This was pointed out and utilized for the first time by the author in Ref. [1].

Unfortunately, the vacuum expectation value can not be evaluated directly since the limit $L_\tau ag \to \infty$ can not be taken on a computer. While the thermal expectation value at almost zero temperature can be obtained by setting $L_\tau ag$ large, exact zero temperature can be important in certain cases in $1 + 1$ dimensions, as we will see in Chapter 5.

2.4 Comparison of the three lattice formulations

In this chapter, we have discussed the three lattice formulations of the Schwinger model. A summary of the comparison among them is shown in Table 2.1. As evident from the lattice

Table 2.1: Summary of the comparison among the three lattice formulations of the Schwinger model.

	Lattice gauge	Spin Hamiltonian	Lattice bosonized
Main numerical method	Monte Carlo	Tensor Network	Monte Carlo
Sign problem	exist	not exist	not exist
Lattice fermion dependence	exist	exist	not exist
Chiral anomaly	tainted	tainted	intact
Zero temperature	impossible	possible	impossible
Finite temperature	easy	difficult	easy
Numerical cost	high	medium	low

fermion independence and the preservation of the chiral anomaly at finite lattice spacing, the lattice bosonized Schwinger model stands out as the theoretically cleanest lattice formulation. Furthermore, for our purpose in this thesis, which is to investigate the interplay between the quantum effects of the θ term and thermal effects through first-principle calculations, the Monte Carlo study of the lattice bosonized Schwinger model would be the most practical method.

Chapter 3

Verification of the lattice bosonized Schwinger model

While the lattice bosonized Schwinger model is expected to be useful for investigating the finite temperature and θ region of the Schwinger model, it is important to perform an explicit verification before using it to explore new properties of the model. Such verification had never been done before. In this chapter, we verify the lattice bosonized Schwinger model (2.47) by reproducing analytical and numerical results in the literature. As an observable, we mainly focus on the chiral condensate

$$\overline{\psi}\psi = -\frac{e^{\gamma}}{2\pi^{3/2}} g \mathcal{N}_{g/\sqrt{\pi}} \cos\left(2\sqrt{\pi}\phi\right) \tag{3.1a}$$

$$= -\frac{e^{\gamma}}{2\pi^{3/2}} g \mathcal{O}(1/ag) \cos\left(2\sqrt{\pi}\phi\right), \tag{3.1b}$$

because it is directly related to the nontrivial normal ordering.

3.1 Analyical expression of the chiral condensate for a massless fermion

We first derive the analytical expression for the chiral condensate at $m = 0$ and $\theta = 0$

$$\left\langle\overline{\psi}\psi\right\rangle_{\text{lat.}} = -\frac{e^{\gamma}}{2\pi^{3/2}} g \mathcal{O}(1/ag) \left\langle\cos\left(2\sqrt{\pi}\phi\right)\right\rangle \tag{3.2}$$

at zero and finite temperatures. Using Wick's theorem, the thermal expectation value of $\exp(i\beta\phi)$ is analytically obtained as

$$\langle\exp(i\beta\phi)\rangle = \exp\left\{-\frac{\beta^2}{2}\Delta\left(0; \frac{g}{\sqrt{\pi}}; \frac{1}{a}\right)_{L_x, L_\tau}\right\}, \tag{3.3}$$

where $\Delta(0; \mu; 1/a)_{L_x, L_\tau}$ is the Feynman propagator in the lattice system with $L_x \times L_\tau$ sites in the periodic boundary conditions. Its explicit form is given by

$$\Delta\left(x; \mu; \frac{1}{a}\right)_{L_x, L_\tau} = \frac{1}{L_x L_\tau} \sum_{k_x = 2\pi/L_x, 4\pi/L_x, \ldots}^{2\pi} \sum_{k_\tau = 2\pi/L_\tau, 4\pi/L_\tau, \ldots}^{2\pi} e^{ikx} \Delta(k, a\mu), \qquad (3.4)$$

where $\Delta(k, a\mu)$ is the lattice Feynman propagator in the momentum space (2.42). Hence, we obtain

$$\langle \overline{\psi}\psi \rangle_{\text{lat.}} = -\frac{e^\gamma}{2\pi^{3/2}} g \exp\left[-2\pi\left\{\Delta\left(0; \frac{g}{\sqrt{\pi}}; \frac{1}{a}\right)_{L_x, L_\tau} - \Delta\left(0; \frac{g}{\sqrt{\pi}}; \frac{1}{a}\right)\right\}\right]. \qquad (3.5)$$

The vacuum expectation value of the chiral condensate in the lattice bosonized Schwinger model is obtained by setting the system size and the extent in the imaginary time direction infinity

$$L_x ag \to \infty, \quad L_\tau ag \to \infty. \qquad (3.6)$$

In these limits, the argument of the exponential in Eq. (3.5) becomes zero, and the analytically exact chiral condensate

$$\langle \overline{\psi}\psi \rangle_{\text{cont.}} = -\frac{e^\gamma}{2\pi^{3/2}} g \qquad (3.7)$$

is reproduced. Thus, we find that the analytically exact chiral condensate is reproduced at any lattice spacing ag, as long as the number of lattice sites in both directions is sent to infinity. This feature reflects the preservation of the chiral anomaly on a lattice.

The thermal expectation value of the chiral condensate at temperature $T/g = (L_\tau ag)^{-1}$ is obtained by taking the large spatial length and continuum limits

$$L_x ag \to \infty, \quad ag \to 0. \qquad (3.8)$$

In these limits, the lattice chiral condensate (3.5) converge to the analytically exact chiral condensate in the continuum [1]

$$\langle \overline{\psi}\psi \rangle_{\text{cont.}} = -\frac{e^\gamma}{2\pi^{3/2}} g \exp\left\{2I\left(\frac{g}{\sqrt{\pi}T}\right)\right\}, \qquad (3.9)$$

$$I(x) := \int_0^\infty dt \left(1 - e^{x \cosh t}\right)^{-1}, \qquad (3.10)$$

which can be obtained by directly evaluating the fermionic path-integral in the original fermionic formulation [19].

The two analytical chiral condensates on a lattice (3.5) and in the continuum (3.9) enable us to investigate the finite lattice spacing and spatial length effects at $m = 0$ analytically. The

---

[1]This expression first appeared in Ref. [16], in which the chiral condensate in the massless Schwinger model on a circle ($0 \le x < L$) was analytically obtained using bosonization in the Hamiltonian formalism. Because of the equivalence between space and time in $(1 + 1)$-dimensional Euclidean space-time, the resultant chiral condensate is equivalent to that at temperature $T = 1/L$ in the large spatial length limit.

upper half of Fig. 3.1 shows the two analytical chiral condensates (3.5, 3.9) at various lattice spacings ag and two spatial lengths $L_x ag = 11.2, 22.4$. Remarkably, we find that the lattice chiral condensate (3.5) appears to agree with the continuum one (3.9) even at a very large lattice spacing $ag = 2.8$ and high temperature. [2] For a more detailed investigation, we show the ratio of the two analytical chiral condensates (3.5, 3.9) at the same parameters in the lower half of Fig. 3.1. We find that the ag dependence is almost negligible for $ag \leq 0.2$. At $L_x ag = 11.2$, the spatial length is not satisfactory large, and some discrepancies can be seen. These discrepancies are almost absent at $L_x ag = 22.4$, except for the small discrepancies at high temperatures $(T/g)^{-1} \lesssim 1$. Those small discrepancies in the ratio should not be taken seriously because the chiral condensate is almost zero at these temperatures. We conclude that both continuum and large spatial length limits are reliably taken for $ag \lesssim 0.2, L_x ag = 22.4$ at $m = 0$. In the following numerical simulations at $m \neq 0$ in this chapter, we very conservatively use the lattice of $ag = 0.025, L_x = 896$ and generate $N_{\text{conf}} = 10^6$ Monte Carlo configurations for each measurement, unless otherwise mentioned.

3.2 Chiral condensate for a massive fermion

We next calculate the chiral condensate at $m \neq 0$ and $\theta = 0$. While there exists no analytically exact result, the chiral condensates at both zero and nonzero temperatures have been extensively studied using the tensor network method [25, 28, 29]. We compare our results with theirs and check the lattice bosonized Schwinger model. We stress that this serves as another nontrivial check since we are dealing with the normal ordering dynamically in this case. In this section, we remove the logarithmic divergence in the chiral condensate at $m \neq 0$ by subtracting the free chiral condensate at (almost) zero temperature following Refs. [25, 28, 29]. We use the jackknife method to estimate statistical errors.

The chiral condensates at $T/g = (448 \times 0.025)^{-1}$ obtained in this work and the most recent results by the tensor network method at zero temperature [28] are summarized in Table 3.1. Our numerical results match theirs with approximately one percent accuracy. It is notable that our results are obtained with no continuum nor infinite spatial length extrapolation in contrast to the tensor network calculations, although the errors are far larger. If we aim at the precision of Ref. [28] using the current lattice parameters, around $N_{\text{conf}} = 10^{10}$–$10^{12}$ configurations are required, which is not practically feasible.

The present method is advantageous against the tensor network method at finite temperatures. Figure 3.2 shows the temperature dependence of the chiral condensate at $m/g = 0.0625, 0.125, 0.25, 0.5, 1$. Our numerical results are seemingly consistent with the tensor network results by using the matrix product operator [28, 29] (see Fig. 4 in Ref. [29]), and higher precision is achieved at high temperatures. Those results provide further evidence that the lattice formulation of the bosonized Schwinger model is valid.

---

[2] In upper left of Fig. 3.1, the number of spatial sites is just $L_x = 4$ at the largest lattice spacing $ag = 2.8$. The number of temporal sites is set to $L_\tau = 1, 2, 3, 4$.
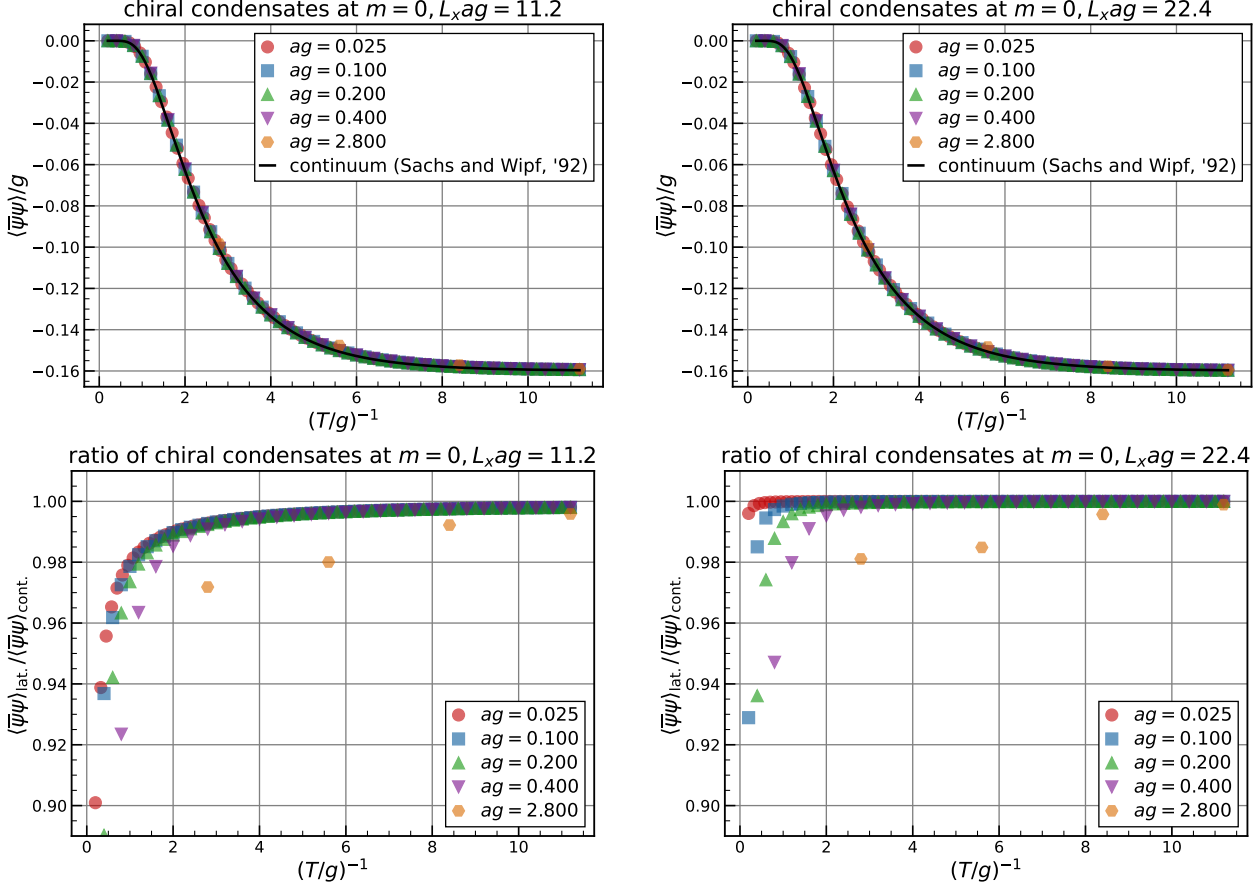
Figure 3.1: (Upper half) The two analytical chiral condensates (3.5, 3.9) as functions of temperature at $L_x ag = 11.2$ (left) and $L_x ag = 22.4$ (right). (Lower half) Ratio of the two analytical chiral condensates at the same parameters. These figures are taken from Ref. [1].

3.3 Finite θ

After verifying the lattice bosonized Schwinger model, we here explicitly confirm that high-precision calculation is possible even at $\theta \neq 0$ by studying the chiral condensate and the electric field. Figure 3.3 shows the θ dependence of the chiral condensates

$$\langle \overline{\psi}\psi \rangle_\theta = -\frac{e^\gamma}{2\pi^{3/2}} g \mathcal{O}(1/ag) \left\langle \cos\left(2\sqrt{\pi}\phi\right) \right\rangle_\theta \tag{3.11}$$

at $m/g = 0.0625, 0.125, 0.25, 0.5$. Here, Monte Carlo configurations only at $\theta \leq \pi$ are generated, and data points at $\theta > \pi$ are obtained using the line symmetry at $\theta = \pi$. The statistical errors are all smaller than the symbols, even though the chiral condensates at nonzero θ are evaluated using $N_{\text{conf}} = 10^5$ configurations. The chiral condensates at $m/g = 0.0625, 0.125, 0.25$ are compared with the leading-order mass perturbation [55, 56]

$$\langle \overline{\psi}\psi \rangle_\theta - \langle \overline{\psi}\psi \rangle_{\theta=0} = \frac{e^\gamma}{2\pi^{3/2}} g(1 - \cos\theta) - 0.358 m(1 - \cos 2\theta). \tag{3.12}$$

Table 3.1: Absolute values of the chiral condensates at $T/g = (448 \times 0.025)^{-1}$ obtained in this work, compared with the tensor network results at zero temperature [28].

m/g	This work	Ref. [28]	This work / Ref. [28]
0.0625	0.11506(91)	0.1139657(8)	1.0096(80)
0.125	0.09249(66)	0.0920205(5)	1.0051(72)
0.25	0.06629(62)	0.0666457(3)	0.9947(93)
0.5	0.04207(37)	0.0423492(20)	0.9935(87)
1	0.02385(22)	0.0238535(28)	0.9997(93)
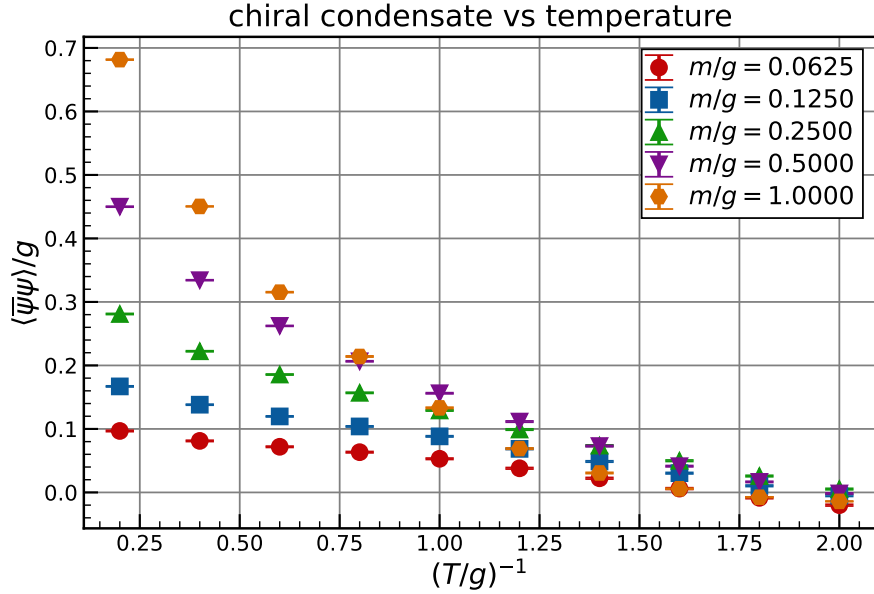
Figure 3.2: Temperature dependence of the chiral condensate at $m/g = 0.0625, 0.125, 0.25, 0.5, 1$. This figure is taken from Ref. [1].

The mass perturbation theory works well at $m/g = 0.0625, 0.125$, whereas sizable deviations appear at $m/g = 0.25$. These behaviors are consistent with the tensor network results at zero temperature [31, 32], although we are calculating the chiral condensates at very low yet not zero temperature $T/g = (448 \times 0.025)^{-1}$.

A cusp-like behavior is observed at $\theta = \pi$ for $m/g = 0.5$ in Fig. 3.3. A cusp at $\theta = \pi$ indicates the spontaneous breaking of the CP symmetry, because the θ derivative of the expectation value of the chiral condensate is calculated as

$$
\frac{\partial \langle \overline{\psi}\psi \rangle_\theta}{\partial \theta} = \frac{e^\gamma}{4\pi^2} g \mathcal{O}(1/ag) \left\{ \left\langle \left(\phi + \frac{\theta}{2\sqrt{\pi}} \right) \cos\left(2\sqrt{\pi}\phi\right) \right\rangle_\theta - \left\langle \phi + \frac{\theta}{2\sqrt{\pi}} \right\rangle \left\langle \cos\left(2\sqrt{\pi}\phi\right) \right\rangle_\theta \right\}
$$

(3.13a)

$$
= \frac{e^\gamma}{4\pi^2} g \mathcal{O}(1/ag) \left\{ \left\langle \phi \cos\left(2\sqrt{\pi}\phi - \theta\right) \right\rangle'_\theta - \left\langle \phi \right\rangle'_\theta \left\langle \cos\left(2\sqrt{\pi}\phi - \theta\right) \right\rangle'_\theta \right\},
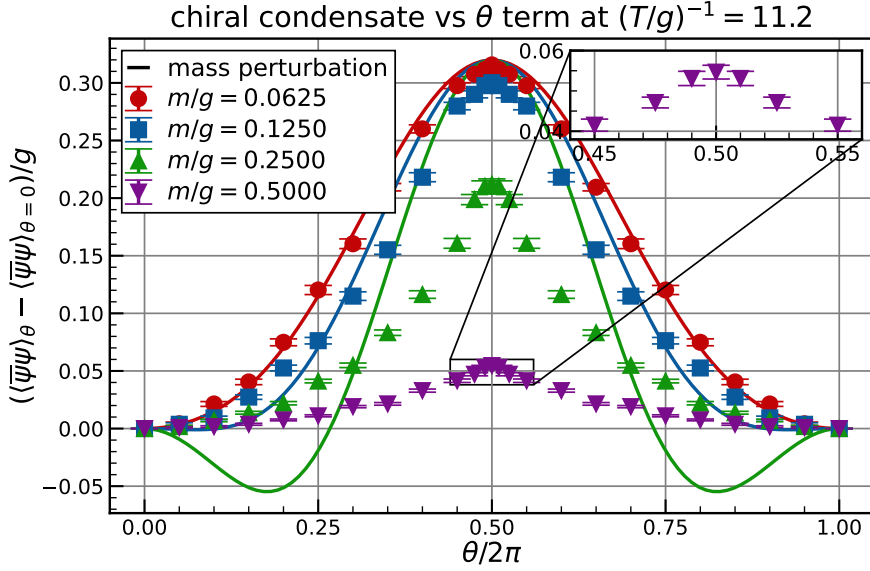$$

(3.13b)

Figure 3.3: θ dependence of the chiral condensate at $m/g = 0.0625, 0.125, 0.25, 0.5, T/g = (448 \times 0.025)^{-1}$. The chiral condensates at $m/g = 0.0625, 0.125, 0.25$ are compared with the leading-order mass perturbation (3.12) (solid line). This figure is taken from Ref. [1].

where $\langle \rangle'$ denotes the expectation value under the shifted Euclidean action (2.48). The spontaneous CP symmetry breaking can also be probed by studying the θ dependence of the electric field (1.61)

$$\langle E \rangle = \frac{g}{\sqrt{\pi}} \left\langle \phi + \frac{\theta}{2\sqrt{\pi}} \right\rangle_\theta \tag{3.14a}$$

$$= \frac{g}{\sqrt{\pi}} \langle \phi \rangle'_\theta. \tag{3.14b}$$

Figure 3.4 shows the θ dependence of the electric field at $m/g = 0.0625, 0.125, 0.25, 0.5$, evaluated using the same Monte Carlo configurations. In Fig. 3.4, we find an approximate discontinuity at $\theta = \pi$ for $m/g = 0.5$, which more directly suggests the spontaneous CP symmetry breaking. In fact, at zero temperature, it is already established that the spontaneous CP symmetry breaking occurs for sufficiently large fermion masses $m/g \gtrsim 0.33$ [66, 20, 24, 69, 40]. We investigate the fate of the CP symmetry at $\theta = \pi$ at finite temperature in Chapter 5. Remarkably, we find that the CP symmetry is restored by infinitesimally small thermal effects. Therefore, the cusp-like behavior in Fig. 3.3 can never be a genuine cusp, and the approximate discontinuity in Fig. 3.4 can never be a genuine discontinuity, even if we took the infinite spatial length limit.
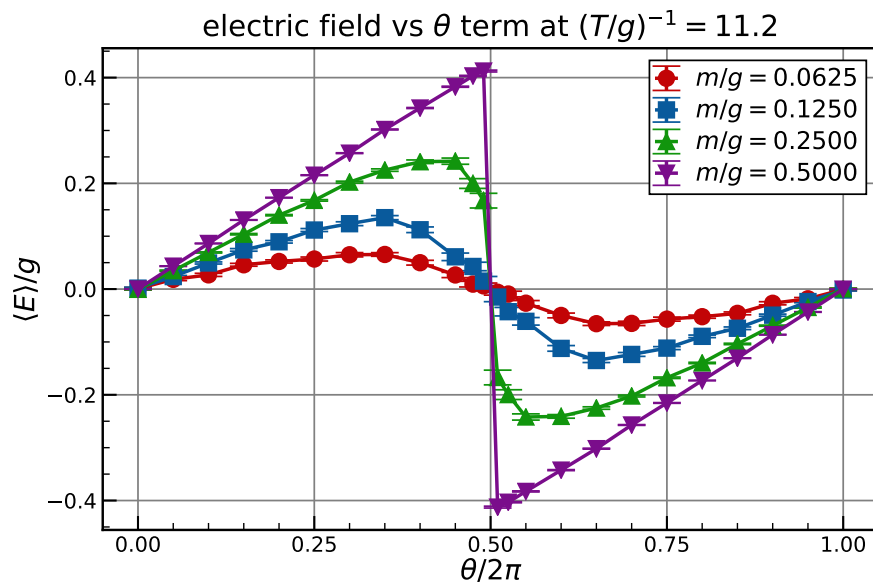
40

Figure 3.4: θ dependence of the electric field at $m/g = 0.0625, 0.125, 0.25, 0.5, T/g = (448 \times 0.025)^{-1}$.

Chapter 4

Confinement at finite temperature and θ

In this chapter, we investigate the confining properties in the Schwinger model at finite temperature and θ. In Section 4.1, we introduce the basic methodology for discussing confinement in the Schwinger model and analytically discuss confinement at $\theta = 0$. We explain our numerical method to calculate the string tension at finite temperature and θ by developing the methodology in Section 4.2. We perform an extensive calculation of the string tension at finite temperature and θ in Section 4.3.

4.1   Analytical examination of confinement

We here introduce the basic methodology for discussing confinement in preparation for the next section and summarize analytically exact results known for a long time [11] using the bosonized Schwinger model (2.47).

Consider to include the pair of static probe charges $q_p g, -q_p g$ separated by distance r in the vacuum. Since the probe charge can be treated classically, a constant electric field $E = q_p g$ appears between the two static probe charges due to the classical Gauss law, as shown in Fig. 4.1. As noted in subsection 1.3.1, the θ angle is physically interpreted as the external electric field. Hence, the inclusion of the pair of static probe charges $q_p g, -q_p g$ is equivalent to setting $\theta = 2\pi q_p$ in the interval of r. In the infinite distance limit $r \to \infty$, the linear term dominates the static potential. The string tension, the coefficient of the linear term in the static potential, can be extracted from the difference in free energy densities

$$\sigma(q_p) = f(2\pi q_p) - f(\theta = 0) = \frac{-1}{L_x L_\tau a^2} \ln \frac{Z(2\pi q_p)}{Z(0)}, \tag{4.1}$$

where $Z(\theta)$ is the partition function

$$Z(\theta) = \operatorname{tr} e^{-H(\theta)/T} \propto \int D\phi \, e^{-S_E(\theta)}. \tag{4.2}$$
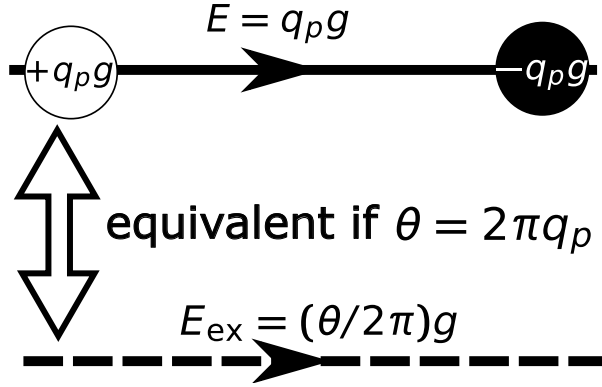
43

Figure 4.1: Schematic picture describing the equivalence between the system with the pair of static probe charges $q_p g, -g_p g$ and that with the external electric field $E_{\text{ex}} = (\theta/2\pi)g$ arising from the θ term.

From the Euclidean action of the bosonized Schwinger model (2.47), the following results can be easily drawn [11]:

- The string tension is zero at $m = 0$ since the partition function does not depend on θ.

- The string tension is zero for any integer probe charge $q_p \in \mathbb{Z}$ due to the 2π periodicity of θ.

The vanishing of the string tension for any integer probe charge $q_p \in \mathbb{Z}$ can be intuitively understood by the creation of q_p dynamical charge pairs $g, -g$ from the vacuum, which works to erase the total electric field. Conversely, the creation of these dynamical charge pairs is the physical explanation for the 2π periodicity of the θ angle. The vanishing of the string tension indicates that there is neither attractive nor repulsive force between the probe charges. Of course, this does not correspond to the isolation of charge. The integer probe charge is completely screened by dynamical charges and loses its physical presence. It is not appropriate to link the vanishing of the string tension to deconfinement in this case. On the other hand, a noninteger probe charge cannot be completely screened by dynamical charges and retain its physical presence. In the following, we mainly consider the string tension between noninteger probe charges.

4.2 Method to calculate the string tension

Extending the above methodology to finite θ is straightforward. Due to the principle of superposition, the inclusion of the two static probe charges $q_p g, -q_p g$ separated infinity to the vacuum at any θ can be described through a modification of the θ angle

$$\theta \to 2\pi q_p + \theta. \tag{4.3}$$

44

The string tension can be obtained from the difference in free energy densities

$$\sigma(q_p, \theta) = f(2\pi q_p + \theta) - f(\theta) = \frac{-1}{L_x L_\tau a^2} \ln \frac{Z(2\pi q_p + \theta)}{Z(\theta)}. \tag{4.4}$$

The computation of the free energy density itself is difficult by the Monte Carlo method since it cannot be expressed as an expectation value. However, the difference can be:

$$\sigma(q_p, \theta) = \frac{-1}{L_x L_\tau a^2} \ln \left\langle \exp \left[-\frac{(ag)^2}{\sqrt{\pi}} \sum_{x,\tau} q_p \left(\phi_{x,\tau} + \frac{\theta + \pi q_p}{2\sqrt{\pi}} \right) \right] \right\rangle_\theta. \tag{4.5}$$

In practical numerical simulations, direct evaluation using Eq. (4.5) leads to large statistical and systematic errors at large q_p. To avoid this problem, we consider to decompose the string tension at

$$q_p = N\delta q_p, \quad \theta = M\delta\theta, \quad N, M \in \mathbb{Z}, \tag{4.6}$$

where $\delta q_p, \delta\theta$ are some small step widths. Setting $\delta q_p = \delta\theta/2\pi$, the free energy density can be expressed as

$$f(2\pi q_p + \theta) = f((N+M)\delta\theta) =: f_{N+M}. \tag{4.7}$$

Using this notation, the string tension can be decomposed as

$$\sigma(N\delta q_p, M\delta\theta) = f_{N+M} - f_M \tag{4.8a}$$

$$= \sum_{i=0}^{N-1} f_{i+M+1} - f_{i+M} \tag{4.8b}$$

$$= \frac{-1}{L_x L_\tau a^2} \sum_{i=0}^{N-1} \ln \left\langle \exp \left[-\frac{(ag)^2}{\sqrt{\pi}} \sum_{x,\tau} \delta q_p \left(\phi_{x,\tau} + \frac{\theta + \pi \delta q_p}{2\sqrt{\pi}} \right) \right] \right\rangle_{\theta = (i+M)\delta\theta}. \tag{4.8c}$$

By using Eq. (4.8c) instead of Eq. (4.5), we can greatly mitigate the large statistical and systematic errors at large q_p since q_p in Eq. (4.5) is now replaced by δq_p.

4.3 Numerical results

We first check the finite lattice spacing effects in the string tension, while the spatial length is set to sufficiently large $L_x ag = 22.4$. Figure 4.2 shows the probe charge dependence of the string tension at $ag = 0.4, 0.2, 0.1$ and $m/g = 0.25, 0.5$. The results are obtained from $N_{\text{conf}} = 10^6$ configurations at θ/π ranging from 0.0 to 1.0 with a step width of $\delta\theta/\pi = 0.1$. The temperature and spatial length are held constant at $T/g = 11.2^{-1}$ and $L_x ag = 22.4$, respectively. We find that the results at $ag = 0.4, 0.2, 0.1$ exhibit exceptional precision and agreement. Motivated by this, we use the lattice of $ag = 0.2, L_x = 112$ in the following analysis.
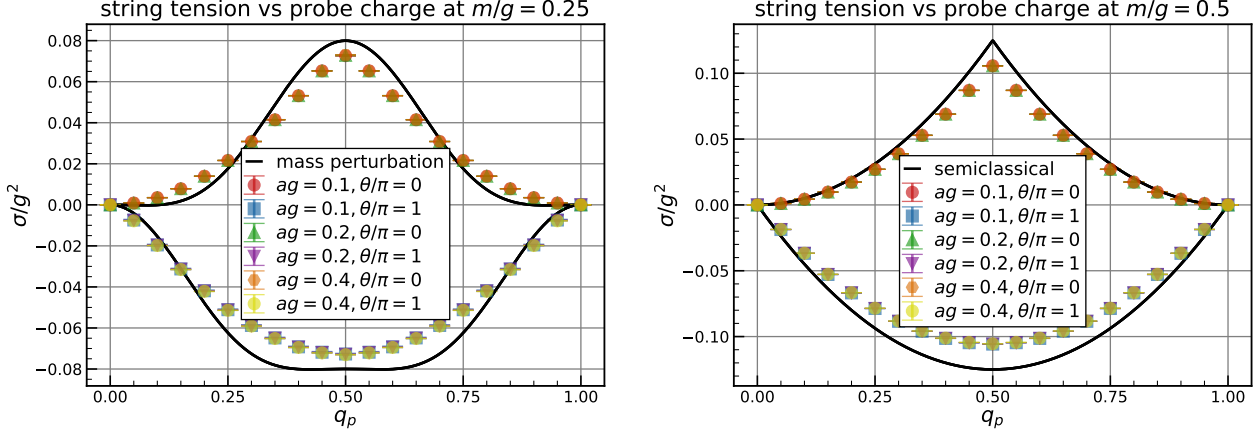
Figure 4.2: Probe charge dependence of the string tension for $\theta = 0, \pi$ at $m/g = 0.25$ (left) and $m/g = 0.5$ (right). The string tensions at $m/g = 0.25$ and $m/g = 0.5$ are compared with the mass perturbation (4.10) and the semiclassical estimates (4.9), respectively. The temperature and spatial length are held constant at $T/g = 11.2^{-1}$ and $L_x a g = 22.4$, respectively. These figures are taken from Ref. [2].

In Fig. 4.2, we observe peculiar behaviors in the string tension: at $\theta = 0$, there is a peak in the string tension at $q_p = 0.5$. More interestingly, the string tension becomes negative for noninteger probe charges at $\theta = \pi$. These behaviors can be well understood through semiclassical analysis of the string tension (see Fig. 4.3). For $q_p \in [0, 1/2], \theta = 0$, a constant electric field $E = q_p g$ appears between the two static probe charges at the classical level due to the classical Gauss law, as shown in the upper left of Fig. 4.3. Consequently, the string tension increases quadratically as the probe charge q_p increases. When q_p exceeds $1/2$, and the distance between the probe charges is sufficiently large, the vacuum produces a dynamical charge pair, reducing the total electric field by forming a two "meson" system (upper right of Fig. 4.3). Setting $\theta = \pi$, i.e., applying an external electric field $E_{ex} = g/2$, to the two "meson" system, the external electric field works to decrease the total electric field, resulting in the negative string tension. In the case of the single "meson" system (upper left of Fig. 4.3), as the external electric field approaches $g/2$, the vacuum would again produce a dynamical charge pair to decrease the total electric field by forming a two "meson" system at a certain value of θ. Therefore, at $\theta = \pi$, the configuration is the same regardless of the probe charge, as shown in the lower of Fig. 4.3. The resulting semiclassical estimate for the string tension is given by

$$\sigma/g^2 = \begin{cases} \frac{1}{2}q_p^2, & q_p \in \left[0, \frac{1}{2}\right], \theta = 0, \\ \frac{1}{2}(1 - q_p)^2, & q_p \in \left[\frac{1}{2}, 1\right], \theta = 0, \\ -\frac{1}{2}q_p(1 - q_p), & q_p \in [0, 1], \theta = \pi. \end{cases} \tag{4.9}$$

In the right panel of Fig. 4.2, we find that the semiclassical string tension (4.9) successfully
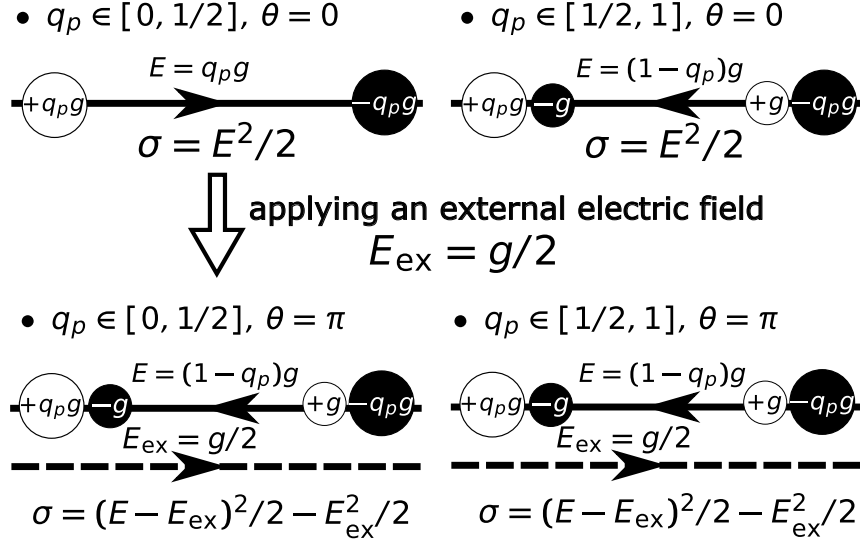
46

Figure 4.3: Semiclassical picture of the string tension between two static probe charges $q_p g, -q_p g$. This figure is taken from Ref. [2].

explains the qualitative behavior of our numerical results. [1]

While it is difficult to give an intuitive explanation for the negative string tension at small fermion mass, the next-to-leading order mass perturbation [54, 55]

$$\sigma/g^2 = \frac{e^\gamma}{2\pi^{3/2}} \frac{m}{g}(\cos(\theta) - \cos(2\pi q_p + \theta)) - 0.179\left(\frac{m}{g}\right)^2 (\cos(2\theta) - \cos(4\pi q_p + 2\theta)) \quad (4.10)$$

successfully explains the qualitative behavior, as shown in the left panel of Fig. 4.2. We note that the string tensions at $\theta = 0$ at various masses, probe charges, and temperatures have been already obtained with high precision by the tensor network method [27, 29, 31]. In the case of the charge-3 Schwinger model, the string tension between integer probe charges at nonzero θ was studied in Ref. [41] through quantum simulation on a classical simulator. Negative string tension was observed at large θ, although reliable continuum extrapolation was impossible due to a limited number of lattice sites ($L_x \leq 25$) and slow convergence to the continuum limit. In Refs. [70, 41], the negative string tension between integer probe charges in the charge-q Schwinger model, where q is an integer larger than 1, was explained in terms of the $\mathbb{Z}_q$ 1-form symmetry. Unfortunately, their argument can not be applied to the present case. Nevertheless, our numerical results demonstrate that the negative string tension appears for noninteger probe charges at almost zero temperature in the standard Schwinger model for the first time.

Let us consider the charge distribution when the probe charge is small $q_p \in (0, 1/2)$. As shown in Fig. 4.4, an attractive force appears between the noninteger probe charges at $\theta = 0$, indicating confinement. On the contrary, a repulsive force appears between the noninteger

---

[1]The cusp in the string tension at $q_p = 0.5$ corresponds to the spontaneous breaking of the CP symmetry, similar to the chiral condensate.

probe charges at $\theta = \pi$, indicating that the pair of the probe charges $-(1-q_p)g, (1-q_p)g$ tends to move away from each other. Thus, the isolation of charge is realized, distinct from the cases involving the integer probe charges. In a sense, true deconfinement is taking place. We refer to such state as *inverse confining* in the following.
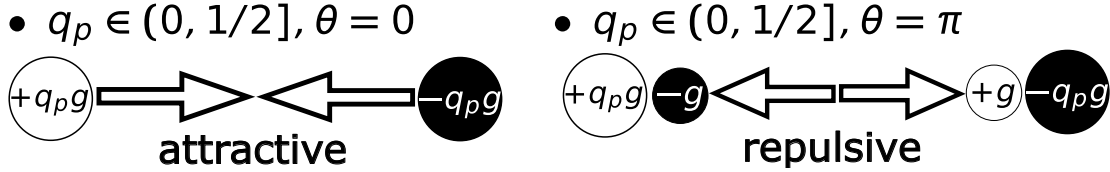

Figure 4.4: Appearance of attractive and repulsive forces between the static probe charges at $\theta = 0$ and $\theta = \pi$, when the probe charge is small $q_p \in (0, 1/2]$.

The above discussion is restricted to almost zero temperature. We finally investigate the string tension at finite temperature and θ. To cover almost the entire (T, θ) plane, we generate $N_{\text{conf}} = 10^6$ Monte Carlo configurations at $L_\tau = 4, 6, 8, 10, 12, 16, 20, 24, 28, 40, 56$, with θ/π ranging from 0.0 to 1.0 with a step width of $\delta\theta/\pi = 0.1$. By combining these configurations with the reweighing method, we achieve a very smooth surface in the (T, θ) plane. For both T and θ directions, we obtain ten data points between adjacent simulation points, each reweighted from the nearest simulation point. This results in 12^2 data points within the unit cell formed by four simulation points.

Figure 4.5 shows the string tension at $q_p = 0.5$ in the (T, θ) plane at $m/g = 0.25$ (upper half) and $m/g = 0.5$ (lower half). At $q_p = 0.5$, one can easily show that

$$\sigma(0.5, \theta + \pi) = -\sigma(0.5, \theta). \tag{4.11}$$

For both $m/g = 0.25$ and $m/g = 0.5$, the string tension is positive around $\theta \simeq 0$ at low temperatures, indicating confinement. The string tension diminishes as θ increases and becomes zero at $\theta = \pi/2$. With further increases in θ, the string tension becomes negative and reaches its minimum at $\theta = \pi$, indicating inverse confinement. The peak height is roughly proportional to the fermion mass m/g. As temperature increases, the string tension gradually converges to zero at all θ, indicating deconfinement. In Fig. 4.6, we show similar plots but at $q_p = 0.3$, where simple constraint like Eq. (4.11) does not exist. Consequently, we observe shifts in the peak positions. Nevertheless, the basic pattern remains the same: the system undergoes a smooth transition from the confining phase to the inverse confining phase as θ goes from 0 to π, and this transition becomes weakened as temperature increases. For sufficiently high temperatures, the θ dependence almost vanishes, and the system is always in the deconfining phase. Thus, we observe the thermal suppression of the quantum effects of the θ term.
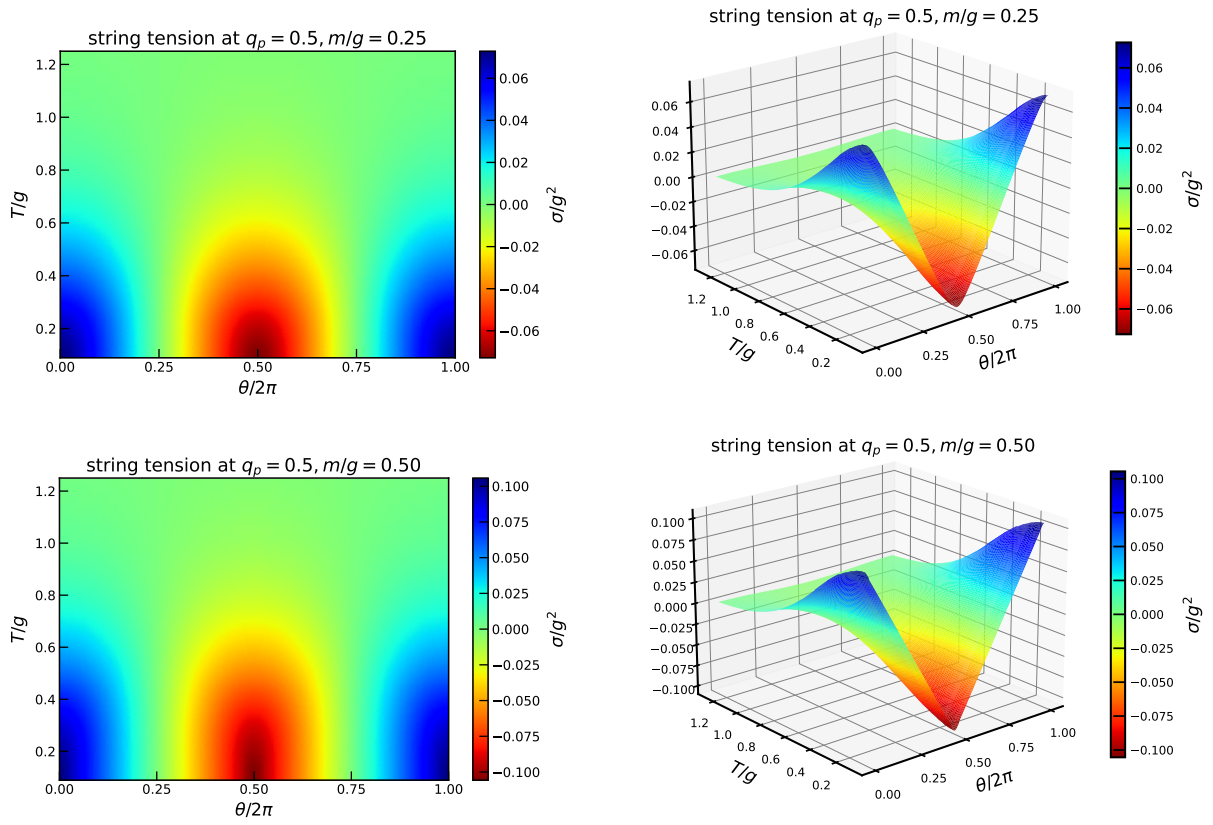
Figure 4.5: The string tension at $q_p = 0.5$ in the (T, θ) plane at $m/g = 0.25$ (upper half) and $m/g = 0.5$ (lower half). These figures are taken from Ref. [2].
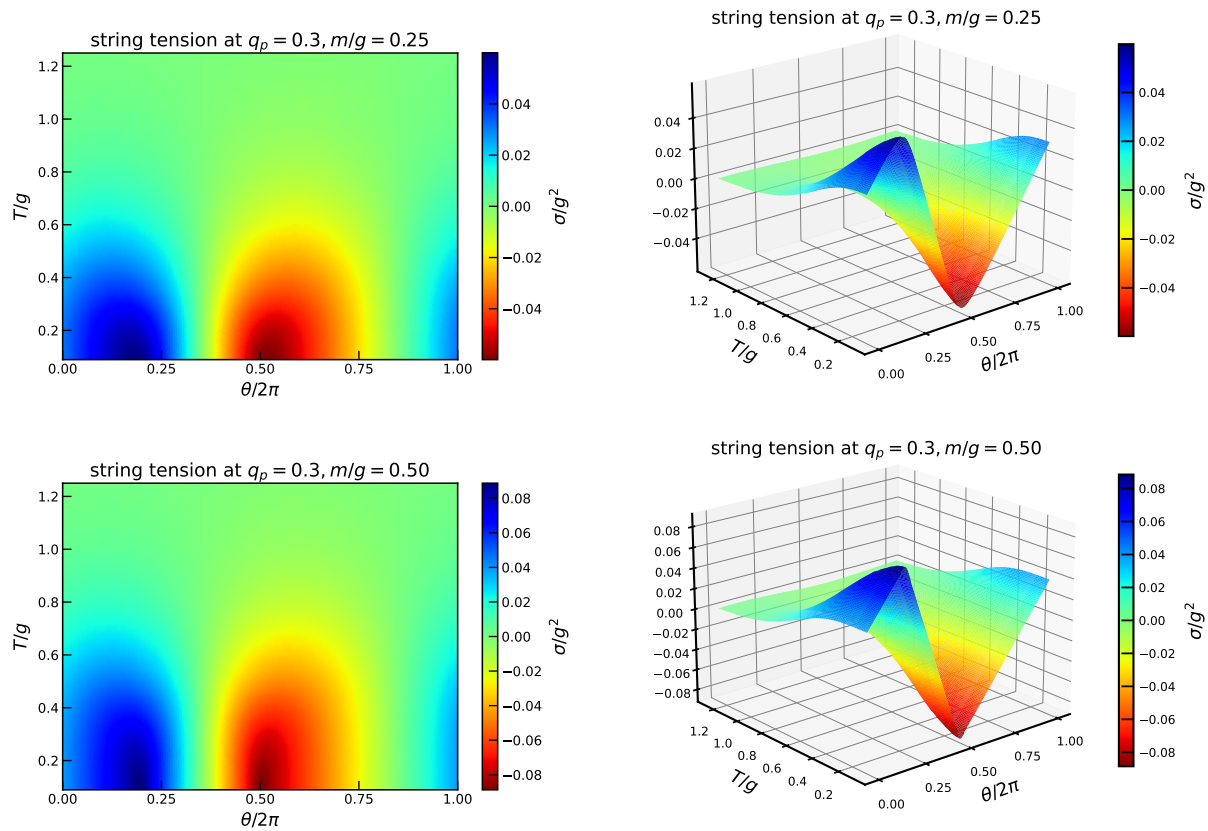
Figure 4.6: The string tension at $q_p = 0.3$ in the (T, θ) plane at $m/g = 0.25$ (upper half) and $m/g = 0.5$ (lower half). These figures are taken from Ref. [2].

Chapter 5

Phase diagram near the quantum critical point at $\theta = \pi$

In this chapter, we investigate the phase structure of the Schwinger model at $\theta = \pi$ in the temperature and fermion mass plane. As already noted in Section 3.3 and suggested from Figs. 3.3 and 3.4, at zero temperature, the CP symmetry at $\theta = \pi$ is spontaneously broken for sufficiently large fermion mass $m/g \gtrsim 0.33$ [66, 20, 24, 69, 40]. Our primary question in this chapter is how the CP symmetry is restored by thermal fluctuations and what kind of phase structure is realized at finite temperatures.

To be self-contained, we review the spontaneous CP symmetry breaking at zero temperature from both analytical and numerical sides in Section 5.1. In Section 5.2, we first recall the quantum Ising chain and conjecture the phase diagram of the Schwinger model at $\theta = \pi$ based on universality with the quantum Ising chain. Our strategy to establish the conjectured phase diagram using the Monte Carlo method is also explained. In Section 5.3, we perform a detailed numerical investigation of the correlation function and establish the conjectured phase diagram.

5.1 Spontaneous CP symmetry breaking at zero temperature

We review the spontaneous CP symmetry breaking at zero temperature in the Schwinger model at $\theta = \pi$. The spontaneous CP symmetry breaking at $\theta = \pi$ was first predicted by Coleman with an intuitive analytical picture using the bosonized form of the Schwinger model [12]. From the Euclidean action of the bosonized Schwinger model (2.48), the effective potential of ϕ, which is proportional to the electric field (2.49), is given by

$$V(\phi) = \frac{g^2}{2\pi}\phi^2 - \frac{e^\gamma}{2\pi^{3/2}}mg\cos\left(2\sqrt{\pi}\phi - \theta\right). \tag{5.1}$$

At $\theta = 0$, the cosine term forms a pocket at $\phi = 0$, indicating a unique CP-symmetric vacuum at any fermion mass. This changes drastically at $\theta = \pi$. Figure 5.1 shows the effective
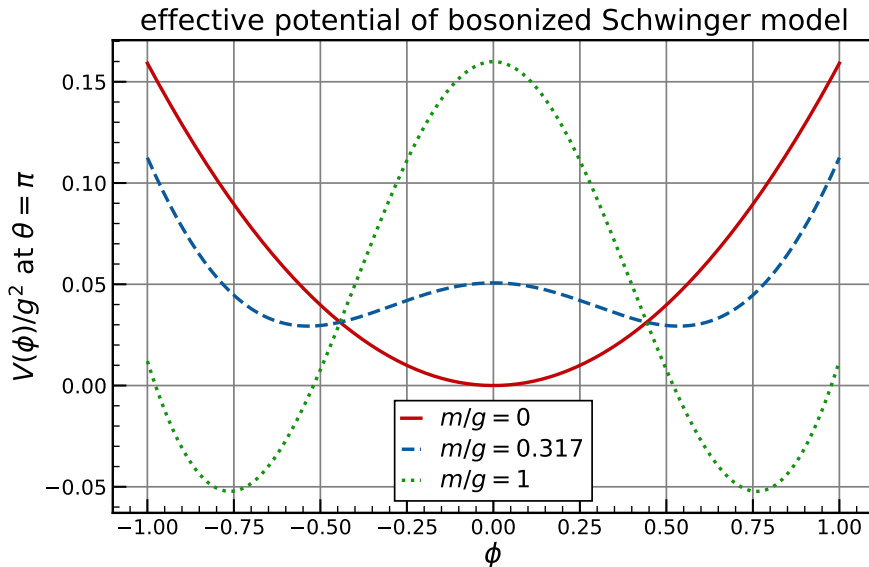
Figure 5.1: The effective potential of the bosonized Schwinger model (5.1) at $\theta = \pi$. This figure is taken from Ref. [2].

potential at $\theta = \pi$ at various fermion masses. For small fermion masses, the bosonic mass term dominates the potential, and we expect a unique vacuum. On the other hand, for large fermion masses, the cosine term forms a potential wall at $\phi = 0$, and we expect degenerate vacua, corresponding to the spontaneous CP symmetry breaking. In an intermediate fermion mass region, where the CP symmetry is either maintained or at least well-preserved, by expanding the cosine to the second order, the effective potential becomes [20]

$$V(\phi) \simeq \frac{1}{2} \left\{ \frac{g}{\sqrt{\pi}} \left(1 - \sqrt{\pi} e^{\gamma} \frac{m}{g} \right) \right\}^2 \phi^2. \tag{5.2}$$

As m/g increases, the effective mass decreases and reaches zero at

$$\frac{m_c}{g} = \frac{1}{\sqrt{\pi} e^{\gamma}} \simeq 0.317, \tag{5.3}$$

where we expect a second-order phase transition. It is important to note that this second-order phase transition is driven purely by quantum fluctuations. Hence, the critical point at zero temperature $(m_c, T = 0)$ is referred to as the quantum critical point (QCP) in the following.

First-principle numerical simulations are needed for a more quantitative and conclusive understanding. As described in Section 2.1, the conventional Monte Carlo method is not applicable due to the severe sign problem at $\theta = \pi$, when using the Euclidean lattice fermion formulations. Consequently, numerical investigations of the QCP have been mainly performed using the spin Hamiltonian (2.38).

The first numerical evidence of the above analytical picture was provided by Hamer et al. [66], in which the spin Hamiltonian was combined with the finite-size scaling method [71]

to identify the QCP. They estimated the critical mass to be $m_c/g = 0.325(20)$ and a critical exponent $\nu = 0.9(1)$. A more precise investigation was done by Byrnes et al. [20] using the density matrix renormalization group [72, 73]. They obtained at present the most precise estimate of the critical mass

$$\frac{m_c}{g} = 0.3335(2), \tag{5.4}$$

and two critical exponents

$$\nu = 1.01(1), \quad \frac{\beta}{\nu} = 0.125(5). \tag{5.5}$$

These two critical exponents precisely agree with those of the quantum Ising chain ($\nu = 1, \beta = 1/8$), indicating that these two models are in the same universality class. As a quite different approach, Shimizu and Kuramashi [24] applied the Grassmann tensor renormalization group [63] to the conventional Wilson fermion formulation in Euclidean space-time, explained in Section 2.1. Using the Lee–Yang and Fisher zero analyses, they provided further evidence that the QCP belongs to the Ising universality class. Other approaches include, for example, a conversion method from the imaginary θ term [69], and one using quantum computing [40]. The resulting phase diagram of the Schwinger model at zero temperature in the θ angle and fermion mass plane is shown in Fig. 5.2.
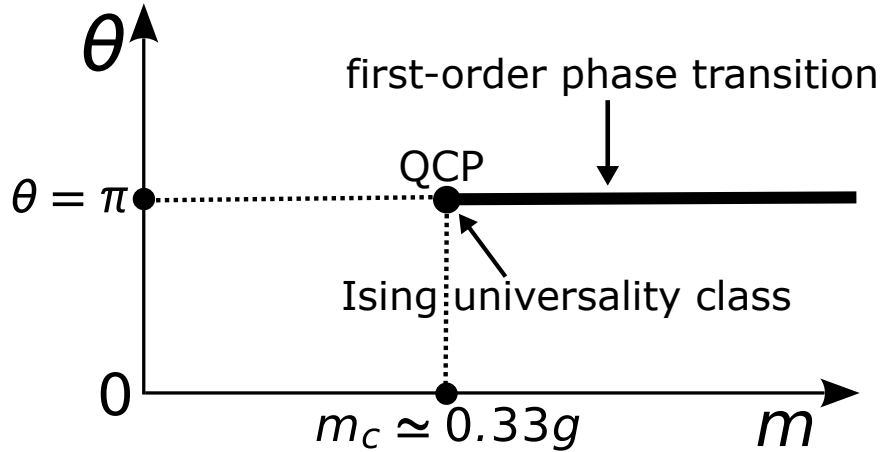

Figure 5.2: Phase diagram of the Schwinger model at zero temperature in the θ angle and fermion mass plane.

5.2 Method to explore phase diagram near the quantum critical point

Compared to the comprehensive studies on the second-order phase transition at zero temperature, the phase structure near the QCP at finite temperature remains much less known.

In general, thermal fluctuations work to spoil the long-range order. Therefore, it is natural to consider that the CP symmetry is restored at high temperatures. Figure 5.3 shows the electric field at $m/g = 0.5$ in the (T, θ) plane, which is obtained in the same way as the string tension in Section 4.3. It is clear that the discontinuity at $\theta = \pi$ disappears at high temperatures. However, it is not clear from Fig. 5.3 at which temperature the CP symmetry is restored.
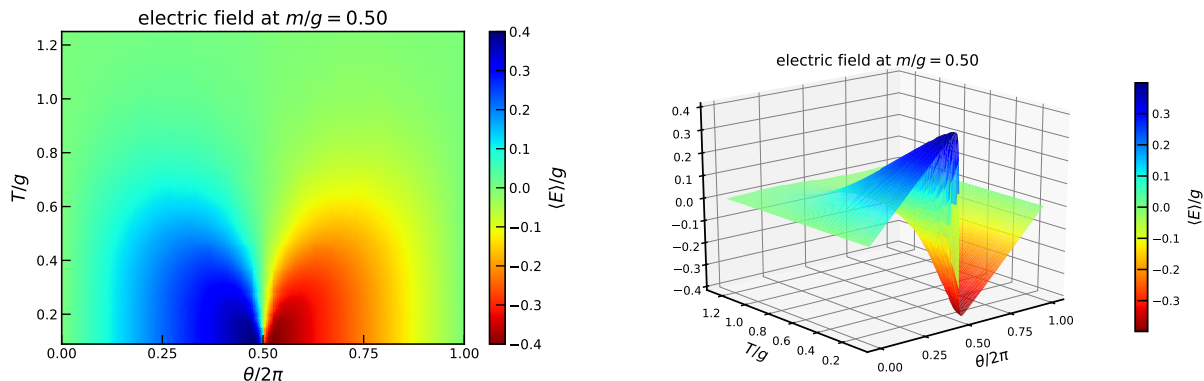

Figure 5.3: The electric field in the (T, θ) plane at $m/g = 0.5$.

To the best of the author's knowledge, the only study addressing this issue was conducted by Buyens et al. [29], in which they investigated the fate of the spontaneously broken CP symmetry at finite temperature using the matrix product operators [74, 75] based on the spin Hamiltonian formulation. For each $\theta \simeq \pi$, they obtained the temperature $T_{1/2}(\theta)$ at which the electric field equals half of its vacuum expectation value. By empirically extrapolating $T_{1/2}(\theta)$ toward $\theta \to \pi$, they concluded that $T_{1/2}$ diverges, implying that the CP symmetry is restored at any nonzero temperature. The weakness of their argument lies in relying on extrapolation based on empirical rules. Incorporating some analytical theory is necessary to perform a more reliable extrapolation. [1]

In this work, we explore broad characteristics near the QCP at finite temperature by the Monte Carlo method incorporating the perspective of universality with the quantum Ising chain. In this section, we first review the quantum Ising chain, in particular its phase structure at finite temperature, and then explain our strategy to explore the phase diagram of the Schwinger model at $\theta = \pi$.

5.2.1 Quantum Ising chain

We here review the phase diagram of the quantum Ising chain following a review [76, Chapter 10]. The quantum Ising chain is the quantum analog of the two-dimensional classical Ising model with no external magnetic field. The Hamiltonian of the quantum Ising chain is given

---

[1]In the Monte Carlo simulation of QCD, the numerical cost diverges as the quark mass approaches zero. When studying the chiral properties of QCD, the chiral perturbation theory is conventionally used for extrapolating numerical data at finite quark mass to the chiral limit.

by
$$H_I = -J \sum_{i_x} (Z_x Z_{x+1} + g X_x), \tag{5.6}$$

where $J > 0$ is an overall energy scale, $g > 0$ is the dimensionless coupling constant, and Z_x, X_x are the Pauli matrices

$$Z = \sigma^3 = \begin{pmatrix} 1 & 0 \\ 0 & -1 \end{pmatrix}, \quad X = \sigma^1 = \begin{pmatrix} 0 & 1 \\ 1 & 0 \end{pmatrix}, \tag{5.7}$$

which reside on a spatial site x, respectively. Thus, the first term is diagonal, whereas the second term is not. The Hamiltonian is symmetric under the $\mathbb{Z}_2$ transformation, generated by the unitary operator $\prod_x X_x$.

Unlike the massive Schwinger model, the quantum Ising chain is exactly solvable in the sense that all eigenstates are obtained analytically by applying the Jordan–Wigner transformation and diagonalizing the Hamiltonian by the Bogoliubov transformation [77, 78]. At zero temperature, as decreasing the coupling constant, the system undergoes a second-order phase transition to the ferromagnetic ($\mathbb{Z}_2$ broken) phase at $g_c = 1$, which is analogous to the Schwinger model at $\theta = \pi$.

The phase diagram of the quantum Ising chain in the temperature and coupling constant plane can be deduced from the correlation function of the order parameter at finite temperature [2]

$$C(x) = \langle Z_0 Z_x \rangle = \mathrm{tr}\big(Z_0 Z_x e^{-H_I/T}\big) \big/ \mathrm{tr}\big(e^{-H_I/T}\big) . \tag{5.8}$$

A crucial feature that we will exploit throughout this chapter is the explicit asymptotic form of the correlation function, derived by Sachdev [79]:

$$\lim_{x \to \infty} C(x) = Z T^{1/4} G_I(\Delta/T) \exp\left(-\frac{Tx}{c} F_I(\Delta/T)\right), \quad \Delta = r(g_c - g), \tag{5.9}$$

where Z, c, r are the nonuniversal constants, and F_I and G_I are the universal scaling functions of the quantum Ising chain. Their explicit forms read [79]

$$F_I(s) = |s|\Theta(-s) + \frac{1}{\pi} \int_0^\infty dy \, \ln \coth \frac{(y^2 + s^2)^{1/2}}{2}, \tag{5.10}$$

$$\ln G_I(s) = \int_s^1 \frac{dy}{y} \left[\left(\frac{dF_I(y)}{dy}\right)^2 - \frac{1}{4}\right] + \int_1^\infty \frac{dy}{y} \left(\frac{dF_I(y)}{dy}\right)^2, \tag{5.11}$$

where $\Theta(x)$ is the step function. Figure 5.4 plots the universal scaling functions F_I, G_I, illustrating their smoothness throughout the entire region.

The correlation length is defined from the exponential decay of the correlation function (5.9) as

$$\xi^{-1} = \frac{T}{c} F_I\left(\frac{\Delta}{T}\right). \tag{5.12}$$

---

[2]Note that we do not subtract the connected part $\langle Z_x \rangle^2$ from the correlation function.
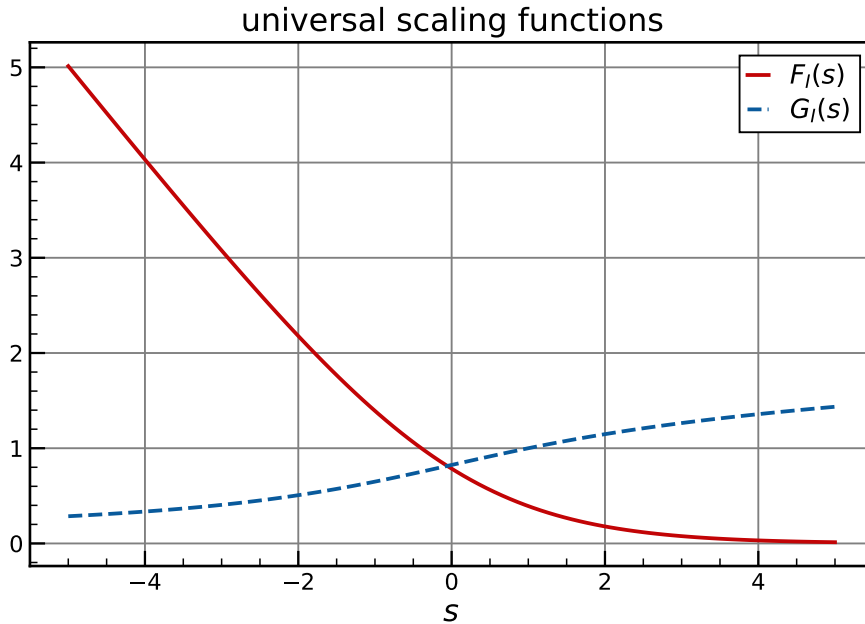
Figure 5.4: The universal scaling functions of the quantum Ising chain (5.10, 5.11). This figure is taken from Ref. [2].

At any nonzero temperature, the correlation length is finite, indicating that the correlation function vanishes in the long-distance limit. Simultaneously, the correlation function converges to its connected part as

$$\lim_{x \to \infty} C(x) = \langle Z_x \rangle^2 . \tag{5.13}$$

Thus, we can deduce that the system is in the paramagnetic ($\mathbb{Z}_2$ symmetric) phase at any nonzero temperature.

In the vicinity of the QCP, even a slight shift in the coupling constant results in a substantial change in Δ/T. It is meaningful to categorize the phase into three depending on the value of Δ/T, each characterized by a specific asymptotic form of the correlation length [79]:

$$\xi = \begin{cases} c\sqrt{\frac{\pi}{2\Delta T}}e^{\Delta/T}, & \Delta/T \gg 1, \\ \frac{4c}{\pi T}, & |\Delta|/T \ll 1, \\ \frac{c}{|\Delta|}, & \Delta/T \ll -1. \end{cases} \tag{5.14}$$

In the low-temperature region with $\Delta > 0$, the correlation length diverges exponentially toward the zero temperature limit, corresponding to the ferromagnetic phase at zero temperature. Conversely, the long-range order at zero temperature is thermally destroyed. This region is commonly referred to as the thermally disordered region in the context of condensed matter physics [80]. In the other low-temperature region with $\Delta < 0$, the correlation length saturates at a finite value in the zero temperature limit, resulting in a disordered phase even

at zero temperature. This region is called the quantum disordered phase [80]. The final region with $|\Delta|/T \ll 1$ is the so-called quantum critical region, where the physics is considered to be governed by the thermal excitations of the quantum critical ground state [80]. The resulting phase diagram of the quantum Ising chain is shown in the left panel of Fig. 5.5. Universality with the quantum Ising chain implies the phase diagram of the Schwinger model at $\theta = \pi$ near the QCP, as shown in the right panel of Fig. 5.5.
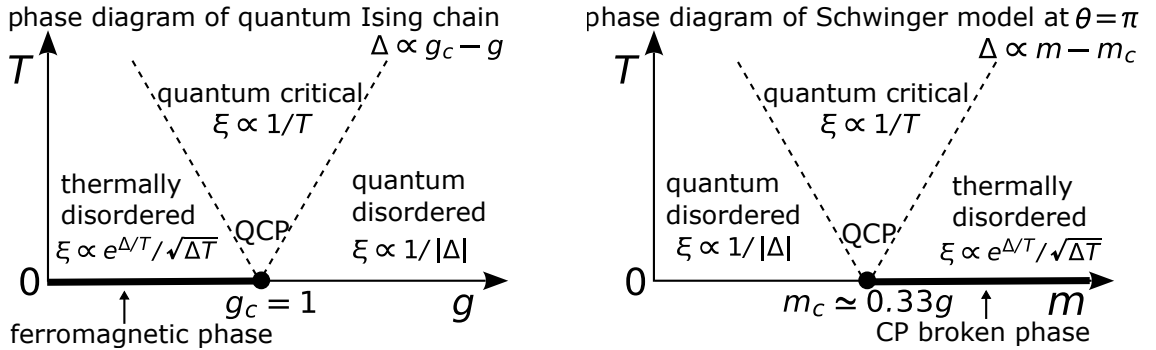

Figure 5.5: (Left) Phase diagram of the quantum Ising chain. (Right) Conjectured phase diagram of the Schwinger model at $\theta = \pi$. These figures are taken from Ref. [2].

5.2.2 Schwinger model at $\theta = \pi$

We here explain our strategy to establish the conjectured phase diagram of the Schwinger model at $\theta = \pi$. In the previous subsection, we observed that the phase diagram of the quantum Ising chain at finite temperature can be deduced from the asymptotic form of the correlation function (5.9). Therefore, our approach is rather straightforward: we calculate the correlation function of the electric field at $\theta = \pi$ at finite temperatures near the QCP and examine whether the correlation function shares the same asymptotic form as the quantum Ising chain (5.9). If this confirmation is obtained at a certain temperature, the scaling behavior should also hold at lower temperatures, allowing us to determine the phase diagram of the Schwinger model near the QCP. Our method does not aim to approach the QCP itself, but rather inspect the scaling behavior near the QCP. We need not employ the finite-size scaling method because the correlation length is always finite in our analysis. The most significant difficulty is that we must circumvent the sign problem at $\theta = \pi$ in some way.

Using the lattice bosonized Schwinger model, the difficulty can be completely avoided. The correlation function of the electric field at temperature $T/g = (L_\tau a g)^{-1}$ can be expressed by the path-integral, along with using the proportional relation between the electric field and

the scalar field (2.49):

$$C(x) = \frac{1}{g^2} \langle E_x E_0 \rangle' \tag{5.15a}$$

$$= \frac{1}{\pi} \langle \phi_x \phi_0 \rangle' \tag{5.15b}$$

$$= \frac{1}{\pi} \int D\phi\, \phi_{x,0}\phi_{0,0} e^{-S_E} \bigg/ \int D\phi\, e^{-S_E}, \tag{5.15c}$$

where $\langle \cdot \rangle'$ denotes the expectation value under the shifted Euclidean action (2.48).

5.3 Numerical results

In this work, we use a sufficiently fine and large lattice of $ag = 0.2$, $L_x = 1792$; we verify that the finite lattice spacing and finite spatial length effects are indeed nearly negligible in our analysis. As for the temperature, we mainly consider two low temperatures $L_\tau = 112, 56$ to inspect the scaling behavior near the QCP.

5.3.1 Autocorrelation and lattice artifacts

In this subsection, we investigate the autocorrelation and lattice artifacts in preparation for the large-scale numerical simulations in the next subsection.

We first investigate the autocorrelation among Monte Carlo configurations near the QCP for reliable error estimates. The autocorrelation can be characterized by the autocorrelation function [81]

$$A(t) = \frac{1}{N - t} \sum_{i=1}^{N-t} \phi_i \phi_{i+t} - \langle \phi \rangle^2, \tag{5.16}$$

where ϕ_i is the mean of $\phi_{x,\tau}$:

$$\phi_i = \frac{1}{L_x L_\tau} \sum_{x,\tau} \phi_{x,\tau} \tag{5.17}$$

at the i-th Monte Carlo configuration, and $\langle \phi \rangle$ is the subtraction term, which should be 0 in our analysis. From the normalized autocorrelation function

$$C(t) = \frac{A(t)}{A(0)}, \tag{5.18}$$

the integrated autocorrelation time with finite lattice data is defined as

$$\tau_{\text{int}}(t) = \frac{1}{2} + \sum_{i=1}^{t} C(i). \tag{5.19}$$

Twice the integrated autocorrelation time

$$\tau_{\text{int}} = \lim_{t \to \infty} \tau_{\text{int}}(t) \tag{5.20}$$

gives an estimate of the number of iterations required to generate mostly independent config-
urations. Figure 5.6 shows the integrated autocorrelation time (5.19) at $m/g = 0.2, 0.33, 0.4$.
From such behaviors, we estimate the integrated autocorrelation time (5.20). The estimated
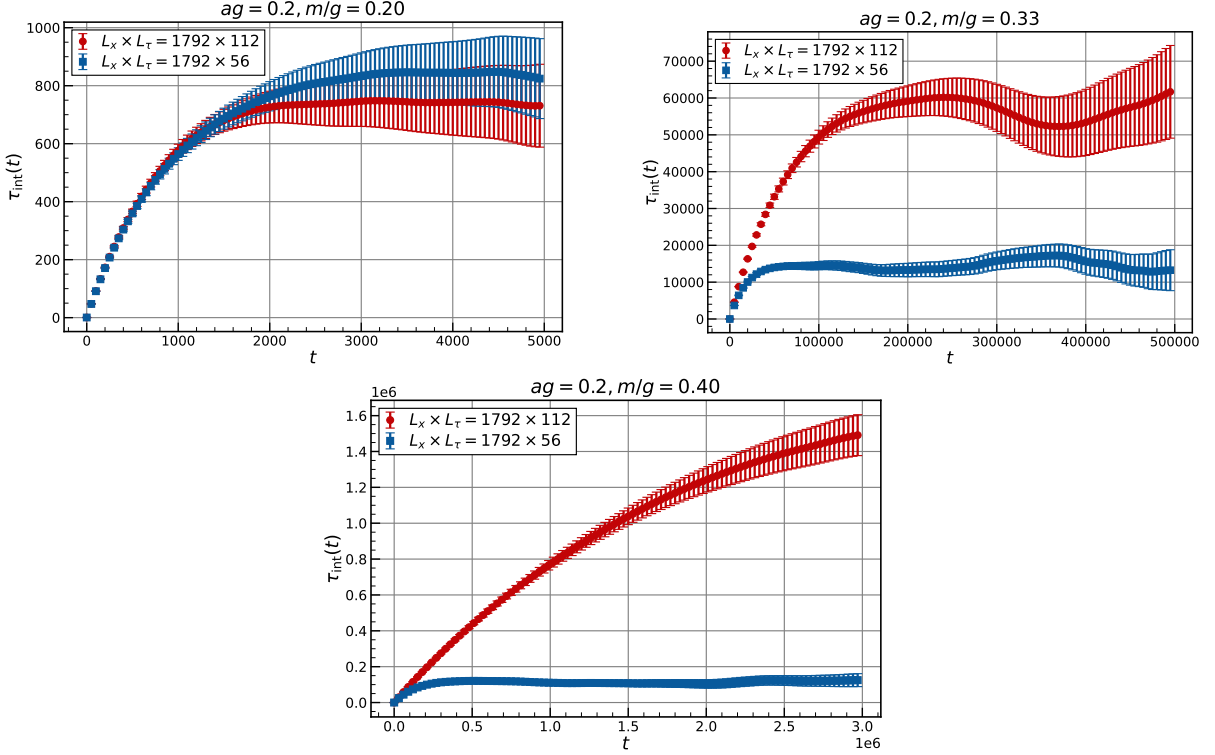

Figure 5.6: The integrated autocorrelation time with finite lattice data (5.19) at $m/g = 0.2, 0.33, 0.4$. These figures are taken from Ref. [2].

integrated autocorrelation times at the two lattices and various fermion masses are summa-
rized in Table 5.1. We find that the integrated autocorrelation time is longer at larger fermion
masses and lower temperatures, which seems to be related to the expected correlation length
near the QCP, as shown in the right panel of Fig. 5.5. In this work, we set the number
of iterations to approximately $\tau_{\text{int}}/2$ and use the binning of ten to eliminate the remaining
autocorrelation.

We also investigate the finite lattice spacing and finite spatial length effects. For this
purpose, we compare correlation functions at $m/g = 0.32$ calculated using three different
lattices:

- $ag = 0.2, L_x \times L_\tau = 1792 \times 112$,

- $ag = 0.2, L_x \times L_\tau = 896 \times 112$,

- $ag = 0.1, L_x \times L_\tau = 3584 \times 224$.

Table 5.1: Estimated integrated autocorrelation times at the two lattices and various fermion masses.

ag	$L_x \times L_\tau$	m/g	τ_{int}
0.2	1792×112	0.2	$\sim 8 \times 10^2$
0.2	1792×112	0.33	$\sim 6 \times 10^4$
0.2	1792×112	0.4	$\sim 2 \times 10^6$
0.2	1792×56	0.1	$\sim 2 \times 10^2$
0.2	1792×56	0.2	$\sim 8 \times 10^2$
0.2	1792×56	0.33	$\sim 1.4 \times 10^4$
0.2	1792×56	0.4	$\sim 1.2 \times 10^5$
0.2	1792×56	0.5	$\sim 5 \times 10^5$

By comparing the first and the second lattices, we can assess the finite spatial length effect. The finite lattice spacing effect can be examined by comparing the first and the third lattices. Figure 5.7 shows the correlation functions at these three lattices. For each correlation
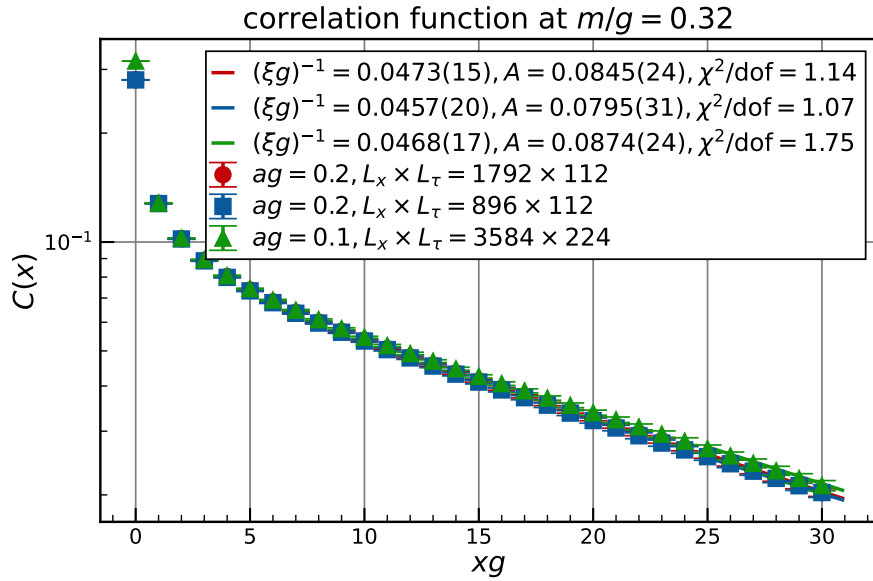

Figure 5.7: Correlation functions and fit results using the single exponential function (5.21) at three lattices of $ag = 0.2, L_x \times L_\tau = 1792 \times 112$, $ag = 0.2, L_x \times L_\tau = 896 \times 112$, and $ag = 0.1, L_x \times L_\tau = 3584 \times 224$. For visibility, only one-fifth and one-tenth of the data points are plotted for $ag = 0.2$ and $ag = 0.1$, respectively. This figure is taken from Ref. [2].

function, we perform a correlated fit using the single exponential function

$$C(x) = A \exp\left(-\frac{x}{\xi}\right), \tag{5.21}$$

with the correlation length ξ and the amplitude A being the fit parameters. The fit range is set as $xg \in [25, 30]$. The fit results are also shown in Fig. 5.7. We find that the resulting

correlation lengths and amplitudes are consistent with each other, suggesting that both finite lattice spacing and finite spatial length effects are nearly negligible in our analysis.

5.3.2 Correlation function near the quantum critical point

We now perform a detailed investigation of the correlation function near the QCP. To carefully examine the behavior near the QCP, we analyze correlation functions over a broad range of fermion masses. The simulation parameters relevant in this subsection are summarized in Table 5.2.

Table 5.2: Summary of the simulation parameters.

ag	$L_x \times L_\tau$	m/g	iterations, n	configurations, n
0.2	1792×112	0.16, 0.18, 0.2, 0.22, 0.24, 0.26	4×10^2	10^5
0.2	1792×112	0.28, 0.3, 0.32, 0.34, 0.36, 0.38	3×10^4	2×10^3
0.2	1792×112	0.4, 0.42, 0.44	10^6	10^3
0.2	1792×56	0.08, 0.10, 0.12, 0.14	10^2	10^5
0.2	1792×56	0.16, 0.18, 0.2, 0.22, 0.24, 0.26	4×10^2	10^5
0.2	1792×56	0.28, 0.3, 0.32, 0.34, 0.36, 0.38	7×10^3	10^4
0.2	1792×56	0.4, 0.42, 0.44	6×10^4	10^3
0.2	1792×56	0.48, 0.5, 0.52	1.3×10^5	10^3

For each correlation function, we perform a correlated fit using the single exponential function (5.21) and extract the correlation length ξ and amplitude A. For demonstration, we show the correlation functions and the fit results at $m/g = 0.2, 0.26, 0.34, 0.44$ at the lower temperature in Fig. 5.8. The fit ranges are set as $xg \in [20, 25], [20, 25], [25, 30], [30, 35]$, for $m/g = 0.2, 0.26, 0.34, 0.44$, respectively.

We next perform fits to the correlation length and amplitude at the lower temperature, independently. Universality with the quantum Ising chain suggests the asymptotic form of the correlation function in the Schwinger model at $\theta = \pi$ as

$$\lim_{x \to \infty} C(x) = Z(T/g)^{1/4} G_I(\Delta/T) \exp\left(-\frac{Tx}{c} F_I(\Delta/T)\right), \quad \Delta = r(m - m_c), \qquad (5.22)$$

where Z, c, r are the nonuniversal constants and the functional forms of F_I and G_I are given in Eqs. (5.10, 5.11). Figure 5.9 shows the correlation length and amplitude as functions of the fermion mass, fitted using

$$\frac{T}{cg} F_I(r(m - m_c)/T), \quad Z(T/g)^{1/4} G_I(r(m - m_c)/T), \qquad (5.23)$$

respectively. In these fits, we set the critical mass to $m_c/g = 0.3335$, using the wisdom obtained by Byrnes et al. (5.4). From the fits, the nonuniversal constants are found to be

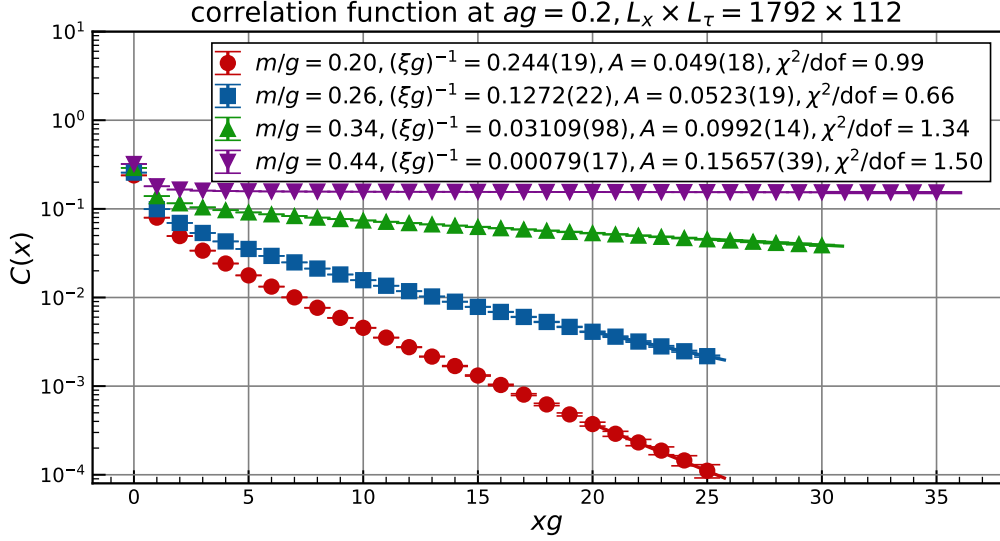$$Z = 0.2435(16), \quad c = 0.978(11), \quad r = 1.593(46). \qquad (5.24)$$

61

Figure 5.8: Correlation functions and fit results by the single exponential function (5.21) at $m/g = 0.2, 0.26, 0.34, 0.44$. The lattice is $ag = 0.2$, $L_x \times L_\tau = 1792 \times 112$. For visibility, only one-fifth of the data points are plotted. This figure is taken from Ref. [2].

Note that the value of r is also obtained from the fit to the correlation length, as shown in the left panel of Fig. 5.9. In the following analysis, however, we use the value obtained from the amplitude since the fit seems to be more reliable, although they are consistent with each other.
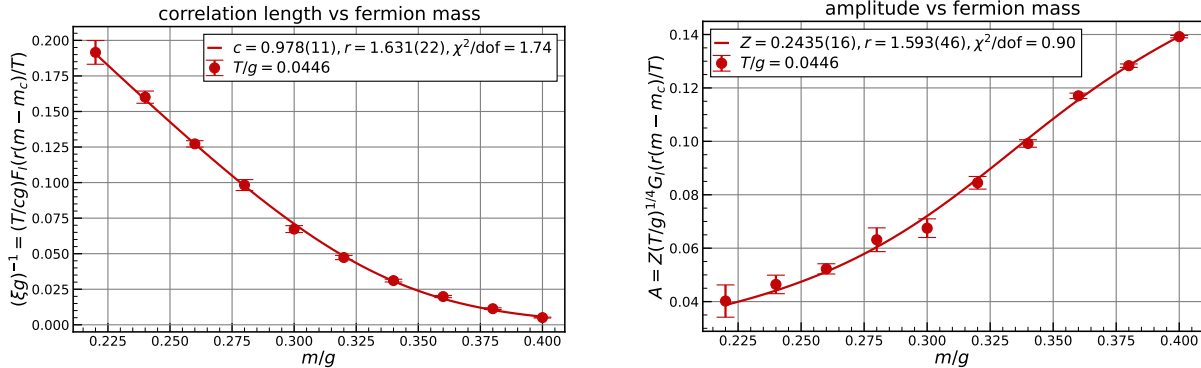
Figure 5.9: Fits to the correlation length (left) and to the amplitude (right) using the universal scaling functions of the quantum Ising chain (5.10, 5.11). The lattice is $ag = 0.2, L_x \times L_\tau = 1792 \times 112$. These figures are taken from Ref. [2].

We rescale the correlation lengths and amplitudes at the two temperatures using the nonuniversal constants (5.24) and compare them to the universal scaling functions of the quantum Ising chain (5.10, 5.11). Figure 5.10 demonstrates that the rescaled data align beautifully with the expected analytical curves. In particular, we observe that data at the

62

higher temperature also match the analytical curves, providing strong evidence that the correlation function of the Schwinger model at $\theta = \pi$ shares the same asymptotic form as the quantum Ising chain. Based on the argument in Section 5.2, we conclude that the phase diagram of the Schwinger model at $\theta = \pi$ is entirely analogous to the quantum Ising chain near the QCP, as schematically shown in Fig. 5.5.
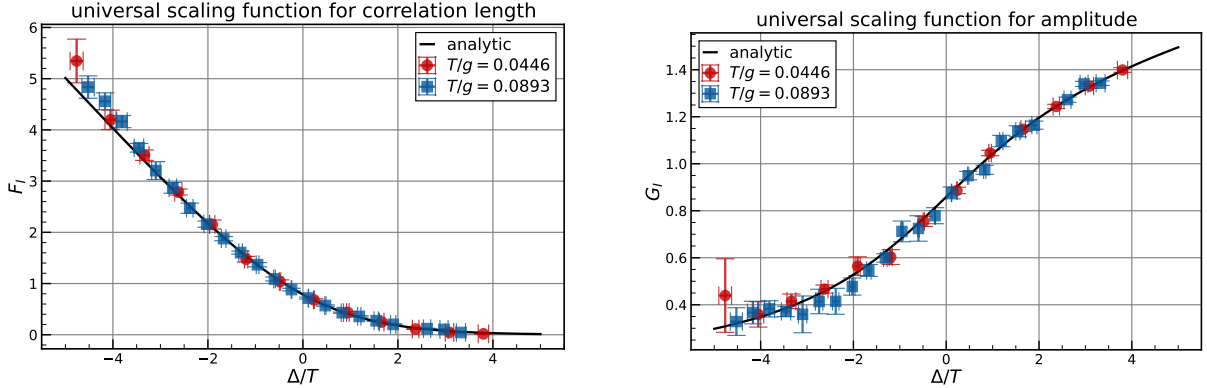

Figure 5.10: Rescaled correlation length (left) and amplitude (right) using the nonuniversal constants (5.24), compared with the universal scaling functions of the quantum Ising chain (5.10, 5.11). These figures are taken from Ref. [2].

5.3.3 Range of the scaling behavior

With the established asymptotic form of the correlation function (5.22) and the explicit values of the nonuniversal constants (5.24), we can quantitatively predict the behavior of certain observables near the QCP. In this subsection, we estimate the range of the scaling behavior by comparing the predictions to direct numerical results.

We first examine how well the scaling behavior holds at zero temperature by comparing our prediction to Byrnes et al.'s results [20]. [3]

At zero temperature in the CP symmetric phase ($m \leq m_c$), the inverse of the correlation length, i.e., the energy gap, is given by

$$(\xi g)^{-1} = \frac{1}{c} \frac{|\Delta|}{g} = \frac{r}{c} \left(\frac{m_c}{g} - \frac{m}{g} \right). \tag{5.25}$$

In Fig. 5.11, we compare Eq. (5.25) to their direct numerical results [20]. Figure 5.11 demonstrates a strong agreement between the prediction and their direct numerical results, indicating that the scaling behavior holds surprisingly well in the region $m \in [0, m_c]$ at zero temperature.

We can also predict the electric field in the CP broken phase ($m > m_c$) at zero temperature from the asymptotic form of the correlation function (5.22). In this region, using the zero

---

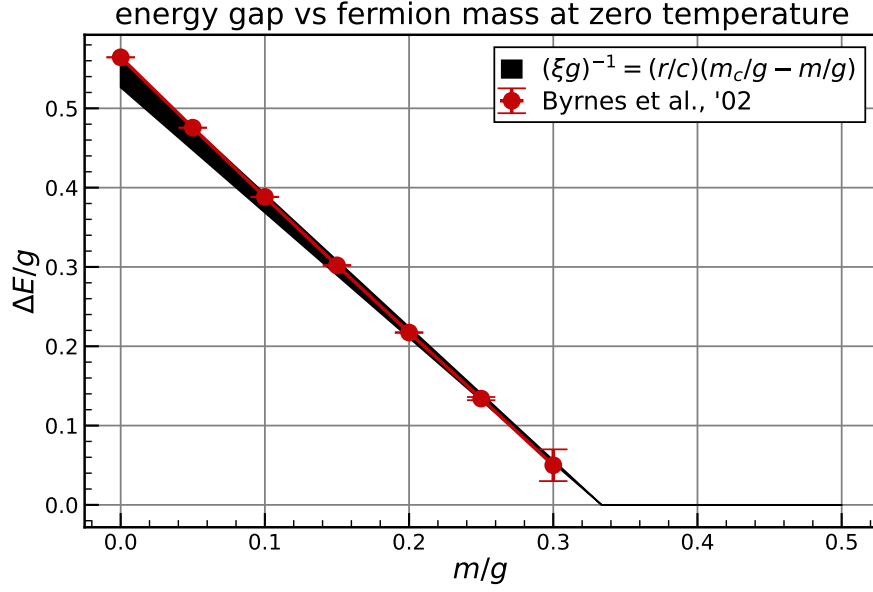[3]The explicit values can be found in Table 6.10 of Ref. [82].

Figure 5.11: Fermion mass dependence of the energy gap at zero temperature. This figure is taken from Ref. [2].

temperature limit of G_I [79]

$$G_I(\Delta/T) \to (\Delta/T)^{1/4}, \quad \Delta/T \gg 1, \tag{5.26}$$

the correlation function behaves as

$$C(x) \to Z(T/g)^{1/4}(\Delta/T)^{1/4} = Z(\Delta/g)^{1/4} = Zr^{1/4}\left(\frac{m}{g} - \frac{m_c}{g}\right)^{1/4}. \tag{5.27}$$

Therefore, the electric field in the CP broken phase is given by

$$\frac{|\langle E \rangle|}{g} = Z^{1/2}r^{1/8}\left(\frac{m}{g} - \frac{m_c}{g}\right)^{1/8}. \tag{5.28}$$

We plot Eq. (5.28) using the nonuniversal constants (5.24) in Fig. 5.12. We observe a rather sharp but continuous increase in the electric field near the QCP, which corresponds to the small critical exponent $\beta = 1/8$. In Fig. 5.12, the numerical results by Byrnes et al. [20] are also plotted. We find that the analytical curve successfully explains their numerical results near the QCP. While clear discrepancies are observed away from the QCP, the discrepancies are very small even at $m/g = 1$. This allows us to conclude that the scaling behavior holds well in the region $m/g \in [m_c/g, 1]$ at zero temperature.

The agreement with Byrnes et al.'s results near the QCP reinforces the validity of our estimate for the nonuniversal constants (5.24) and indicates that the scaling behavior holds well in the region $m/g \in [0, 1]$ at zero temperature.
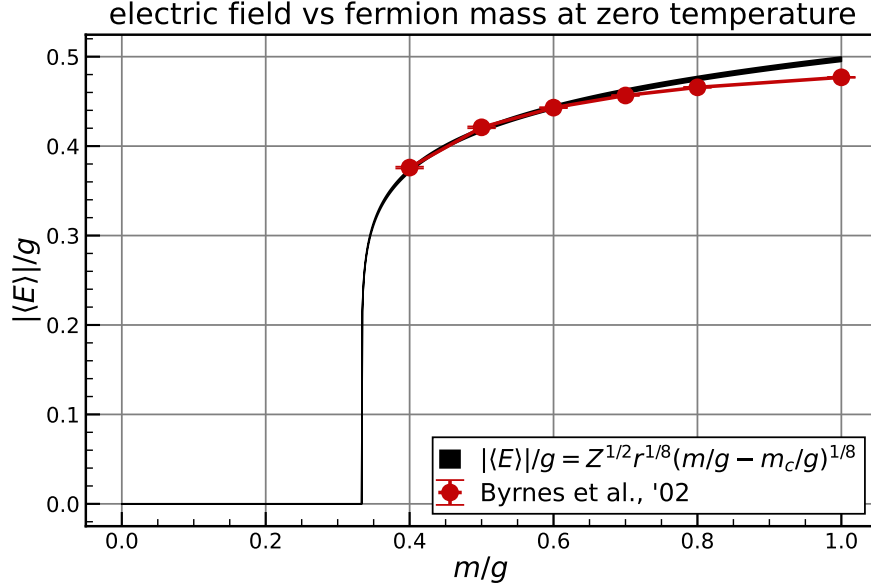
Figure 5.12: Fermion mass dependence of the electric field at zero temperature. This figure is taken from Ref. [2].

We also examine the range of the scaling behavior at the critical fermion mass. In this region, the inverse of the correlation length is

$$(\xi g)^{-1} = \frac{\pi T}{4cg},\tag{5.29}$$

and the amplitude is given by

$$A = 0.8587 Z \left(\frac{T}{g}\right)^{1/4},\tag{5.30}$$

from the behavior of G_I [79]:

$$G_I(\Delta/T) = 0.8587..., \quad |\Delta|/T \ll 1.\tag{5.31}$$

In Fig. 5.13, we compare Eqs. (5.29, 5.30) to our direct numerical results, which are obtained in the same way as in the previous subsection. The simulation parameters are summarized in Table. 5.3. We find that the direct numerical results agree with the analytical curves with an accuracy of at least ninety percent up to $T/g \simeq 0.4$. This ensures that the scaling behavior holds well in the region $T/g \in [0, 0.4]$ at the critical fermion mass.

In Fig. 5.14, we finally present the inverse of the correlation length in the temperature and fermion mass plane obtained from the asymptotic form (5.22) and the nonuniversal constants (5.24). Based on the analysis in this subsection, the values are reliable at zero temperature or at the critical fermion mass within the range plotted in Fig. 5.14. At $m = 0$, the Schwinger model is equivalent to the free boson theory (1.62), resulting in an energy gap of $g/\sqrt{\pi} \simeq 0.564g$ at any temperature. In Fig. 5.14, we indeed observe approximate temperature independence up to $T/g \simeq 0.3$, suggesting that Fig. 5.14 is to some extent reliable except for the two edges on the finite-temperature side.

Table 5.3: Simulation parameters and estimated autocorrelation times for investigating temperature dependence of the correlation length and the amplitude at the critical fermion mass.

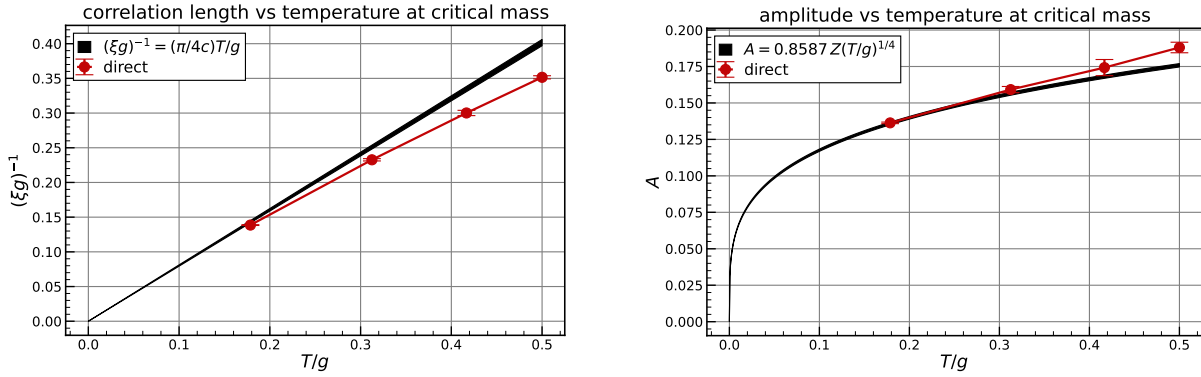| ag	$L_x \times L_\tau$	m/g	τ_{int}	iterations, n	configurations, n
0.2	1792×28	0.3335	$\sim 2 \times 10^3$	10^3	10^5
0.2	1792×16	0.3335	$\sim 10^3$	5×10^2	10^5
0.2	1792×12	0.3335	$\sim 5 \times 10^2$	2.5×10^2	10^5
0.2	1792×10	0.3335	$\sim 3 \times 10^2$	1.5×10^2	10^6

Figure 5.13: Temperature dependence of the correlation length (left) and the amplitude (right) at the critical fermion mass. These figures are taken from Ref. [2].
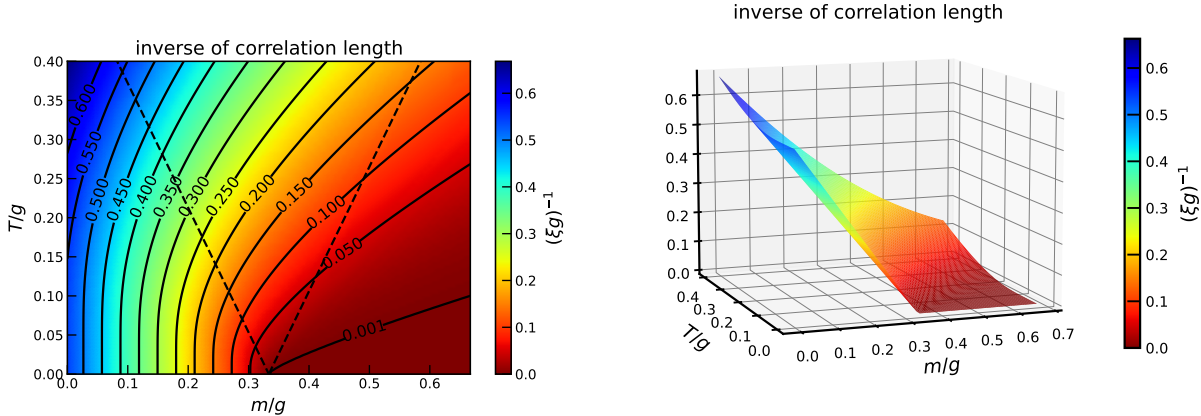

Figure 5.14: Inverse of the correlation length in the temperature and fermion mass plane obtained from the asymptotic form (5.22) and the nonuniversal constants (5.24). The dashed lines $T = \pm\Delta$, $\Delta = r(m - m_c)$ in the left panel are the crossover lines that classify the phases effectively. These figures are taken from Ref. [2].

Chapter 6

Summary and outlook

In this thesis, we have studied the interplay between the quantum effects of the θ term and thermal effects in the Schwinger model by the Monte Carlo method while avoiding the sign problem using the bosonization technique.

In Chapter 1, we first presented the theoretical background of the θ term mainly focusing on quantum chromodynamics and the purpose of this thesis. We next reviewed the basic properties of the Schwinger model in both the Lagrangian and Hamiltonian formalism. Bosonization, which played a fundamental role in this thesis, was also introduced in this chapter.

In Chapter 2, we introduced three different lattice formulations of the Schwinger model in detail. Special attention was given to the chiral anomaly as it is closely related to the fermion doubling problem through the Nielsen–Ninomiya theorem. We observed that bosonization provides a novel approach to formulate the Schwinger model on a lattice, effectively evading the fermion doubling problem and preserving the chiral anomaly intact simultaneously. By comparing the three formulations, we concluded that the Monte Carlo study of the lattice bosonized Schwinger model is the best method to investigate the model at finite temperature and θ region, both theoretically and practically.

In Chapter 3, before exploring new properties of the Schwinger model, we verified the lattice bosonized Schwinger model by reproducing the analytical and numerical results in the literature. We derived the analytical expression for the chiral condensate at the vanishing fermion mass $m = 0$. We confirmed that the lattice chiral condensate converges to the continuum one in the continuum limit. Notably, we observed that the vacuum expectation value of the chiral condensate, which arises from the chiral anomaly, is reproduced at any lattice spacing, demonstrating the perfect preservation of the chiral anomaly on a lattice. We also calculated the chiral condensate for a massive fermion at almost zero and finite temperatures. We compared them with those obtained by the tensor network method and confirmed that the lattice bosonized Schwinger model produces consistent results at any fermion mass.

In Chapter 4, we investigated the confining properties of the Schwinger model at finite temperature and θ. We first obtained the probe charge dependence of the string tension at $\theta = 0$ and $\theta = \pi$ at almost zero temperature. At these θ, we found attractive and repulsive

forces between noninteger probe charges, indicating confinement and inverse confinement at low temperatures. To explain this peculiar behavior, we provided a semiclassical explanation based on the pair creation of the dynamical charges. In light of this finding, we next calculated the string tension at small probe charges $q_p = 0.3, 0.5$ in the temperature and θ angle plane, combining the reweighting method. We found that the system undergoes a smooth transition from the confining phase to the inverse confining phase as θ goes from 0 to π, and this transition is weekend as temperature increases. For high temperatures, the string tension is kept almost at zero, indicating the thermal suppression of the quantum effects of the θ term.

In Chapter 5, we have explored the phase diagram of the Schwinger model at $\theta = \pi$ in the temperature and fermion mass plane. From the perspective of universality, we conjectured that the phase diagram of the Schwinger model at $\theta = \pi$ near the quantum critical point is entirely analogous to the quantum Ising chain. This conjecture was subsequently confirmed by verifying that the correlation function of the electric field shares the same asymptotic form as the quantum Ising chain, leading to an interesting conclusion that the long-range order at zero temperature is broken by infinitesimally small thermal effects. Despite the absence of genuine phase transition, the Schwinger model at $\theta = \pi$ has a rich phase structure at finite temperature, quite differently from $\theta = 0$.

Thus, by utilizing bosonization as a method to circumvent the sign problem probably for the first time, we have revealed some new aspects of the Schwinger model, which occur in the interplay between the quantum effects of the θ term and thermal effects.

Our present studies have demonstrated that bosonization is a powerful tool not only for analytical investigations but also for a theoretically clean lattice formulation and numerical studies. An important question that arises here is the feasibility of applying the methodology to other fermionic models in $1+1$ dimensions, such as the multi-flavor Schwinger model, the gauged Thirring model, quantum chromodynamics in $(1+1)$ dimensions, and so on. Because the key formula (2.43) is model-independent and bosonization is a universal concept in $1+1$ dimensions, the methodology is expected to be applicable to a wide variety of fermionic models.

Throughout this thesis, we focused on the θ term. However, the θ term is not the only source of the sign problem. One well-known example where the sign problem arises is in finite-density systems. Because the bosonized form of the fermion density is expressed by the spatial derivative of the scalar field (1.49), the inclusion of the chemical potential term does not induce the sign problem. Hence, the present methodology would also be useful for investigating finite-density systems. Investigating finite-density systems using the present methodology would provide a new perspective on interesting phenomena at finite density, such as the breaking of homogeneity and the Silver Blaze phenomenon.

Acknowledgements

Appendix A

Bosonization

In this Appendix, we explain bosonization following Mandelstam's paper [10] and derive the bosonization formulae used in the main text (1.49, 1.50, 1.51). Throughout this Appendix, we work in the Schrödinger picture and use the chiral representation of the gamma matrices

$$\gamma^0 = \sigma^1, \quad \gamma^1 = i\sigma^2, \quad \gamma^5 = \gamma^0\gamma^1 = -\sigma^3. \tag{A.1}$$

A.1 Constraction of the Dirac fermion by bosonic operators

The Dirac fermion $\psi = (\psi_1, \psi_2)^\top$ is constructed by the scalar field ϕ and its conjugate momentum π as

$$\psi_1(x) = \left(\frac{c\mu}{2\pi}\right)^{1/2} \mathcal{N}_\mu \exp\left(-i\frac{2\pi}{\beta}\int_{-\infty}^x dx'\, \pi(x') - \frac{i\beta}{2}\phi(x)\right), \tag{A.2}$$

$$\psi_2(x) = -i\left(\frac{c\mu}{2\pi}\right)^{1/2} \mathcal{N}_\mu \exp\left(-i\frac{2\pi}{\beta}\int_{-\infty}^x dx'\, \pi(x') + \frac{i\beta}{2}\phi(x)\right), \tag{A.3}$$

where c is a constant related to Euler's constant $\gamma = 0.57721...$ as

$$c = \frac{e^\gamma}{2}. \tag{A.4}$$

The real parameter β is specified later. As explained in the main text, the symbol $\mathcal{N}_\mu$ denotes the normal ordering with respect to the bosonic creation and annihilation operators defined as

$$\phi(x) =: \int \frac{dk}{2\pi} \left(\frac{1}{2\omega(k,\mu)}\right)^{1/2} \left[a(k,\mu)e^{-ikx} + a^\dagger(k,\mu)e^{ikx}\right] =: \phi_+(x) + \phi_-(x), \tag{A.5}$$

$$\pi(x) =: -i\int \frac{dk}{2\pi} \left(\frac{\omega(k,\mu)}{2}\right)^{1/2} \left[a(k,\mu)e^{-ikx} - a^\dagger(k,\mu)e^{ikx}\right] =: \pi_+(x) + \pi_-(x), \tag{A.6}$$

with $\omega(k, \mu) = \sqrt{k^2 + \mu^2}$ and μ being the energy scale to define the normal ordering. The annihilation and creation components of ϕ are denoted by ϕ_+ and ϕ_-, respectively. The scalar field and its conjugate momentum satisfy the canonical commutation relations

$$[\phi(x), \pi(y)] = i\delta(x - y), \tag{A.7}$$

$$[\phi(x), \phi(y)] = [\pi(x), \pi(y)] = 0. \tag{A.8}$$

We are now forced to confirm that the fermion fields constructed by the bosonic fields (A.2, A.3) satisfy the canonical anticommutation relations

$$\left\{\psi_\alpha(x), \psi_\beta^\dagger(y)\right\} = \delta(x - y)\delta_{\alpha,\beta}, \tag{A.9}$$

$$\{\psi_\alpha(x), \psi_\beta(y)\} = \left\{\psi_\alpha^\dagger(x), \psi_\beta^\dagger(y)\right\} = 0. \tag{A.10}$$

A.2   Useful relations

For the evaluation of the product of the fermion fields, we use an identity

$$\mathcal{N}_\mu e^A \mathcal{N}_\mu e^B = e^{[A_+, B_-]} \mathcal{N}_\mu e^{A+B}, \quad \text{if } [A_+, B_-] \text{ is a } c \text{ number}, \tag{A.11}$$

which can be easily derived from a special case of the Campbell–Baker–Hausdorff (CBH) formula

$$e^A e^B = e^{[A,B]} e^B e^A, \quad \text{if } [A, B] \text{ is a } c \text{ number}. \tag{A.12}$$

These relations constitute the central part of the subsequent manipulations:

$$[\phi_+(x), \phi_-(y)] = \int \frac{dk}{2\pi} \frac{1}{2\omega(k, \mu)} e^{-ik(x-y)} = \Delta(x - y; \mu), \tag{A.13}$$

$$[\pi_+(x), \pi_-(y)] = \int \frac{dk}{2\pi} \frac{\omega(k, \mu)}{2} e^{-ik(x-y)} = \partial_x \partial_y \Delta(x - y; \mu), \tag{A.14}$$

$$[\phi_+(x), \pi_-(y)] = \frac{i}{2} \int \frac{dk}{2\pi} e^{-ik(x-y)} = \frac{i}{2}\delta(x - y). \tag{A.15}$$

Here, $\Delta(x; \mu)$ is the Feynman propagator for the scalar field of mass μ, which behaves as

$$\Delta(x; \mu) = -\frac{1}{2\pi} \ln |c\mu x| + \mathcal{O}(x^2) \tag{A.16}$$

for small separations. The constant c is defined in Eq. (A.4). In addition, the following

72

relations are used in the subsequent manipulations:

$$\exp\left\{\pm\left(\frac{\beta}{2}\right)^2[\phi(x),\phi(y)]\right\} = |c\mu(x-y)|^{\mp\beta^2/8\pi}\exp\{\mathcal{O}((x-y)^2)\}, \tag{A.17}$$

$$\exp\left\{\pm\left(\frac{2\pi}{\beta}\right)^2\int_{-\infty}^x dx'\int_{-\infty}^y dy'\,[\pi_+(x'),\pi_-(y')]\right\} = |c\mu(x-y)|^{\mp 2\pi/\beta^2}\exp\{\mathcal{O}((x-y)^2)\}, \tag{A.18}$$

$$\exp\left\{\pm\frac{i\pi}{2}(\Theta(x-y)-\Theta(y-x))\right\} = \pm i\frac{|x-y|}{x-y}, \tag{A.19}$$

$$\exp\left\{\pm\frac{i\pi}{2}(\Theta(x-y)+\Theta(y-x))\right\} = \pm i, \tag{A.20}$$

where $\Theta(x)$ is the step function.

A.3   Canonical anticommutation relations

Using the relations in the previous section, we now confirm the canonical anticommutation relations

$$\{\psi_\alpha^a(x),\psi_\beta^b(y)\} = \delta(x-y)\delta_{\alpha\beta}\delta_{ab}. \tag{A.21}$$

Here, $\alpha=1,2$ denotes the spinor index, and $a=1,2$ corresponds to the absence or presence of the dagger, respectively. Using this convention, the fermion field (A.2, A.3) can be written as

$$\psi_\alpha^a(x) = ((-1)^a i)^{\alpha-1}\left(\frac{c\mu}{2\pi}\right)^{1/2}\mathcal{N}_\mu\exp\left\{(-1)^a\left(i\frac{2\pi}{\beta}\int_{-\infty}^x dx'\,\pi(x')+(-1)^{\alpha-1}\frac{i\beta}{2}\phi(x)\right)\right\}. \tag{A.22}$$

We now evaluate the product of the fermion fields $\psi_\alpha^a(x)\psi_\beta^b(y)$ using the identity (A.11). The argument of the exponential factor without the normal ordering is calculated as

$$[A_+(x), B_-(y)] = (-1)^{a+b+1}\left[\frac{2\pi}{\beta}\int_{-\infty}^{x} dx'\, \pi_+(x') + (-1)^{\alpha-1}\frac{\beta}{2}\phi_+(x),\right.$$
$$\left.\frac{2\pi}{\beta}\int_{-\infty}^{y} dy'\, \pi_-(y') + (-1)^{\beta-1}\frac{\beta}{2}\phi_-(y)\right] \tag{A.23a}$$

$$= (-1)^{a+b+1}\left[(-1)^{\alpha+\beta}\left(\frac{\beta}{2}\right)^2[\phi_+(x),\phi_-(y)] + \left(\frac{2\pi}{\beta}\right)^2\int_{-\infty}^{x} dx'\int_{-\infty}^{y} dy'\,[\pi_+(x'),\pi_-(y')]\right.$$
$$\left. - (-1)^\alpha\pi\int_{-\infty}^{y} dy'\,[\phi_+(x),\pi_-(y')] - (-1)^\beta\pi\int_{-\infty}^{x} dx'\,[\pi_+(x'),\phi_-(y)]\right] \tag{A.23b}$$

$$= (-1)^{a+b+1}\left[(-1)^{\alpha+\beta}\left(\frac{\beta}{2}\right)^2[\phi_+(x),\phi_-(y)] + \left(\frac{2\pi}{\beta}\right)^2\int_{-\infty}^{x} dx'\int_{-\infty}^{y} dy'\,[\pi_+(x'),\pi_-(y')]\right.$$
$$\left. + \frac{i\pi}{2}\left\{(-1)^\beta\theta(x-y) - (-1)^\alpha\theta(y-x)\right\}\right]. \tag{A.23c}$$

Hence, we obtain

$$\psi_\alpha^a(x)\psi_\beta^b(y) = ((-1)^a i)^{\alpha-1}((-1)^b i)^{\beta-1}\frac{c\mu}{2\pi}e^{[A_+(x),B_-(y)]}$$
$$\times \mathcal{N}_\mu \exp\left\{(-1)^a\left(i\frac{2\pi}{\beta}\int_{-\infty}^{x} dx'\pi(x') + (-1)^{\alpha-1}i\frac{\beta}{2}\phi(x)\right)\right.$$
$$\left. + (-1)^b\left(i\frac{2\pi}{\beta}\int_{-\infty}^{y} dy'\pi(y') + (-1)^{\beta-1}i\frac{\beta}{2}\phi(y)\right)\right\}, \tag{A.24}$$

where the exponential factor without the normal ordering is

$$e^{[A_+(x),B_-(y)]} = |c\mu(x-y)|^{(-1)^{a+b+\alpha+\beta}\beta^2/8\pi + (-1)^{a+b}2\pi/\beta^2}\exp\left(\mathcal{O}((x-y)^2)\right)$$
$$\times (-1)^{a+b+\beta+1}\begin{cases} i\frac{|x-y|}{x-y}, & \alpha = \beta, \\ i, & \alpha \neq \beta. \end{cases} \tag{A.25}$$

The vanishing anticommutation relations at $a = b$ can be easily seen:

$$\{\psi_\alpha^a(x), \psi_\beta^a(y)\} = \text{some factor} \times \begin{cases} (-1)^{\beta+1}i\frac{|x-y|}{x-y} + (-1)^{\alpha+1}i\frac{|y-x|}{y-x}, & \alpha = \beta \\ (-1)^{\beta+1}i + (-1)^{\alpha+1}i, & \alpha \neq \beta \end{cases} \tag{A.26a}$$
$$= 0. \tag{A.26b}$$

We next consider the anticommutation relation $\{\psi_\alpha^\dagger(x), \psi_\beta(y)\}$, i.e., the case of $a = 2, b = 1$. The first term is given by

$$\psi_\alpha^\dagger(x)\psi_\beta(y) = i^{\alpha-1}(-i)^{\beta-1}\frac{c\mu}{2\pi}e^{[A_+(x),B_-(y)]}$$
$$\times \mathcal{N}_\mu \exp\left\{-i\frac{2\pi}{\beta}\int_{x}^{y} d\xi\,\pi(\xi) - i\frac{\beta}{2}\left((-1)^{\beta-1}\phi(y) - (-1)^{\alpha-1}\phi(x)\right)\right\}, \tag{A.27}$$

where the exponential factor without the normal ordering is

$$
\begin{aligned}
e^{[A_+(x),B_-(y)]} =& |c\mu(x-y)|^{(-1)^{\alpha+\beta+1}\beta^2/8\pi-2\pi/\beta^2} \exp\big(\mathcal{O}((x-y)^2)\big) \\
& \times (-1)^\beta \begin{cases} i\frac{|x-y|}{x-y}, & \alpha=\beta, \\ i, & \alpha\neq\beta. \end{cases}
\end{aligned} \tag{A.28}
$$

The second term is given by

$$
\begin{aligned}
\psi_\beta(y)\psi_\alpha^\dagger(x) =& i^{\alpha-1}(-i)^{\beta-1}\frac{c\mu}{2\pi}e^{[A_+(y),B_-(x)]} \\
& \times \mathcal{N}_\mu \exp\left\{-i\frac{2\pi}{\beta}\int_x^y d\xi\,\pi(\xi) - i\frac{\beta}{2}\big((-1)^{\beta-1}\phi(y)-(-1)^{\alpha-1}\phi(x)\big)\right\}, \quad \text{(A.29)}
\end{aligned}
$$

where the exponential factor without the normal ordering is

$$
\begin{aligned}
e^{[A_+(y),B_-(x)]} =& |c\mu(x-y)|^{(-1)^{\alpha+\beta+1}\beta^2/8\pi-2\pi/\beta^2} \exp\big(\mathcal{O}((x-y)^2)\big) \\
& \times (-1)^\alpha \begin{cases} i\frac{|y-x|}{y-x}, & \alpha=\beta, \\ i, & \alpha\neq\beta. \end{cases}
\end{aligned} \tag{A.30}
$$

For $\alpha\neq\beta$, we find $\{\psi_\alpha^\dagger(x),\psi_\beta(y)\}=0$, as expected. For $\alpha=\beta$, we also find $\{\psi_\alpha^\dagger(x),\psi_\alpha(y)\}=0$ at $x\neq y$. In the limit $x\to y$, the product

$$
\begin{aligned}
\psi_\alpha^\dagger(x)\psi_\alpha(y) =& (-1)^\alpha i\frac{c\mu}{2\pi}\frac{|x-y|}{x-y}|c\mu(x-y)|^{-\beta^2/8\pi-2\pi/\beta^2} \\
& \times \mathcal{N}_\mu \exp\left\{-i\frac{2\pi}{\beta}\int_x^y dx'\,\pi(x') + (-1)^\alpha\frac{i\beta}{2}(\phi(y)-\phi(x))\right\}
\end{aligned} \tag{A.31}
$$

seems to be divergent, so careful analysis is required. Following Mandelstam, we indirectly confirm the nonvanishing anticommutation relation by showing the commutation relations among the vector currents $j^\mu=\overline{\psi}\gamma^\mu\psi$:

$$
\begin{aligned}
\big[j^0(x),\psi_\alpha(y)\big] &= -\delta(x-y)\psi_\alpha(x), \tag{A.32}\\
\big[j^1(x),\psi_\alpha(y)\big] &= -\delta(x-y)\big(\gamma^5\psi(x)\big)_\alpha, \tag{A.33}
\end{aligned}
$$

after the bosonization of the vector current.

A.4 Bosonization formulae

In this section, we derive the bosonization formulae used in the main text (1.49, 1.50, 1.51).

A.4.1 Bosonization of the vector current

Under the chiral representation (A.1), the vector current is written as

$$j^\mu = \bar{\psi}\gamma^\mu\psi = \begin{cases} \psi_1^\dagger\psi_1 + \psi_2^\dagger\psi_2, & \mu = 0, \\ -\psi_1^\dagger\psi_1 + \psi_2^\dagger\psi_2, & \mu = 1. \end{cases} \tag{A.34}$$

Using Eq. (A.31), j^0 is calculated as

$$j^0(x) = \lim_{y \to x} \psi_1^\dagger(x)\psi_1(y) + \psi_2^\dagger(x)\psi_2(y) \tag{A.35a}$$

$$= \lim_{y \to x} \frac{-i}{2\pi(x-y)} |c\mu(x-y)|^{1-\beta^2/8\pi-2\pi/\beta^2}$$

$$\times \mathcal{N}_\mu \left[\exp\left\{ -i\frac{2\pi}{\beta} \int_x^y d\xi\, \pi(\xi) - \frac{i\beta}{2}(\phi(y) - \phi(x)) \right\} \right.$$

$$\left. - \exp\left\{ -i\frac{2\pi}{\beta} \int_x^y d\xi\, \pi(\xi) + \frac{i\beta}{2}(\phi(y) - \phi(x)) \right\} \right]. \tag{A.35b}$$

Because the two components in the argument of the exponential are commutative

$$\left[\int_x^y d\xi\, \pi(\xi), \phi(y) - \phi(x) \right] = 0, \tag{A.36}$$

the vector current is written as

$$j^0(x) = \lim_{y \to x} \frac{1}{\pi(y-x)} |c\mu(x-y)|^{1-\beta^2/8\pi-2\pi/\beta^2}$$

$$\times \mathcal{N}_\mu \exp\left(-i\frac{2\pi}{\beta} \int_x^y d\xi\, \pi(\xi) \right) \sin\left(\frac{\beta}{2}(\phi(y) - \phi(x)) \right) \tag{A.37a}$$

$$= \frac{\beta}{2\pi} |c\mu(x-y)|^{1-\beta^2/8\pi-2\pi/\beta^2} \partial_x\phi(x). \tag{A.37b}$$

As for j^1, we similarly find

$$j^1(x) = \lim_{y \to x} -\psi_1^\dagger(x)\psi_1(y) + \psi_2^\dagger(x)\psi_2(y) \tag{A.38a}$$

$$= \lim_{y \to x} \frac{-i}{\pi(y-x)} |c\mu(x-y)|^{1-\beta^2/8\pi-2\pi/\beta^2}$$

$$\times \mathcal{N}_\mu \exp\left(-i\frac{2\pi}{\beta} \int_x^y d\xi\, \pi(\xi) \right) \cos\left(\frac{\beta}{2}(\phi(y) - \phi(x)) \right) \tag{A.38b}$$

$$= -\frac{2}{\beta} |c\mu(x-y)|^{1-\beta^2/8\pi-2\pi/\beta^2} \pi, \tag{A.38c}$$

where we neglected an irrelevant additive constant. Because the exponent $1 - \beta^2/8\pi - 2\pi/\beta^2$ takes its maximum value of zero at $\beta = 2\sqrt{\pi}$, the vector current is regularized only at $\beta = 2\sqrt{\pi}$. The regularized vector current is then written as

$$j^\mu = \begin{cases} \frac{1}{\sqrt{\pi}}\partial_x\phi, & \mu = 0, \\ -\frac{1}{\sqrt{\pi}}\pi, & \mu = 1, \end{cases} \tag{A.39}$$

which is Eq. (1.49) in the main text.

We now confirm the commutation relations among the vector currents (A.32, A.33). Using the bosonized form of j^0, we find

$$\left[j^0(x), \psi_1(y)\right] = \frac{\beta}{2\pi}[\partial_x \phi(x), \psi_1(y)] \tag{A.40a}$$

$$= \frac{\beta}{2\pi}\left(\frac{c\mu}{2\pi}\right)^{1/2}\left[\partial_x\phi(x), \mathcal{N}_\mu \exp\left(-i\frac{2\pi}{\beta}\int_{-\infty}^{y} dy' \,\pi(y) - i\frac{\beta}{2}\phi(y)\right)\right] \tag{A.40b}$$

$$= \frac{\beta}{2\pi}\left(\left[\partial_x\phi_+(x), -i\frac{2\pi}{\beta}\int_{-\infty}^{y} dy'\,\pi_-(y') - i\frac{\beta}{2}\phi_-(y)\right]\right.$$
$$\left.+ \left[\partial_x\phi_-(x), -i\frac{2\pi}{\beta}\int_{-\infty}^{y} dy'\,\pi_+(y') - i\frac{\beta}{2}\phi_+(y)\right]\right)\psi_1(y), \tag{A.40c}$$

where an identity

$$\left[A, \mathcal{N}e^B\right] = ([A_+, B_-] + [A_-, B_+])\mathcal{N}e^B, \text{ if } [A_+, B_-], [A_-, B_+] \text{ are } c \text{ numbers,} \tag{A.41}$$

which can be derived from a special case of the CBH formula

$$Ae^B = e^B A + [A, B]e^B, \text{ if } [A, B] \text{ is a } c \text{ number,} \tag{A.42}$$

is used from Eq. (A.40b) to Eq. (A.40c). The first and second terms are calculated as

$$\left[\partial_x\phi_+(x), -i\frac{2\pi}{\beta}\int_{-\infty}^{y} dy'\,\pi_-(y') - i\frac{\beta}{2}\phi_-(y)\right] = -\frac{\pi}{\beta}\delta(x-y) - i\frac{\beta}{2}\partial_x\Delta(x-y;\mu), \tag{A.43}$$

$$\left[\partial_x\phi_-(x), -i\frac{2\pi}{\beta}\int_{-\infty}^{y} dy'\,\pi_+(y') - i\frac{\beta}{2}\phi_+(y)\right] = -\frac{\pi}{\beta}\delta(x-y) + i\frac{\beta}{2}\partial_x\Delta(x-y;\mu), \tag{A.44}$$

respectively. Hence, we obtain

$$\left[j^0(x), \psi_1(y)\right] = -\delta(x-y)\psi_1(x). \tag{A.45}$$

Similarly, we find

$$\left[j^0(x), \psi_2(y)\right] = -\delta(x-y)\psi_2(x), \tag{A.46}$$

$$\left[j^1(x), \psi_1(y)\right] = \delta(x-y)\psi_1(y), \tag{A.47}$$

$$\left[j^1(x), \psi_2(y)\right] = -\delta(x-y)\psi_1(y). \tag{A.48}$$

Thus, the commutation relations (A.32, A.33) and the nonvanishing anticommutation relations are confirmed.

A.4.2   Bosonization of the free massless Dirac fermion

We next obtain the bosonized form of the free massless Dirac fermion component in the Hamiltonian

$$-\overline{\psi}(x)i\partial_x\gamma^1\psi(x) = \lim_{dx\to 0}\frac{-i}{2dx}\psi^\dagger(x)\left(\gamma^5\psi(x+dx) - \gamma^5\psi(x-dx)\right). \tag{A.49}$$

Recalling the bosonization of $j^1 = \psi^\dagger \gamma^5 \psi$, we find

$$-\overline{\psi}(x)i\partial_x\gamma^1\psi(x) = \lim_{dx\to 0} \frac{-1}{2\pi}\frac{1}{dx^2}|c\mu dx|^{1-\beta^2/8\pi-2\pi/\beta^2}$$

$$\times \mathcal{N}_\mu \left[\exp\left(-\frac{2\pi i}{\beta}\pi(x)dx\right)\cos\left(\frac{\beta}{2}\partial_x\phi(x)dx\right)\right.$$

$$\left. + \exp\left(\frac{2\pi i}{\beta}\pi(x)dx\right)\cos\left(-\frac{\beta}{2}\partial_x\phi(x)dx\right)\right] \quad \text{(A.50a)}$$

$$= \lim_{dx\to 0} \frac{-1}{2\pi}\frac{1}{dx^2}|c\mu dx|^{1-\beta^2/8\pi-2\pi/\beta^2}$$

$$\times \left[2 + \left\{\left(\frac{2\pi i}{\beta}\right)^2\pi(x)^2 - \left(\frac{\beta}{2}\right)^2(\partial_x\phi(x))^2\right\}(dx)^2 + \mathcal{O}\big((dx)^4\big)\right] \quad \text{(A.50b)}$$

$$= \lim_{dx\to 0} |c\mu dx|^{1-\beta^2/8\pi-2\pi/\beta^2}\left[\frac{2\pi}{\beta^2}\pi(x)^2 + \frac{\beta^2}{8\pi}(\partial_x\phi)^2\right], \quad \text{(A.50c)}$$

where we neglected an irrelevant additive constant. Thus, at $\beta = 2\sqrt{\pi}$, we obtain

$$-\overline{\psi}i\partial_x\gamma^1\psi = \frac{1}{2}\pi^2 + \frac{1}{2}(\partial_x\phi)^2, \quad \text{(A.51)}$$

which is Eq. (1.50) in the main text.

A.4.3 Bosonization of the chiral condensate

We finally obtain the bosonized form of the chiral condensate

$$\overline{\psi}(x)\psi(x) = \lim_{y\to x} \psi_2^\dagger(x)\psi_1(y) + \psi_1^\dagger(x)\psi_2(y). \quad \text{(A.52)}$$

Using Eq. (A.31), the first term is evaluated as

$$\lim_{y\to x} \psi_2^\dagger(x)\psi_1(y) = \lim_{y\to x}\frac{c\mu}{2\pi}e^{\mu/4\epsilon}|c\mu(x-y)|^{\beta^2/8\pi-2\pi/\beta^2}$$

$$\times \mathcal{N}_\mu\exp\left\{-i\frac{2\pi}{\beta}\int_x^y d\xi\,\pi(\xi) - i\frac{\beta}{2}(\phi(y)+\phi(x)) + \mathcal{O}((x-y)^2)\right\} \quad \text{(A.53)}$$

$$= \lim_{y\to x}\frac{c\mu}{2\pi}|c\mu(x-y)|^{\beta^2/8\pi-2\pi/\beta^2}\mathcal{N}_\mu\exp(-i\beta\phi(x)) \quad \text{(A.54)}$$

Similarly, the second term is calculated as

$$\lim_{y\to x} \psi_1^\dagger(x)\psi_2(y) = \lim_{y\to x}\frac{c\mu}{2\pi}|c\mu(x-y)|^{\beta^2/8\pi-2\pi/\beta^2}\mathcal{N}_\mu\exp(i\beta\phi(x)). \quad \text{(A.55)}$$

Hence, the chiral condensate is expressed by the scalar field as

$$\overline{\psi}(x)\psi(x) = \lim_{y\to x}\frac{e^\gamma}{2\pi}\mu|c\mu(x-y)|^{\beta^2/8\pi-2\pi/\beta^2}\mathcal{N}_\mu\cos(\beta\phi). \quad \text{(A.56)}$$

Note that the sign of the chiral condensate changes by the irrelevant shift

$$\psi' = i\gamma^5\psi, \tag{A.57}$$

which corresponds to a change in the sign of the fermion mass. Therefore, by setting $\beta = 2\sqrt{\pi}$, we obtain the bosonized form of the chiral condensate

$$\overline{\psi}\psi = -\frac{e^\gamma}{2\pi}\mu\mathcal{N}_\mu \cos\bigl(2\sqrt{\pi}\phi\bigr), \tag{A.58}$$

which is Eq. (1.51) in the main text.

Bibliography

[1] H. Ohata, *Monte Carlo study of Schwinger model without the sign problem*, *JHEP* **12** (2023) 007 [2303.05481].

[2] H. Ohata, *Phase diagram near the quantum critical point in Schwinger model at $\theta = \pi$: analogy with quantum Ising chain*, *PTEP* **2024** (2023) 013B02 [2311.04738].

[3] D.J. Gross and F. Wilczek, *Ultraviolet Behavior of Nonabelian Gauge Theories*, *Phys. Rev. Lett.* **30** (1973) 1343.

[4] H. Politzer, *Reliable Perturbative Results for Strong Interactions?*, *Phys. Rev. Lett.* **30** (1973) 1346.

[5] PARTICLE DATA GROUP collaboration, *Review of Particle Physics*, *PTEP* **2022** (2022) 083C01.

[6] C. Abel et al., *Measurement of the Permanent Electric Dipole Moment of the Neutron*, *Phys. Rev. Lett.* **124** (2020) 081803 [2001.11966].

[7] J.E. Kim and G. Carosi, *Axions and the Strong CP Problem*, *Rev. Mod. Phys.* **82** (2010) 557 [0807.3125].

[8] J.S. Schwinger, *Gauge Invariance and Mass. 2.*, *Phys. Rev.* **128** (1962) 2425.

[9] S.R. Coleman, *The Quantum Sine-Gordon Equation as the Massive Thirring Model*, *Phys. Rev. D* **11** (1975) 2088.

[10] S. Mandelstam, *Soliton Operators for the Quantized Sine-Gordon Equation*, *Phys. Rev. D* **11** (1975) 3026.

[11] S.R. Coleman, R. Jackiw and L. Susskind, *Charge Shielding and Quark Confinement in the Massive Schwinger Model*, *Annals Phys.* **93** (1975) 267.

[12] S.R. Coleman, *More About the Massive Schwinger Model*, *Annals Phys.* **101** (1976) 239.

[13] W. Fischler, J.B. Kogut and L. Susskind, *Quark Confinement in Unusual Environments*, *Phys. Rev. D* **19** (1979) 1188.

[14] N.S. Manton, *The Schwinger Model and Its Axial Anomaly*, *Annals Phys.* **159** (1985) 220.

[15] S. Iso and H. Murayama, *Hamiltonian Formulation of the Schwinger Model: Nonconfinement and Screening of the Charge*, *Prog. Theor. Phys.* **84** (1990) 142.

[16] J.E. Hetrick and Y. Hosotani, *QED ON A CIRCLE*, *Phys. Rev. D* **38** (1988) 2621.

[17] A.V. Smilga, *On the fermion condensate in Schwinger model*, *Phys. Lett. B* **278** (1992) 371.

[18] A.V. Smilga, *Critical amplitudes in two-dimensional theories*, *Phys. Rev. D* **55** (1997) 443 [`hep-th/9607154`].

[19] I. Sachs and A. Wipf, *Finite temperature Schwinger model*, *Helv. Phys. Acta* **65** (1992) 652 [`1005.1822`].

[20] T.M.R. Byrnes, P. Sriganesh, R.J. Bursill and C.J. Hamer, *Density matrix renormalization group approach to the massive Schwinger model*, *Phys. Rev. D* **66** (2002) 013002 [`hep-lat/0202014`].

[21] M.C. Bañuls, K. Cichy, K. Jansen and J.I. Cirac, *The mass spectrum of the Schwinger model with Matrix Product States*, *JHEP* **11** (2013) 158 [`1305.3765`].

[22] B. Buyens, J. Haegeman, K. Van Acoleyen, H. Verschelde and F. Verstraete, *Matrix product states for gauge field theories*, *Phys. Rev. Lett.* **113** (2014) 091601 [`1312.6654`].

[23] Y. Shimizu and Y. Kuramashi, *Grassmann tensor renormalization group approach to one-flavor lattice Schwinger model*, *Phys. Rev. D* **90** (2014) 014508 [`1403.0642`].

[24] Y. Shimizu and Y. Kuramashi, *Critical behavior of the lattice Schwinger model with a topological term at $\theta = \pi$ using the Grassmann tensor renormalization group*, *Phys. Rev. D* **90** (2014) 074503 [`1408.0897`].

[25] B. Buyens, K. Van Acoleyen, J. Haegeman and F. Verstraete, *Matrix product states for Hamiltonian lattice gauge theories*, *PoS* **LATTICE2014** (2014) 308 [`1411.0020`].

[26] M.C. Bañuls, K. Cichy, J.I. Cirac, K. Jansen and H. Saito, *Thermal evolution of the Schwinger model with Matrix Product Operators*, *Phys. Rev. D* **92** (2015) 034519 [`1505.00279`].

[27] B. Buyens, J. Haegeman, H. Verschelde, F. Verstraete and K. Van Acoleyen, *Confinement and string breaking for QED_2 in the Hamiltonian picture*, *Phys. Rev. X* **6** (2016) 041040 [`1509.00246`].

[28] M.C. Bañuls, K. Cichy, K. Jansen and H. Saito, *Chiral condensate in the Schwinger model with Matrix Product Operators*, *Phys. Rev. D* **93** (2016) 094512 [`1603.05002`].

[29] B. Buyens, F. Verstraete and K. Van Acoleyen, *Hamiltonian simulation of the Schwinger model at finite temperature*, *Phys. Rev. D* **94** (2016) 085018 [1606.03385].

[30] M.C. Bañuls, K. Cichy, J.I. Cirac, K. Jansen and S. Kühn, *Density Induced Phase Transitions in the Schwinger Model: A Study with Matrix Product States*, *Phys. Rev. Lett.* **118** (2017) 071601 [1611.00705].

[31] B. Buyens, S. Montangero, J. Haegeman, F. Verstraete and K. Van Acoleyen, *Finite-representation approximation of lattice gauge theories at the continuum limit with tensor networks*, *Phys. Rev. D* **95** (2017) 094509 [1702.08838].

[32] L. Funcke, K. Jansen and S. Kühn, *Topological vacuum structure of the Schwinger model with matrix product states*, *Phys. Rev. D* **101** (2020) 054507 [1908.00551].

[33] E. Ercolessi, P. Facchi, G. Magnifico, S. Pascazio and F.V. Pepe, *Phase Transitions in Z_n Gauge Models: Towards Quantum Simulations of the Schwinger-Weyl QED*, *Phys. Rev. D* **98** (2018) 074503 [1705.11047].

[34] S. Kühn, J.I. Cirac and M.-C. Bañuls, *Quantum simulation of the Schwinger model: A study of feasibility*, *Phys. Rev. A* **90** (2014) 042305 [1407.4995].

[35] T.V. Zache, N. Mueller, J.T. Schneider, F. Jendrzejewski, J. Berges and P. Hauke, *Dynamical Topological Transitions in the Massive Schwinger Model with a θ Term*, *Phys. Rev. Lett.* **122** (2019) 050403 [1808.07885].

[36] C. Kokail et al., *Self-verifying variational quantum simulation of lattice models*, *Nature* **569** (2019) 355 [1810.03421].

[37] G. Magnifico, M. Dalmonte, P. Facchi, S. Pascazio, F.V. Pepe and E. Ercolessi, *Real Time Dynamics and Confinement in the $\mathbb{Z}_n$ Schwinger-Weyl lattice model for 1+1 QED*, *Quantum* **4** (2020) 281 [1909.04821].

[38] B. Chakraborty, M. Honda, T. Izubuchi, Y. Kikuchi and A. Tomiya, *Classically emulated digital quantum simulation of the Schwinger model with a topological term via adiabatic state preparation*, *Phys. Rev. D* **105** (2022) 094503 [2001.00485].

[39] M. Honda, E. Itou, Y. Kikuchi, L. Nagano and T. Okuda, *Classically emulated digital quantum simulation for screening and confinement in the Schwinger model with a topological term*, *Phys. Rev. D* **105** (2022) 014504 [2105.03276].

[40] S. Thompson and G. Siopsis, *Quantum computation of phase transition in the massive Schwinger model*, *Quantum Sci. Technol.* **7** (2022) 035001 [2110.13046].

[41] M. Honda, E. Itou, Y. Kikuchi and Y. Tanizaki, *Negative string tension of a higher-charge Schwinger model via digital quantum simulation*, *PTEP* **2022** (2022) 033B01 [2110.14105].

[42] J.C. Halimeh, I.P. McCulloch, B. Yang and P. Hauke, *Tuning the Topological θ-Angle in Cold-Atom Quantum Simulators of Gauge Theories*, *PRX Quantum* **3** (2022) 040316 [2204.06570].

[43] QuNu collaboration, *Variational thermal quantum simulation of the lattice Schwinger model*, *Phys. Rev. D* **106** (2022) 054509 [2205.12767].

[44] C. Gattringer, T. Kloiber and V. Sazonov, *Solving the sign problems of the massless lattice Schwinger model with a dual formulation*, *Nucl. Phys. B* **897** (2015) 732 [1502.05479].

[45] D. Göschl, C. Gattringer, A. Lehmann and C. Weis, *Simulation strategies for the massless lattice Schwinger model in the dual formulation*, *Nucl. Phys. B* **924** (2017) 63 [1708.00649].

[46] Y. Tanizaki and M. Tachibana, *Multi-flavor massless QED$_2$ at finite densities via Lefschetz thimbles*, *JHEP* **02** (2017) 081 [1612.06529].

[47] A. Alexandru, G. Başar, P.F. Bedaque, H. Lamm and S. Lawrence, *Finite Density QED$_{1+1}$ Near Lefschetz Thimbles*, *Phys. Rev. D* **98** (2018) 034506 [1807.02027].

[48] L.S. Brown, *Gauge invariance and mass in a two-dimensional model*, *Il Nuovo Cimento (1955-1965)* **29** (1963) 617.

[49] S.L. Adler, *Axial vector vertex in spinor electrodynamics*, *Phys. Rev.* **177** (1969) 2426.

[50] J. Bell and R. Jackiw, *A PCAC puzzle: $\pi^0 \to \gamma\gamma$ in the σ model*, *Nuovo Cim. A* **60** (1969) 47.

[51] K. Fujikawa, *Path Integral Measure for Gauge Invariant Fermion Theories*, *Phys. Rev. Lett.* **42** (1979) 1195.

[52] K. Fujikawa, *Path Integral for Gauge Theories with Fermions*, *Phys. Rev. D* **21** (1980) 2848.

[53] S.R. Coleman, *There are no Goldstone bosons in two-dimensions*, *Commun. Math. Phys.* **31** (1973) 259.

[54] C. Adam, *Charge screening and confinement in the massive Schwinger model*, *Phys. Lett. B* **394** (1997) 161 [hep-th/9609155].

[55] C. Adam, *Massive Schwinger model within mass perturbation theory*, *Annals Phys.* **259** (1997) 1 [hep-th/9704064].

[56] C. Adam, *Normalization of the chiral condensate in the massive Schwinger model*, *Phys. Lett. B* **440** (1998) 117 [hep-th/9806211].

[57] J.B. Kogut and L. Susskind, *How to Solve the eta –> 3 pi Problem by Seizing the Vacuum*, *Phys. Rev. D* **11** (1975) 3594.

[58] K.G. Wilson, *Confinement of quarks*, *Phys. Rev. D* **10** (1974) 2445.

[59] H.B. Nielsen and M. Ninomiya, *Absence of Neutrinos on a Lattice. 1. Proof by Homotopy Theory*, *Nucl. Phys. B* **185** (1981) 20.

[60] H.B. Nielsen and M. Ninomiya, *Absence of Neutrinos on a Lattice. 2. Intuitive Topological Proof*, *Nucl. Phys. B* **193** (1981) 173.

[61] H.-J. Rothe, *Lattice Gauge Theories, 4th ed.*, World Scientific (2012).

[62] S. Duane, A.D. Kennedy, B.J. Pendleton and D. Roweth, *Hybrid Monte Carlo*, *Phys. Lett. B* **195** (1987) 216.

[63] Z.-C. Gu, F. Verstraete and X.-G. Wen, *Grassmann tensor network states and its renormalization for strongly correlated fermionic and bosonic states*, 2010.

[64] J.B. Kogut and L. Susskind, *Hamiltonian Formulation of Wilson's Lattice Gauge Theories*, *Phys. Rev. D* **11** (1975) 395.

[65] P. Jordan and E.P. Wigner, *About the Pauli exclusion principle*, *Z. Phys.* **47** (1928) 631.

[66] C.J. Hamer, J.B. Kogut, D.P. Crewther and M.M. Mazzolini, *The Massive Schwinger Model on a Lattice: Background Field, Chiral Symmetry and the String Tension*, *Nucl. Phys. B* **208** (1982) 413.

[67] I. Bender, H.J. Rothe and K.D. Rothe, *Monte Carlo Study of Screening Versus Confinement in the Massless and Massive Schwinger Model*, *Nucl. Phys. B* **251** (1985) 745.

[68] M. Creutz, *Monte Carlo Study of Quantized SU(2) Gauge Theory*, *Phys. Rev. D* **21** (1980) 2308.

[69] V. Azcoiti, E. Follana, E. Royo-Amondarain, G. Di Carlo and A. Vaquero Avilés-Casco, *Massive Schwinger model at finite θ*, *Phys. Rev. D* **97** (2018) 014507 [`1709.07667`].

[70] T. Misumi, Y. Tanizaki and M. Ünsal, *Fractional θ angle, 't Hooft anomaly, and quantum instantons in charge-q multi-flavor Schwinger model*, *JHEP* **07** (2019) 018 [`1905.05781`].

[71] C.J. Hamer and M.N. Barber, *Finite-size scaling in hamiltonian field theory*, *Journal of Physics A: Mathematical and General* **13** (1980) L169.

[72] S.R. White, *Density matrix formulation for quantum renormalization groups*, *Phys. Rev. Lett.* **69** (1992) 2863.

[73] S.R. White, *Density-matrix algorithms for quantum renormalization groups*, *Phys. Rev. B* **48** (1993) 10345.

[74] F. Verstraete, J.J. García-Ripoll and J.I. Cirac, *Matrix product density operators: Simulation of finite-temperature and dissipative systems*, *Phys. Rev. Lett.* **93** (2004) 207204.

[75] M. Zwolak and G. Vidal, *Mixed-state dynamics in one-dimensional quantum lattice systems: A time-dependent superoperator renormalization algorithm*, *Phys. Rev. Lett.* **93** (2004) 207205.

[76] S. Sachdev, *Quantum Phase Transitions*, Cambridge University Press, 2 ed. (2011), 10.1017/CBO9780511973765.

[77] E.H. Lieb, T. Schultz and D. Mattis, *Two soluble models of an antiferromagnetic chain*, *Annals Phys.* **16** (1961) 407.

[78] P. Pfeuty, *The one-dimensional ising model with a transverse field*, *Annals of Physics* **57** (1970) 79.

[79] S. Sachdev, *Universal, finite temperature, crossover functions of the quantum transition in the Ising chain in a transverse field*, *Nucl. Phys. B* **464** (1996) 576 [`cond-mat/9509147`].

[80] M. Vojta, *Quantum phase transitions*, *Reports on Progress in Physics* **66** (2003) 2069 [`cond-mat/0309604`].

[81] A. Sokal, *Monte carlo methods in statistical mechanics: Foundations and new algorithms*, in *Functional Integration: Basics and Applications*, C. DeWitt-Morette, P. Cartier and A. Folacci, eds., (Boston, MA), pp. 131–192, Springer US (1997), DOI.

[82] T. Byrnes, *Density matrix renormalization group: a new approach to lattice gauge theory*, Ph.D. thesis, The University of New South Wales, 2003. https://doi.org/10.26190/unsworks/6053.